UNIVERSITÀ
DEGLI STUDI
FIRENZE

DOTTORATO DI RICERCA IN SCIENZE CHIMICHE

CICLO XXX

COORDINATORE Prof. Piero Baglioni

CHEMICAL AND PHYSICAL CHARACTERIZATION FOR SOURCE APPORTIONMENT OF MULTI-YEAR ARCTIC AEROSOL RECORDS

Dottorando	**Tutore**
Dott. Fabio Giardi	Prof. Roberto Udisti

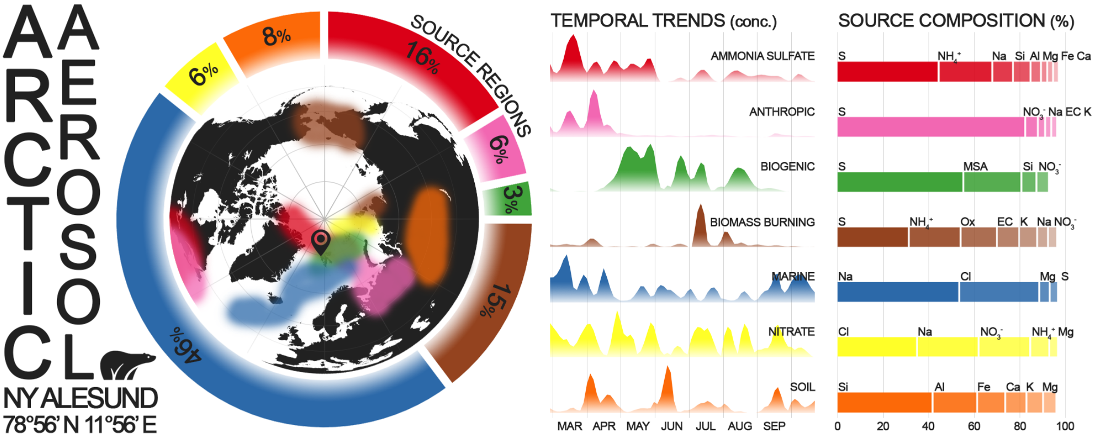

Settore Scientifico Disciplinare CHIM/01 - CHIM/12

Anni 2014/2017

UNIVERSITÀ
DEGLI STUDI
FIRENZE

DOTTORATO DI RICERCA IN SCIENZE CHIMICHE

CICLO XXX

COORDINATORE Prof. Piero Baglioni

CHEMICAL AND PHYSICAL CHARACTERIZATION FOR SOURCE APPORTIONMENT OF MULTI-YEAR ARCTIC AEROSOL RECORDS

Settore Scientifico Disciplinare CHIM/01 - CHIM/12

Dottorando
Dott. Fabio Giardi

Tutore
Prof. Roberto Udisti

Coordinatore
Prof. Piero Baglioni

Anni 2014/2017

You don’t need a weather man
to know which way the wind blows

Bob Dylan

Contents

Chapter 1

Introduction

1.1 Climate change

Earth's climate has always been subject to slow and cyclical changes, that brought to alternate warm and cold periods as a result of the influence of many natural factors. The scientific interest of last years has increasingly focused on the environmental issues that affect global climate change and the study of how human activity in the last few centuries has affected and amplified these changes. The interest that the climate change has raised on the global scale is due to the strong impact that such changes, with particular attention to the rapid and sudden ones, have on the society. So it is necessary reliable and realistic climate models which allow us to understand the influence of the forcing factors and their feedback mechanisms and thus to predict future scenarios. Even though these factors are known, the understanding of how they influence the climate is still affected by a large uncertainty (IPCC, 2013, fig. 1.1). The modeling design is made even more difficult by the deep interconnection existing between atmosphere, oceans, biosphere, cryosphere, and lithosphere. Such systems are in fact very different in extension, features, and variability, but related one to each other, so that changes occurring within a system inevitably affect the others. In addition, to improve the formulation of reliable climate models, it is useful to reconstruct the climate of the past through the study of ice cores and to identify the conditions that led to significant climate changes.

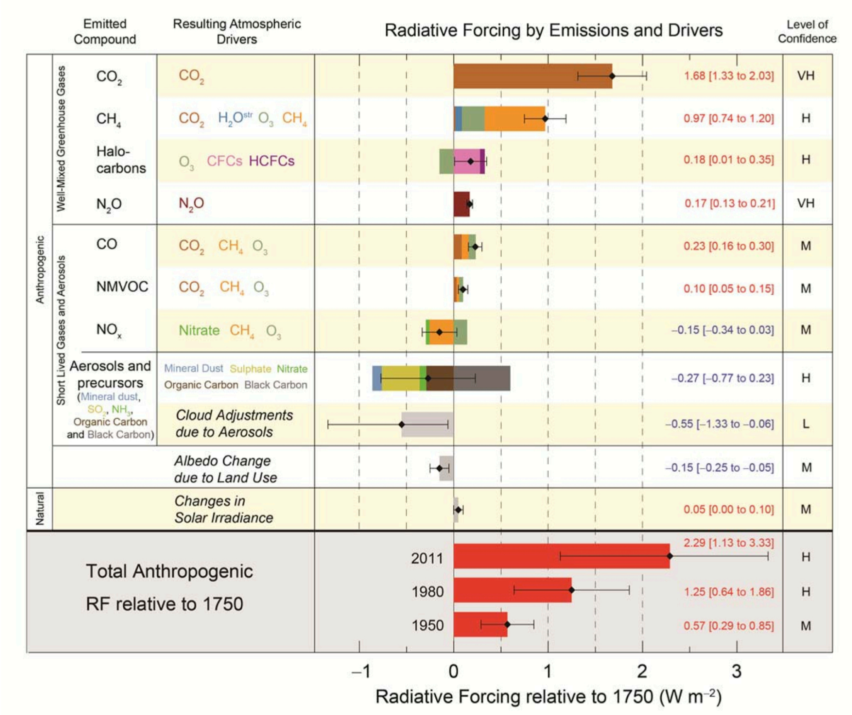

Figure 1.1 – The radiative-forcing bar chart reported by the IPCC 2013 (Working Group 1).

The radiative balance of the Earth in thermal equilibrium assumes that the incoming solar radiation is equivalent to the Earth's emission energy flux. Climatic variations come up when the radiative budget of the planet is not in equilibrium and, as a consequence, the Earth is subjected to heating or cooling phases. The causes of imbalance can be summarized in the variation of three main factors: the solar energy flow, which depends both on the solar activity and on the Earth's relative position; the greenhouse effect, which depends on the nature and atmospheric concentration of the greenhouse gases; and the albedo, which is the total reflectivity of the planet. While the first factor influences the climate on very large time scales and may explain, for example, ice ages occurrence, on the other hand, the other two factors are much more responsive and can give an explanation for the global warming of the last decades.

1.2 Atmospheric aerosols

The atmospheric aerosols plays an important role within the global climate system because of its influence in the complex feedback processes between climate forcings and environmental responses, through the interaction with the solar irradiance. Suspended particles influence the planet's albedo and can perturb the radiative balance through their direct effects of scattering and absorption mechanisms of the solar radiation (IPCC, 2013), which are the functions of aerosol's size distribution, concentration, and chemical composition. These characteristics have a large variability along the year and depend on aerosol sources and transport processes.

Aerosol also has a main indirect effect on the radiative budget. It concerns the modification of cloud microphysics and then clouds albedo and lifetime (Albrecht, 1989; Pincus and Baker, 1994). Indeed, aerosol particles can act as cloud condensation nuclei (CCN), leading to the formation of a larger number of water droplets that increase the reflectivity of clouds. The IPCC, (2013) Report estimates that the direct effects account for an overall cooling forcing of about $-0.35\,\mathrm{W\,m^{-2}}$, with a large uncertainty ($\pm 0.5\,\mathrm{W\,m^{-2}}$). A similar cooling forcing ($-0.4\,\mathrm{W\,m^{-2}}$) is also exerted by the indirect effects,

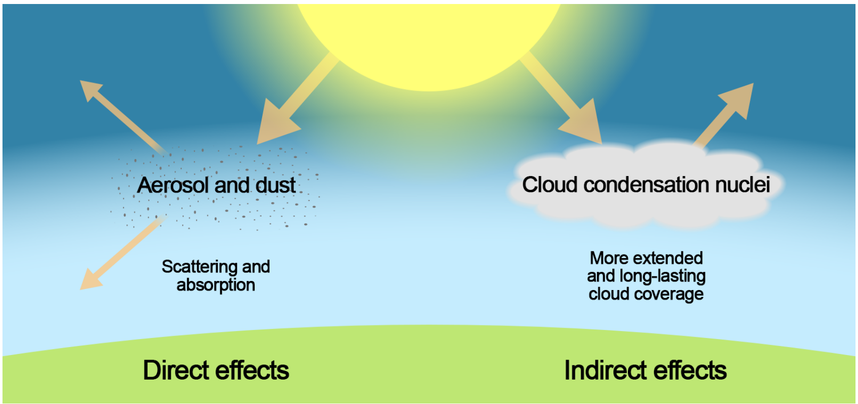

Figure 1.2 – Direct and indirect effects of the presence of atmospheric aerosols on the Earth's radiative budget.

with an even higher uncertainty. As also highlighted in relevant recent works (Carslaw et al., 2013), the largest uncertainty in the forcing exerted by atmospheric aerosol is related to the natural sources. The ultimate magnitude of the aerosol relative forcing depends on the weight of direct and indirect effects, but such uncertainties are so large to make uncertain the sign of the forcing as well. Thus, to reduce the uncertainty about this climate-forcing factor and to better understand the influence of human contribution, it is particularly relevant to study the current aerosol features in terms of atmospheric load, chemical composition, and physical properties.

1.3 The Arctic

The influence of climate forcings is particularly relevant in the Arctic because it is one of the most sensitive environments to climate perturbations. Indeed, the present climate change is affecting the Arctic more than other areas on the planet because of positive feedback mechanisms, leading to the rise of Arctic mean temperature almost twice the global increase in recent decades (Serreze and Francis, 2006; Winton, 2006; IPCC, 2013). This effect, called *Arctic amplification* (fig. 1.3), is the result of complex feedback mechanisms (Pithan and Mauritsen, 2014), mainly ascribed to the decrease of sea ice extent which influences the global radiative balance by reducing the surface albedo; the consequent positive feedback leads to a more rapid sea ice loss (Robock, 1983; Screen and Simmonds, 2010).

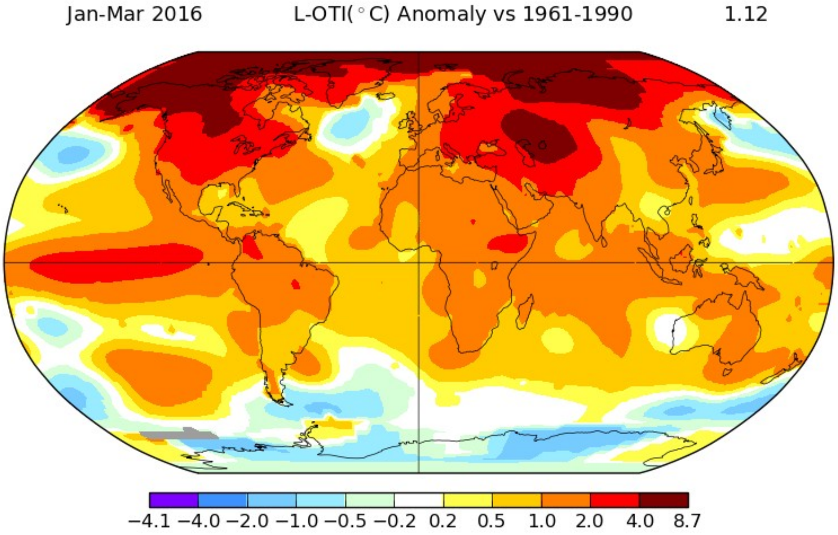

Figure 1.3 – Surface temperature anomalies (°C) for Jan-Mar 2016 with respect to a 1961-1990 baseline (NASA).

The Arctic amplification phenomenon needs in-depth investigations regarding the atmospheric aerosols contribution understanding what are its main sources and origin regions, in order to ascribe the real contribution (weight) to natural and anthropic emissions of atmospheric aerosols.

The impact of aerosol in the Arctic has proved to be highly variable during the year. The most important contribution to the Arctic

Figure 1.4 – Map of the Arctic region (Audun Igesund, NPI).

atmospheric aerosols occurs in the winter-spring period because of a phenomenon known as *Arctic Haze* (Quinn et al., 2007). This phenomenon was at the beginning attributed to natural processes affecting the atmosphere transparency but, since the late 1970s, the anthropogenic origin of the Arctic haze (via atmospheric transport of contaminants from polluted continental areas) was established by the chemical composition of the atmospheric aerosols. This tropospheric brown haze is mainly composed of a mixture of sulfate, organic atmospheric aerosols, ammonium, nitrate, dust, black carbon and heavy metals (Li and Barrie, 1993; Heintzenberg, Hansson, and Lannefors, 1981; Quinn et al., 2002), with a size distribution mainly in the accumulation mode (Shaw, 1984; Tunved, Ström, and Krejci, 2013), as expected for the secondary aerosol especially related to anthropic sources (Bazzano et al., 2016). These particles, during the winter, once transported northward from mid-latitude industrialized areas, end up in a cold and stable atmosphere, which inhibits turbulent transfers between different layers as well as the formation of clouds and precipitations, which are the major atmospheric aerosols removal ways (Iversen and Joranger, 1985). The combination of these factors results in the transport of aerosol particles to the Arctic and their persistence in the atmosphere that usually lasts until April. As a consequence of this source change, Arctic aerosol showed pronounced seasonal variations in the size distribution, with sudden changes in the chemical and physical properties between late winter-spring and summer periods above the planetary boundary layer (Ström et al., 2003; Engvall et al., 2008; Tunved, Ström, and Krejci, 2013).

Unfortunately, current global climate models are still unable to parameterize and reproduce the observed Arctic warming and the observed Arctic sea ice loss (Shindell and Faluvegi, 2009; Stroeve et al., 2007), mainly due to inadequate representation of scavenging processes, different transport mechanisms and underestimation and unknown number of aerosol sources (Stohl et al., 2013). For this reason, studies on aerosol concentrations in Arctic areas are very interesting, considering not only the lack of long-term measurements in the region (Tunved, Ström, and Krejci, 2013; Bodhaine, 1989; Asmi et al., 2015) but also the scarcity of stations due to the logistic difficulties. The active Arctic monitoring sites include: Alert (Canadian Arctic), Station Nord (Northern Greenland), Zeppelin (Svalbard Islands), Barrow (Alaska), Karasjok and Svanvic (Northern Norway), Oulanka (Northern Finland) and Janiskoski (Northern Russia) (Quinn et al., 2007).

1.4 Size distribution

When we talk about size, we often refer to aerosol particles in term of radius or diameter, implying they are spherical. In reality, particles have irregular shape and then it would not make sense to speak of radius and diameter. Thus, it is used the concept of *equivalent diameter*, whose value depends on the physical properties of the particles, rather than geometric ones. The most commonly used is the equivalent aerodynamic diameter (D_a), defined as the diameter of a sphere of unit density ($1\,\mathrm{g\,cm^{-3}}$) which has the same terminal falling speed in air as the particle under consideration. The particles of atmospheric aerosol have an equivalent aerodynamic diameter in the range 0.01 µm to 100 µm, and are separated in three different size classes: Aitken mode, from 10^{-2} µm to 0.1 µm; accumulation mode, from 0.1 µm to 1 µm; coarse mode, under 1 µm.

Particulate size distribution plays an important role in the atmospheric chemistry. In order to better understand the distribution of particles as a function of their size, it is useful to refer to three different characteristics of the particulate: concentration, surface area and volume. To better read the results, the distribution is represented in a plot showing the trend of $\Delta N/\Delta \log D$ as a function of D on logarithmic scale, where D is the equivalent aerodynamic diameter and N is the concentration of particles per cm^3 of air; in the other two cases, N is replaced by S, for the surface, and V, for the volume.

Plots in Figure 1.5 show peaks in different regions and bimodal distributions, indicating a differentiation into groups depending on origins and properties of particles. Generally particles with diameter <2.5 µm are identified as *fine* and those with diameter >2.5 µm as *coarse*. Fine particles, as seen in figure, represent the most of the total number, but just a part of the total mass, and may be divided into two

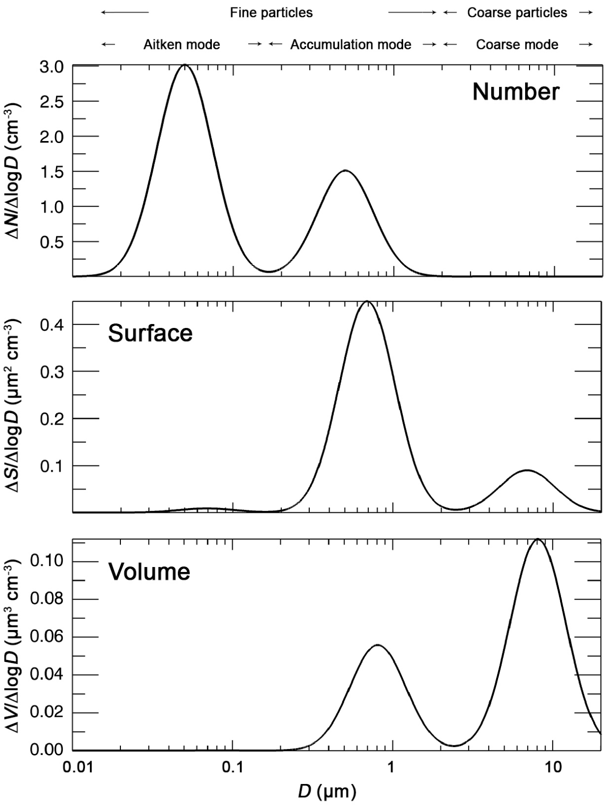

Figure 1.5 – Number, surface and volume distribution for urban aerosol (Whitby and Sverdrup, 1980).

categories: the accumulation range ($D > 0.8\,\mu m$) and Aitken range ($D < 0.8\,\mu m$). The Aitken nuclei arise from gas-to-particle conversion and from condensation of low volatility vapors from combustion processes. These particles rapidly grow in size by coagulation with each other, or acting as condensation nuclei for gaseous species with low vapor pressure, thus reaching the accumulation mode. Coarse particles instead come from mechanical processes and therefore have relatively large size and different composition, which is predominantly inorganic. Due to the different origins, the presence of coarse particles is only weakly associated with the fine component, which typically contains more organic substances and inorganic ions, such as ${NH_4}^+$, ${NO_3}^-$ and ${SO_4}^{2-}$.

1.5 Metals in the aerosol

Metals in the atmospheric aerosols represent a very useful information about the nature of the aerosol, so they deserve an in-depth analysis. Despite the small concentration of metals in the atmosphere, especially in remote sites (Maenhaut et al., 1979; Pacyna and Ottar, 1985; Mazzera et al., 2001), they bring with them very useful information about the original sources of the atmospheric aerosols (Maenhaut et al., 1989). This happens thanks to the conservative properties of the metals within atmospheric transport processes (Ferrat et al., 2011), since they maintain their original composition from the source areas to the deposition sites, even up to thousands of kilometres (Moreno et al., 2006; Pourmand, Prospero, and Sharifi, 2014), and they are not subjected to secondary transformations. For this reason, selected metals and their ratios in the atmospheric aerosols can be considered as specific markers of natural and anthropic sources. In particular with respect to atmospheric transport and transformation processes, rare earth elements (REEs) are a robust and powerful tool for the geochemical characterization of mineral dust source areas, thus allowing the assignment of the origin provenance area to the anthropogenic fraction of atmospheric aerosols.

REEs are fourteen elements, ranging from atomic number 57 (Lanthanum) to 71 (Lutetium). The physical and chemical properties are very similar and are due to their constant trivalent charge (with few exceptions) and to the gradual filling of 4f orbitals as the atomic number increases. REEs keep the same external configuration of valence electrons while the ionic radius decreases from 1.03 Å (La^{3+}) to 0.86 Å (Lu^{3+}). Thus, they behave like isotopes and this so-called Lanthanide contraction affects their chemistry, leading to their fractionation in the environment. Thanks to their low solubility and mobility in the terrestrial crust, they have a conservative behavior in the environment and their profile is like a fingerprint, reflecting the characteristics of their original area.

REEs have proved to be an excellent geochemical tool for the atmospheric aerosols source region apportionment. Many studies have been made on the aerosol mineral content and on the urban aerosol source determination using REEs (Suzuki, Suzuki, and Furuta, 2010; Moreno et al., 2010), but so far, their determination in remote sites was limited to short or low temporal resolution sampling campaigns (Pacyna et al., 1985; Wu et al., 2009; Turetta et al., 2016). Furthermore, the low availability of REEs air concentration in the scientific literature is mainly due to analytical limitations. The use of daily resolution data can provide an accurate analysis of both temporal trends and aerosol events, where anthropogenic enrichments allow to identify pollution events from southern industrialized areas, mainly due to petroleum refining operation emissions (Du and Turner, 2015; Kltto et al., 1992; Moreno et al., 2008).

Inductively coupled plasma sector field mass spectrometry (ICP-SFMS) was proved to be a capable method for the fast quantification of a large number of metals and, in particular, REEs (Zhang, Jiang, and Hu, 2006; Zhang et al., 2007), even though many parameters, from acid digestion to detection, need to be optimized in order to achieve a suitable method for samples with such a low load of analytes (Toscano et al., 2005; Kulkarni et al., 2007; Swami et al., 2001).

In this work, we analyze both the size distribution of arctic aerosol and its chemical composition. Thanks to the high temporal resolution and a large number of samples, the results are used to study the seasonal patterns of the atmospheric aerosols and to identify the kind of source and the source regions, using backward air mass trajectories and mathematical receptive models.

Chapter 2

Sampling and modeling methodologies

2.1 Ny Ålesund, the sampling site

The Arctic samples and data presented in this work were collected in many sampling campaigns in the site of Ny Ålesund (78°56′ N, 11°56′ E), in the Svalbard Islands, part of the Kingdom of Norway. This little village faces the sea in the Kongsfjorden, a fjord which develops in the northwest-southeast direction, in the west part of the Spitsbergen island (fig. 2.1). Born in the '10s of the XX century as a coal mining town, Ny Ålesund is today the northernmost permanent settlement completely dedicated to the scientific research.

The village (fig. 2.2) is managed by the *Kings Bay* company, which provides services and facilities to researchers from Universities and research institutes from all over the world and allows the village to be permanently inhabited by a minimum of 30 people in winter up to about 200 in summer. Between the ten nations with their own station, the *Italian National Research Council* (CNR) manages the Italian Arctic Station *Dirigibile Italia*, dedicated to the general

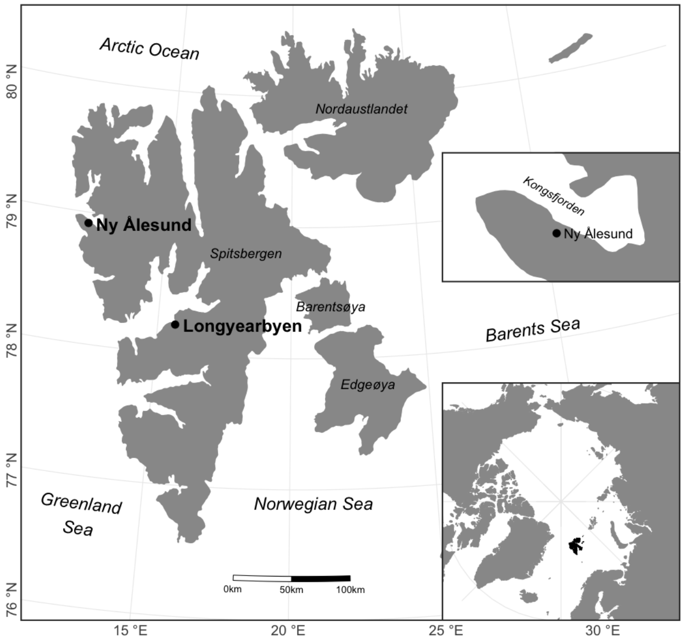

Figure 2.1 – Map and geographic position of the Svalbard Islands and detail of the Ny Ålesund area.

Umberto Nobile's airship and to his scientific expedition towards the North Pole. Part of the Italian Arctic Station structures, the *Gruvebadet* observatory (fig. 2.3a) hosts the sampling devices used for many studies about the atmospheric particulate (Viola et al., 2013; Udisti et al., 2013; Calzolai et al., 2014; Moroni et al., 2015; Bazzano et al., 2015). This observatory is active since 2010 and is located about 1 km south-west of the village in a clean area, where every motorized activity was forbidden and where its geographic location guarantees the lowest impact from the local emissions of the village, which is hit by winds blowing mainly in the same direction of the fjord. For this reason, in the samples, the anthropic impact coming from the village is negligible. The Nobile-Amundsen Climate Change Tower (CCT) is another structure run by CNR, which provide all year round meteorological data, such as temperature, pressure, wind speed and direction (Mazzola et al., 2016).

Figure 2.2 – View of Ny Ålesund facing Kongsfjorden fjord from the laboratory of Mount Zeppelin. Position of the Italian Arctic Station *Dirigibile Italia* and of the sampling site, the laboratory of *Gruvebadet*.

2.2 Sampling instrumentation

Since the beginning of the scientific activity in the observatory in 2010, every year a spring-summer campaign was carried out and the sample collection is still ongoing. In this work, samples and data from the six consecutive sampling campaign from 2010 to 2015 were considered and analyzed. The not coincident beginning and end of the campaigns are due to logistics reasons, whereas minor gaps are due to power failure or extraordinary observatory maintenance. Many are the devices in the Gruvebadet observatory for the study of the physical and chemical properties of the atmospheric particulate at ground level. Between them, the aerosol analyzed and discussed in this work was collected by many devices, for the determination of the chemical composition, and for the study of physical properties, in particular, the size distribution of the atmospheric aerosols.

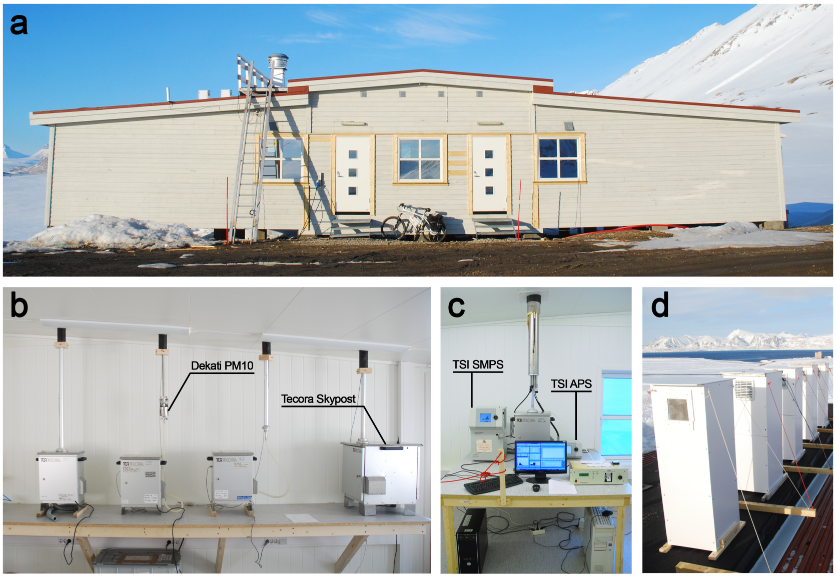

Figure 2.3 – Photos of the building of the Gruvebadet laboratory: (a) outside, (b) inside laboratory with Tecora Skypost PM device and (c) the particle counters SMPS and APS, (d) protective boxes containing the impactor heads on the roof.

2.2.1 PM$_{10}$ and size-segregated sampling

The particulate matter destined to the chemical analysis was collected by two devices. The first sampler was a *Skypost PM* (Tecora, France), shown in fig. 2.3b and in detail in 2.4, which is an automatic low-volume sampler. It was equipped with a PM_{10} head, placed on the roof of the building (fig 2.3d), and allows to collect particulate matter with an aerodynamic equivalent diameter (a.e.d.) smaller than 10 µm. The aerosol was collected by this device on Teflon filters: Pall Corporation (Michigan, USA), 47 mm diameter, 2 µm nominal porosity and capture efficiency of 99.6 % for a.e.d. ≥ 0.3 µm particles. Samplings were carried out continuously on daily basis (00:01 - 23:59 UTC) and in actual conditions, which means that pressure and temperature were monitored to maintain a constant flow rate of 38.33 L min^{-1} (EN12341), in order to not compromise the wanted cut-off value.

Figure 2.4 – Tecora Skypost PM internal detail and PM_{10} impactor head.

The second data set was consists of size-segregated samples, obtained by a four-stage Dekati PM10 multi-stage impactor (4-day resolution, 29.00 L min^{-1}, and cascade impactor, fig 2.5). Polycarbonate filters (25 mm diameter and 0.1 µm nominal porosity) were used as substrate for the first three stages (a.e.d. >10 µm, 10 - 2.5 µm, and 2.5 - 1.0 µm), while a Teflon filter collected the sub-micrometric particles (a.e.d. <1.0 µm) in the last stage.

The total number of collected during the six campaigns is 999 for

Figure 2.5 – Dekati PM10 multi-stage impactor and a step of filters loading (photo by Luca Bracali).

the PM_{10} samples and 256 for the 4-stage distribution, distributed over the years, as table 2.1 shows, with the corresponding period.

The selection of particles size is permitted by the principle of inertial impaction on the basis of differences in inertia. Accelerated through a nozzle, particles collide on the impactor plate if their linear momentum is greater than a given value, which depends on the structural features of the impactor (fig. 2.6). The particle diameter for which impactor collects with 50 % efficiency (d_{50}) is a function of air velocity (U) and nozzle impactor diameter (D_j). Thus a stable flow allows to keep constant the *cut-off* value, that means 50 % efficiency for a specific a.e.d. (fig. 2.7). This principle allows collecting particles smaller than the cut-off value in terms of a.e.d. (not of actual diameter of the particle) with the filter placed after that plate.

Table 2.1 – Period of the six sampling campaigns and number of aerosol samples collected for the daily PM_{10} and 4-stage data sets.

Year	*Start*	*End*	*PM_{10} samples*	*4-stage samples*
2010	Mar 15	Sep 23	164	42
2011	Mar 29	Sep 6	146	39
2012	Mar 23	Sep 6	163	36
2013	Mar 31	Sep 14	165	41
2014	Mar 31	Sep 9	136	40
2015	Feb 27	Oct 21	225	58

To avoid contamination from sampling to analysis, it was necessary to keep clean all the laboratory tools used to handle the filter and the sample solutions, rinsing them carefully, multiple times, with MilliQ water. Moreover, powder-free gloves were used to work with the filters and every operation was carried out under devoted laminar flow hoods in order to minimize contamination risks. Clean filters were initially manipulated before sampling in the analytical laboratory of the Italian Arctic station, provided with a laminar flow hood and water purification system for MilliQ water. All the exposed

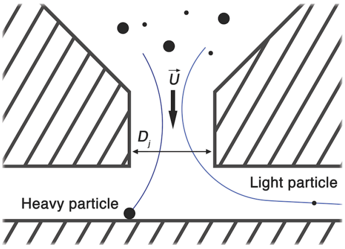

Figure 2.6 – Schematic representation of an inertial impactor.

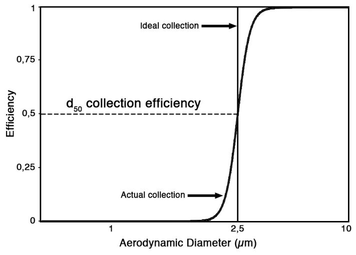

Figure 2.7 – Efficiency of an impactor with 2.5 μm cut-off.

filters were then collected within a refrigerator in the station, at a storage temperature below −20 °C, and kept at the same temperature (during transportation and conservation in a cold room) until the analysis.

2.2.2 Particle counters

The aerosol size distribution was evaluated with two commercial devices: the Scanning Mobility Particle Sizer TSI SMPS 3034 and the Aerodynamic Particle Sizer TSI APS 3321 (fig. 2.3c). The two instruments provide respectively 54 and 52 size channels equidistributed logarithmically in the diameter range between 10 nm and 20 µm, with a small uncovered gap (487 − 523 nm). Both the instruments collect data all day long throughout the duration of the sampling campaign, with a time resolution of 10 minutes, and aspirate air with a flux of 1.0 L min^{-1} from an inlet on the roof, close to the inlets of the other instruments.

During the six campaigns, a total of 152 722 and 148 829 scans have been collected respectively for SMPS and APS, distributed as shown in table 2.2. UTC time was used for all the data present in this work.

2.3 Receptor models

2.3.1 Positive Matrix Factorization analysis

The *Positive Matrix Factorization* (PMF) is a multivariate receptor modeling technique allowing the determination of the chemical profiles of the aerosol sources affecting the receptor site and the estimation of their contributions to the aerosol load. It uses as input data long time series of atmospheric concentrations of different chemical species. Briefly, PMF is an advanced factor analysis technique

Table 2.2 – Sampling periods for the sampling campaigns of the particle counters and number of samples.

Device	*Year*	*Start*	*End*	*ASD scans*	*Coverage %*
SMPS	2010	Mar 14	Sep 23	27299	98.06
	2011	Mar 26	Nov 23	32932	94.55
	2012	Jul 27	Sep 23	8313	100
	2013	Mar 27	Sep 15	24373	98.42
	2014	Mar 26	Sep 28	25709	96.21
	2015	Feb 24	Oct 22	34096	98.75
APS	2010	Mar 14	Sep 23	23928	85.95
	2011	Mar 26	Oct 18	26038	87.86
	2012	May 23	Sep 23	17612	99.52
	2013	Mar 27	Sep 15	24373	98.42
	2014	Mar 26	Sep 10	23160	95.81
	2015	Feb 28	Oct 22	33718	99.21

based on a weighted least-squares approach. The PMF method is based on the mass conservation principle:

$$x_{ij} = \sum_{k-1}^{p} g_{ik} f_{jk} + e_{ij} \qquad i = 1, 2, ..., m \qquad j = 1, 2, ...$$

where x_{ij} is the j^{th} species concentration measured in the i^{th} sample, g_{ik} is the contribution of the k^{th} source to the i^{th} sample, f_{jk} is the concentration of the j^{th} species in the k^{th} factor, and e_{ij} is the residuals associated with the j^{th} species concentration measured in the i^{th} sample. A matrix of residual errors (e_{ij}) accounts for errors in the model fit. The task of PMF is to minimize the sum of the squares of the residuals (Q) weighted inversely with the estimated uncertainties:

$$Q = \sum_{i=1}^{n} \sum_{j=1}^{m} \left(\frac{e_{ij}}{s_{ij}} \right)^2$$

where s_{ij} are the error estimates for the x_{ij} elements. It uses realistic error estimates to weigh data values and imposes non-negativity constraints in the factor computational process, with an algorithm allowing to reduce the influence of outliers. Thus, thanks to the factors achieved, species with similar affinity can be grouped together, helping to recognize common features, such as origins and transport processes.

The PMF analysis was accomplished in collaboration with the National Institute for Nuclear Physics (*Istituto Nazionale di Fisica Nucleare*, INFN) and Physics Department of the University of Florence, using the EPA PMF 5.0 software (from the U.S. Environmental Protection Agency). The PMF model was applied to the dataset of atmospheric concentration and chemical composition of the chemical species measured by IC, ICP-MS, and Particle Induced X-ray Emission (PIXE), in addition to elemental carbon concentrations (EC). All this data is relative to the 237 daily PM_{10} samples collected in the 2015 sampling campaign (from February to October). This elaboration is limited to 2015 because PIXE analysis were caddied out only for this year.

The PIXE analysis was performed by INFN on an identical set of PM_{10} samples, collected at the same site and simultaneously to those analyzed with IC and ICP-MS. This last dataset includes the information about the atmospheric concentration of 27 metals: Na, Mg, Al, Si, P, S, Cl, K, Ca, Ti, V, Cr, Mn, Fe, Ni, Cu, Zn, As, Se, Br, Rb, Sr, Y, Zr, Mo, Ba, and Pb. Since some of the metals have been analyzed by two different techniques and not all of the chemical species have proved to be useful for the PMF analysis, a selection of the species to be used as input of the model was made. This selection was based on the number of available measures for each species (both the number of samples analyzed and the number of measures above detection limit) and on the error associated with them. Since REEs did not provide sufficient variability in concentrations to meaningfully resolve factor profiles, they were put together in their two subgroups previously discussed: light and heavy REEs. Data below the detection limit (LOD) were substituted with LOD/2 and missing data were substituted with the median concentration for each species, so that the missing data will not significantly weight the results. Uncertainties were set as 400 % for PM_{10} concentration, 15 % +LOD/3 for the metals analyzed with ICP-MS and 10 % +LOD/3 for the rest, whereas for values below LOD were set as $5/6 \cdot MDL$.

2.3.2 Air backward trajectories analysis

The NOAA Hybrid Single-Particle Lagrangian Integrated Trajectory (HYSPLIT) model software (HYSPLIT4 for macOS) was used to calculate air back-trajectories for the hybrid receptor modelling (Draxler and Rolph, 1997) ending at the receptor site at 78.93° N 11.95° E. The meteorologic data used for the HYSPLIT modelling in the Arctic were the *gdas* 1° spatial resolution data files, supplied by the ARL (*Air Resources Laboratory*).

HYPLIT was run in order to have backward trajectories (BTs) four times a day (0:00, 6:00, 12:00, and 18:00) for every day of the sampling campaign periods, with the endpoint height of 500 m AGL. This height was chosen to reduce the effects of surface friction and to represent winds in the lower boundary layer. It is also the approximated height of the mixing layer and has been found to be a generally useful height (Fan et al., 1995; Gao, Cheng, and Hopke, 1993; Hafner and Hites, 2003; Hsu, Holsen, and Hopke, 2003). The final dataset consists of a total of 4370 BTs, 120-h lasting (5 days), at 1-h resolution.

The backward trajectories of air masses produced through HYSPLIT software were used to identify regional source areas contributing to the speciated atmospheric measurements in Ny Ålesund by applying the Potential Source Contribution Function (PSCF) model, using the Openair R package (R-Core-Team, 2016; Carslaw and Ropkins, 2012). The PSCF combines the chemical data with air mass back trajectories to identify potential source areas (Ara et al., 2005; Xie and Berkowitz, 2007).

The PSCF values for the longitude-latitude grid cells in the study domain are calculated by counting the trajectory segment endpoints that pass through each cell. The model assumes that a species emitted within a grid cell is swept into the air parcel and transported to the receptor site without loss through diffusion, chemical transformation or atmospheric scavenging. The movement of an air parcel is described as segment endpoints of coordinates in terms of latitude and longitude; the total number of endpoints that fall in the ijth cell is n_{ij}. The number of endpoints for a given cell having arrival times at the sampling site and corresponding to a chemical species concentration higher than an arbitrarily set criterion is defined to be m_{ij}. The PSCF value for the ijth cell is then defined as

$$PSCF_{ij} = \frac{m_{ij}}{n_{ij}}$$

The PSCF value can be interpreted as the conditional probability that the concentrations of a given analyte greater than the criterion level are related to the passage of air parcels through the ijth cell during transport to the receptor site. That is, cells with high PSCF values are associated with the arrival of air parcels at the receptor site that have concentrations of the analyte higher than the criterion value.

These cells are indicative of areas of high potential contributions for the constituent. The threshold value in our case was the 90th percentile of the selected pollutant.

The error associated with the trajectory path increases as the distance from the receptor site increases (Stohl, 1996). In this trajectory approach, the method looks at the collective properties of a large number of endpoints. If the errors in the trajectory endpoint locations are randomly distributed, then for a sufficient number of endpoints distributed over the region of interest, the PSCF values will approach to the true values.

The limitations of the PSCF method are that (i) grid cells can have the same PSCF value when sample concentrations are either only slightly higher or much higher than the criterion and (ii) small values of n_{ij} (i.e. few back-trajectories) can produce high PSCF values with high uncertainties given the small number statistics, making difficult to distinguish moderate sources (sporadic events) from strong ones (seasonal), this effect is also called *tailing effect.* For this reason and to minimize these limitations, the PSCF method is often combined with an empirical weight function originally proposed by Zeng and Hopke, (1989), which reduce the PSCF value for cells with fewer endpoints than a given number.

Chapter 3

Analysis and results

3.1 Size distribution of ultra-fine aerosol

3.1.1 Data analysis

86 388 ultra-fine aerosol size distribution (ASD) scans collected between 2010 and 2014 were deeply analyzed. At the beginning and using the wind data of the CCT, the whole dataset was cleaned, removing data gathered during March and September (mainly due to the total temporal inhomogeneity of these months) and hourly average ASD characterized by wind from the so-called *contaminated sector*, consisting in wind coming from the village direction (Järvinen et al., 2013), a sector defined as wind direction in the range from $22°30'$ to $67°30'$. The dataset consists finally in a total of 12.465 h. The monthly percentage was partitioned in different values, around 20 %: the April dataset consisted of 20.8 % of averaged ASD, May 23.4 %, June 20.3 %, July 19.6 % and August 15.9 %. All the ASD retrieved were analyzed in terms of total number concentration, dividing them into Nuclei, Aitken and Accumulation mode concentration, where Nucleation mode, Aitken mode and Accumulation mode ranges

refer to the spectrum of predefined size intervals measuring <25 nm, between 25 and 100 nm and >100 nm, respectively (Dal Maso et al., 2005).

Figure 3.1a presents the median and mean number, surface and volume concentrations of the four campaigns to compare and check inter-annual coherence. The number distribution was bimodal for all the results: for the various median ASD, they have peaks slightly larger than 0.30 µm in the Aitken region, and around 0.15 µm in the Accumulation region; for the mean ASD, we found peaks between Nuclei and Aitken (0.2 - 0.3 µm), while the mean Accumulation peaks are quite similar to the median ones.

An analysis of the Nuclei/Aitken region suggest a strong inter-annual variability, presumably due to new particle formation (NPF) events, when ultra-fine particles aggregate with each other and grow in size up to about 0.1 µm, as seen in the event of September 27, 2014, in figure 3.2. A different behavior appears looking at the surface and volume concentration: the surface distribution is also bimodal, with a strong mode common to mean and median regions in the range (0.20 - 0.30 µm), and a weak mode in the Aitken region around 0.05 µm. A mono-modal curve characterizes the volume distribution, which is similar in both mean and median peaks, centered around 0.20 - 0.30 µm.

Figure 3.1b shows a monthly median and mean number size distribution: this plot underscores the strong monthly variation in number modal concentration (diminishing from spring to summer) and modal geometric diameter (moving towards lower values in the Accumulation region), passing from spring to summer, approaching autumn.

Total particle number concentration (fig. 3.3a) shows an almost stable median number during the months (from 201 particles cm^{-3} in April to 262 part cm^{-3} in July), while shifting to mean values

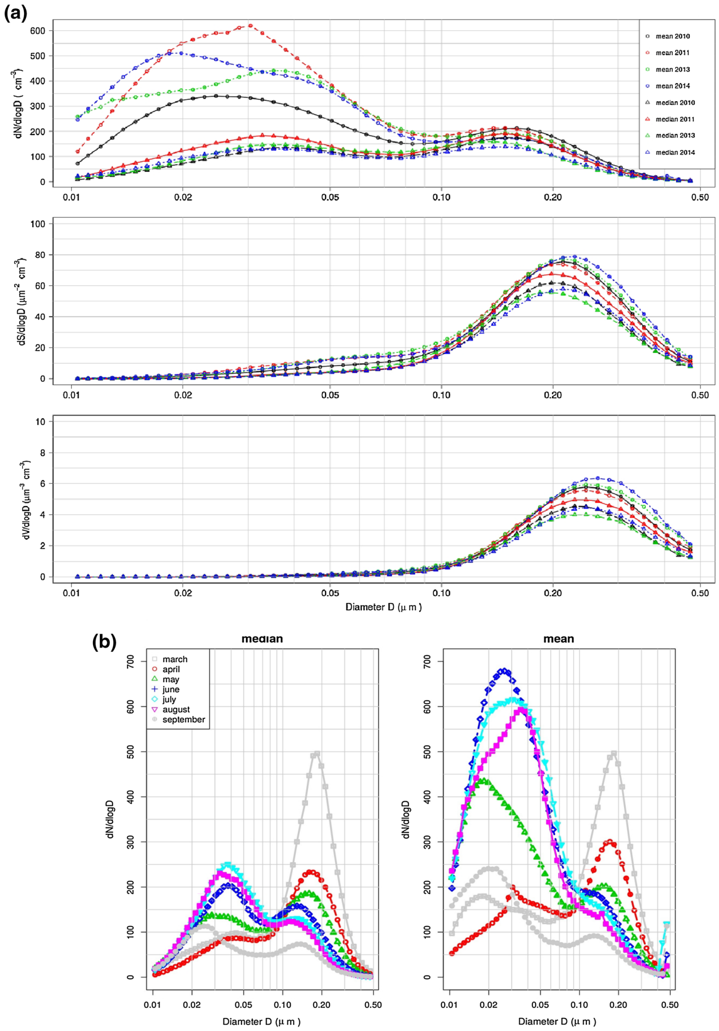

Figure 3.1 – *a* Mean (open circle) and median (open triangle) ASD,c surface ASD and volume ASD during each campaign (open circle for mean and open triangle for median values, respectively). Mean values are always greater than corresponding median values; *b* Monthly median and mean number size distribution evaluated during the four campaigns. The gray symbols refer to the months of March and September, characterized by non-continuous measurements.

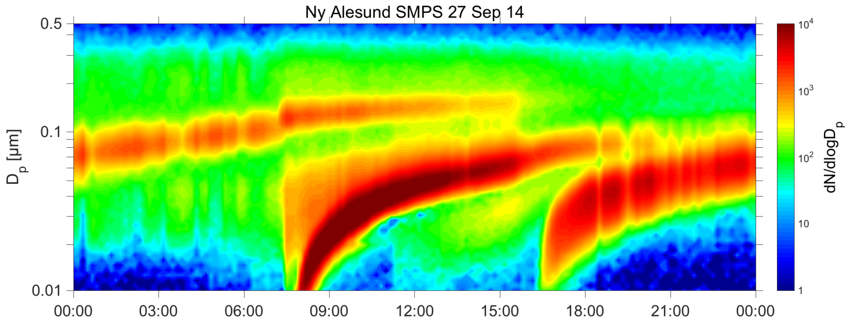

Figure 3.2 – New particle formation event occurred on September 27, 2014 at Ny Ålesund.

and to percentile ranges the seasonal dependence becomes more evident (from 248 part cm^{-3} during April, to 528/524 part cm^{-3} in July/August, respectively). This seasonal variation is confirmed also considering the Nuclei number concentration (fig. 3.3b), with median values ranging from 8 part cm^{-3} in April to 26/27 part cm^{-3} during the summer months of July and August. The corresponding mean values also present a minimum during April (26 part cm^{-3}), and maximum values during the summer months (136, 130 and 122 part cm^{-3} during June, July and August). This seasonal dependence is confirmed considering the Aitken particle concentration (fig. 3.3c), with median values ranging from 64 part cm^{-3} in April to reach values of 158 during July. This increment is also confirmed looking at the mean values, where we find 106 part cm^{-3} in April and 328 part cm^{-3} in July. The opposite behavior was recorded observing the median and mean maximum concentrations of Accumulation particle numbers (fig. 3.3d) recorded in April (97 and 116 part cm^{-3}, respectively), and the minimum values recorded in August (42 and 53 part cm^{-3}). Together with mean and median values, fig. 3.4 also shows the 5/95 and 25/75 percentile ranges which are very broad, corroborating the wide range of variability.

Investigating the predominance of modal particles, the months considered disclosed a clear variation in the ultra-fine particle population. Table 3.1 shows a clear predominance of Accumulation particles during April (47 and 57 % mean and median, respectively), then decreasing during the year, reaching a plateau around 12 and 20 %. Correspondingly, the Aitken percentage increased starting from percentages ranging around 38 - 42 % to reach a sort of plateau during the summer months over 60 %. In addition to Aitken, the Nuclei population is characterized by an increase, with values around 5 - 11 % in April, reaching 25 % and around 12 % (mean and median, respectively) during the summer months when we encountered the largest difference between mean and median values, due to the diurnal high data variability.

Table 3.1 – Monthly mean and median modal concentration percentages measured during the four campaigns.

Month	*% Accumulat.*		*% Aitken*		*% Nuclei*	
	Median	*Mean*	*Median*	*Mean*	*Median*	*Mean*
April	57.2	47.0	38.0	42.2	4.8	10.6
May	37.1	20.8	51.7	49.6	11.2	29.6
June	27.0	12.8	63.0	61.4	10.0	25.8
July	20.3	12.5	68.4	62.6	11.3	24.9
August	19.7	11.8	67.4	61.2	12.9	27.0

Other Arctic particle concentrations showed the same seasonal features, presenting a median annual oscillation between 50 and 200 part cm^{-3} at the Zeppelin observatory in the range 20 - 630 nm (Tunved, Ström, and Krejci, 2013). Considerably higher median values were measured at Tiksi (Asmi et al., 2015), with values ranging from 184 to 724 part cm^{-3}, considering a differential mobility parti-

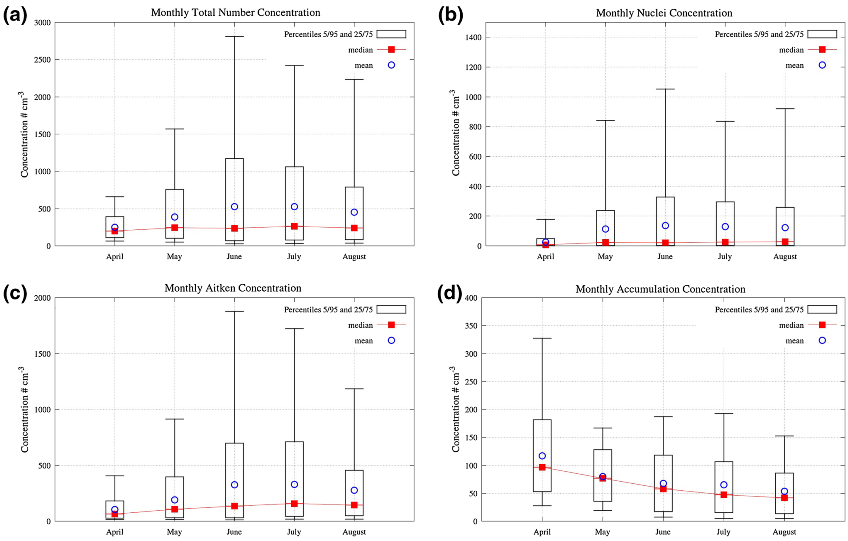

Figure 3.3 – Monthly mean and median total, Nuclei, Aitken and Accumulation number concentration: mean values are indicated with blue open circles and median values with red solid squares. The values of 5/95 and 25/75 percentiles are also indicated with whiskey bars. Please note the different scale on the y axis.

cle sizer (DMPS) range 7 - 500 nm. At Barrow, Bodhaine, (1989) measured CN concentration in the range 20 - 2000 part cm^{-3}, while median values around 30 and 60 part cm^{-3} were recorded in the late summer of 1991 during a cruise in the northern ocean (Covert et al., 1996). The geometric mean diameter (GMD) illustrates the weighted mean of the size distribution (Moorthy et al., 2011) and is defined by

$$\log(GMD) = \frac{\sum_1^m \log D_j}{\sum_1^m n_j}$$

where: n_j is the concentration number for each diameter class D_j and m is the instrumental class size. The usefulness of the GMD consists in its independence of the total number concentration, and its

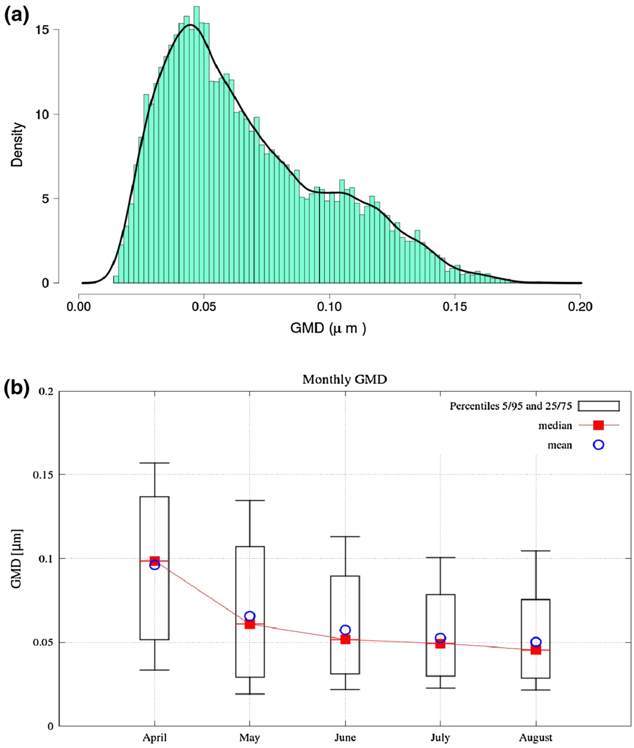

Figure 3.4 – *a* Relative frequency of GMD together with the computed density function (thick black line); *b* Monthly mean and median GMD (mean is indicated with open blue circles and median with solid red squares).

dependence only on the modal characteristics of the ASD considered, allowing the exploitation of few parameters to describe and compare ASD. Figure 3.4b reveals the monthly values of the mean and median GMD, including the 5/95 and 25/75 percentile ranges. The data clearly show the GMD decrease during the part of the year considered, with mean and median values very close to each other: from April to August, the GMD median practically halves, dropping from 0.098 µm in April, showing an intermediate value in May (0.061 µm), and more or less stable values during the three summer months (0.052, 0.049

and 0.045 µm for June, July and August, respectively). Figure 3.4a shows the frequency distribution of GMD, characterized by a clear bimodal feature, suggesting two well-defined GMD population types (centered around 0.049 and 0.11 µm). Well-defined patterns are clearly visible in fig. 3.5. Figure 3.5a shows mean daily values of Accumulation number percentage covariating with the relative daily values of GMD: a parabolic fitting is also displayed with a correlation value $r^2 = 0.81$ (the relative fitted parabolic coefficients have values equal to: $a = 5.1 \times 10^{-6}$, $b = 6.7 \times 10^{-4}$, and $c = 3.4 \times 10^{-2}$). The day of the year was depicted to emphasize the time dependence of covariance between GMD and percentages. Figure 3.5b and c, (both visualized in fig. 3.5d) represents the same curves for Aitken and Nuclei mode: the usefulness of this kind of graph lies in detecting strong NPF events, especially during the spring when focusing on the lowest GMD value.

In the two 2D color plots reported in figure 3.6, the particle counts for each instrument in April 6 - September 15, 2014 period are shown. The APS plot (fig. 3.6a) shows the highest particle concentration in the 0.5 - 1.0 µm range in spring. Starting from the end of April, the sub-micrometric and micrometric particles decrease down to very low summer values. By taking April 28th as border line, before and after this date, the distribution peaked at 723 nm (diameter midpoint of the size class), but the average concentration of the period after April 28th is 20 times lower (fig. 3.7).

In the same period, SMPS plot (fig. 3.6b) showed an abrupt change in the size distribution. In the first period, particles peaked at 184 nm and their atmospheric concentration was relatively constant ($dN/dlogD_p$ around 103). Since late April, the new particle formation (NPF) events appear to be the dominant mode of the atmospheric aerosol, with short and well-characterized (banana shaped) NPF events. The previous study carried out at Zeppelin (Ny Ålesund)

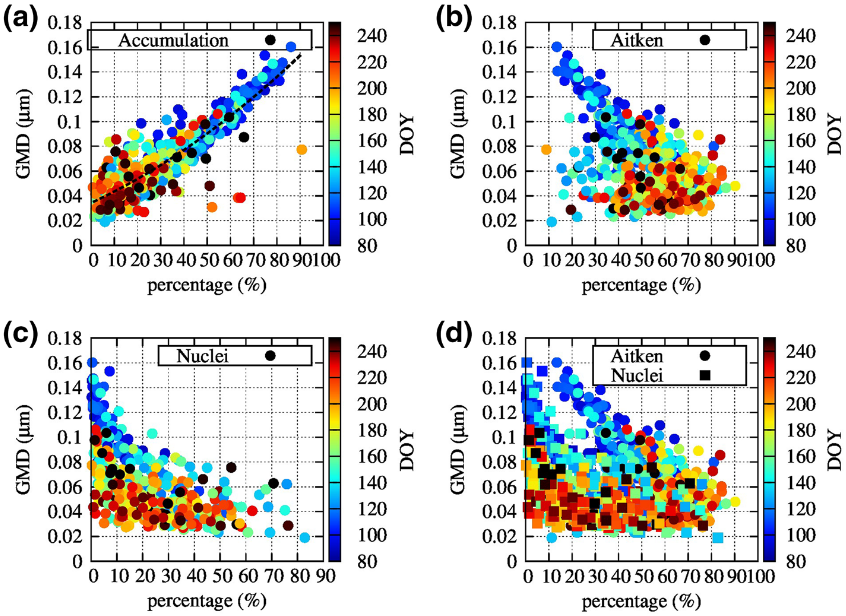

Figure 3.5 – Scatter plot of GMD mean daily values versus number percentages of different classes [Accumulation (*a*), Aitken (*b*), Nuclei (*c*) and a combination (Aitken-Nuclei)]: the color scale is a function of the Day of the Year (DOY); *a* contains the parabolic curve which fits the GMD as a function of number accumulation percentage.

showed that new particle formation events seem to be a rather common phenomenon during the Arctic summer, and this is the result of both the photochemical production of nucleating/condensing species and low condensation sink (Tunved, Ström, and Krejci, 2013). Based on the visual analysis described by Dal Maso et al., (2005), during the sampling period (163 days), 50 clear NPF events were identified starting from the end of April. Besides, in many cases, the nucleation started under the lower size class of the instrument (10 nm); on average, the particles grew up to 20 - 40 nm. Since in springtime and summertime, the sun is always present; during the day, the particle formations did not have a preferential time of the

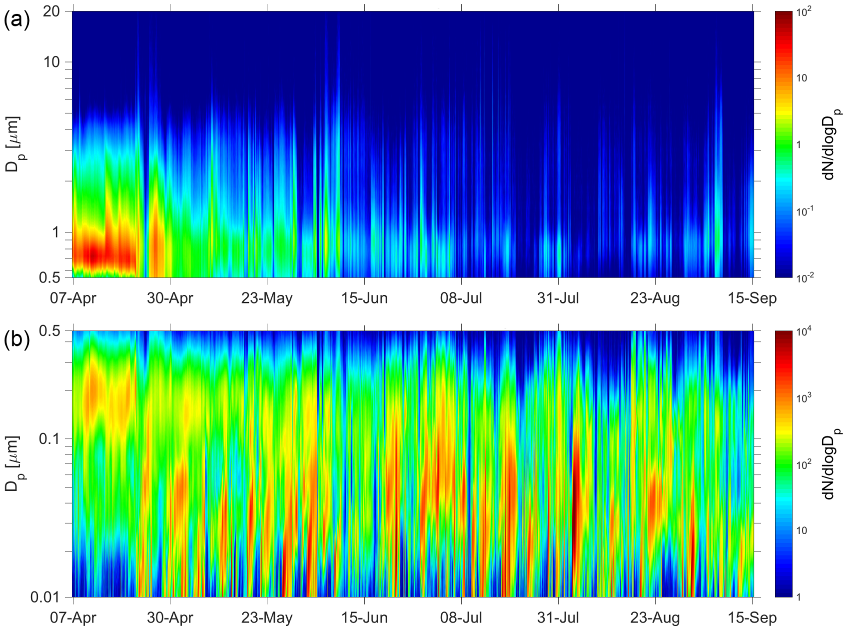

Figure 3.6 – 3D color plots from APS (*a*) and SMPS (*b*) particle-counter data, showing the aerosol size distribution along the whole 2013 campaign. The number of particles (expressed as $dN/dlogD_p$) is plotted as a function of their mobility diameter for SMPS and aerodynamic equivalent diameter (a.e.d.) for APS.

day to begin, whereas the events lasted for 2 - 24 h.

This seasonal pattern of NPF events can be due to the more sunlight presence during May-June and less abundant preexisting accumulation mode particles. This allows the newly formed particles to grow into a large enough size that the particle lasts into the following day. These processes happen until August. The summer months are all characterized by high insolation, low aerosol surface (and mass), and a much higher fraction of open ocean. In September, as days become shorter and solar radiation decreases, the particle production ceases and the period of dominating accumulation mode

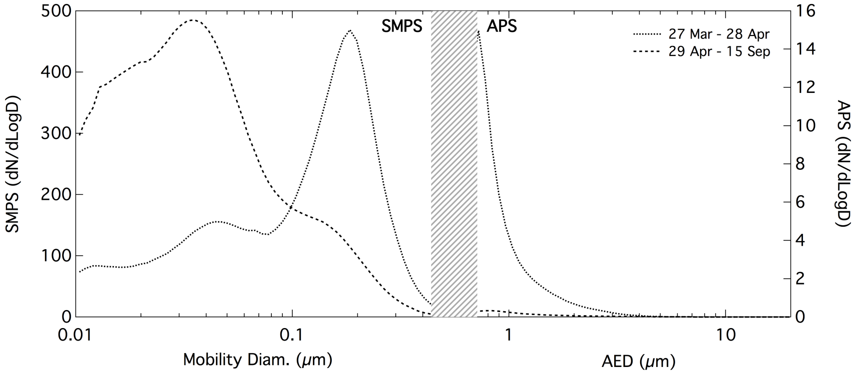

Figure 3.7 – Average size distribution in two different periods; dashed area represents the uncovered gap between the SMPS's upper channel and the APS's lower one in addition to the low-efficiency channels of APS.

is going to be re-established. This again indicates the importance of photochemical production as the main driver for new particle formation in the Arctic environment rather than sea salt aerosol. Indeed, a comparison of sea salt aerosol content with new particle formation events showed no correlation between nucleation and daily marine primary emission.

3.2 Ion composition

3.2.1 Sample handling and instrumentation

PM_{10} mass was measured by weighing the daily Teflon filters with a microbalance (0.01 mg sensitivity) before and after exposure. The filters were conditioned at low humidity with silica gel and controlled temperature ($25 \pm 1\,^{\circ}C$) for at least 24 h before the weighing. Successively, the atmospheric concentration of the particulate matter was calculated using the actual sampled volumes.

To minimize contamination risks, samples were handled inside a Clean Room class-10 000, under a devoted laminar flow hood class-100 (it guarantees less than 100 particles larger than 0.5 µm in each cubic foot of air), using powder-free gloves. At the analysis time, each filter (both Teflon and polycarbonate) were cut in halves with a stainless-steel blade and one half of each PM_{10} Teflon filter was extracted in about 12 mL of ultrapure water (MilliQ, 18 MΩ cm, exactly determined by weighing) by ultrasonic bath for 15 min, for the soluble components extraction.

Analysis was performed using three chromatographic systems, respectively, set up for the determination of cations (Na^+, ${NH_4}^+$, K^+, Mg^{2+}, and Ca^{2+}), inorganic anions (F^-, Cl^-, ${NO_2}^-$, Br^-, ${NO_3}^-$, and ${SO_4}^{2-}$), and selected organic anions (acetate, glycolate, propionate, formate, methanesulfonate, pyruvate, and ${C_2O_4}^{2-}$). Ion chromatographic conditions and the settings of the instruments are reported in table 3.2. The three chromatographs were simultaneously controlled through the dedicated software *Chromeleon*.

To quantify the ion concentrations, a six-standard calibration curve was daily used for quantification of each species. The curves were built by using standards, made by successive dilutions from $1000\,mg\,L^{-1}$ certified Merck standard solutions (Darmstadt, Germany). The preparation of the standard solutions, as well as of the

Table 3.2 – Settings summary of the three chromatographic systems.

	Cations	*Inorganic anions*	*Organic anions*
Chromatograph	ICS-1000	ICS-1000	DX-500
Sample injection	Peristaltic pump	Peristaltic pump	Peristaltic pump
Flow	$1.6\,\mathrm{mL\,min^{-1}}$	$1.6\,\mathrm{mL\,min^{-1}}$	$1.6\,\mathrm{mL\,min^{-1}}$
Duration	1.4 min	1 min	1 min
Preconcentr. or loop	800 µL	IonPac TAC-2 3 x 35 mm	IonPac TAC-2 3 x 35 mm
Guard column	IonPac CG 12 4 x 50 mm	IonPac AG11 4 x 50 mm	IonPac AG 4A 4 x 50 mm
Column	IonPac CS 12A 4 x 250 mm	IonPac AS 12A 4 x 250 mm	IonPac AS11 4 x 250 mm
Cleaning solution			(a) $Na_2B_4O_7 \cdot 10\,H_2O$ 45 mM
Eluents	H_2SO_4 22.5 mN	${CO_3}^{2-}/{HCO_3}^{-}$ 2.5 mM	(b) $Na_2B_4O_7 \cdot 10\,H_2O$ 1.9 mM
			(c) MilliQ water
Flow	$1.5\,\mathrm{mL\,min^{-1}}$	$2.0\,\mathrm{mL\,min^{-1}}$	$1.6\,\mathrm{mL\,min^{-1}}$
Eluition	Isocratic	Isocratic	Gradient
Suppressor	CSRS-300 4 mm	ASRS-300 4 mm	ASRS-Ultra II 4 mm
Regenerant	H_2O	H_2O	H_2O
Detector	Conductimetric CD 20	Conductimetric CD 20	Conductimetric CD 20
Analysis duration	10.7 min	10.5 min	10.2 min

eluents and the regenerant solution for the conductivity suppression, was accomplished using MilliQ water. In this three-system simultaneous analysis, thoughts have been made in the development of the method in order to (1) avoid memory effects between consecutive analysis for both the loop and the two preconcentrators, (2) avoid acidification of the eluent due to the presence of CO_2 in the air, preparing and keeping the solutions under N_2 atmosphere and (3) improve the separation of the organic anions, using a gradient elution of tetraborate/water. The detection limits in the atmosphere and blank values of the main ion species for the used analytical method are reported in table 3.3. The atmospheric values are evaluated considering a mean dilution volume of 12 mL and a sampled actual volume of 55 m^3 and 155 m^3 for daily samples and four-stage samples respectively.

3.2.2 Datasets consistency

High temporal resolution for the total PM_{10} and four-stage impactor data for the campaign of 2013 was tested for internal consistency. For each component, the comparison was made between the concentration of PM_{10} samples (averaged over 4 days) and the sum of the concentration measured in the 10 - 2.5 µm, 2.5 - 1.0 µm, and $<$ 1.0 µm stages. Despite the difference between the two sampling devices (efficiency and size separation system), a close similarity in concentration levels was observed along the whole time period for almost all the species, with a discrepancy lower than 16 % for the main species (tab. 3.4), that is justified by the uncertainty of the slope and the analytical method. Larger differences were found for species present in the samples at very low concentrations, likely because of larger uncertainties in evaluating blank values in the four-stage samples. The proved consistency of the two considered

Table 3.3 – Detection limits and blank values expressed in ng m^{-3} for the PM_{10} samples collected on Teflon filters (mean sampling volume = 55 m^3) and for the four-stage samples collected on Teflon filter and polycarbonate (PC) membrane (mean sampling volume = 155 m^3).

Species	*PM_{10}* ng m^{-3}		*4-stage* ng m^{-3}		
	d.l.	*Blank Teflon*	*d.l.*	*Blank Teflon*	*Blank PC*
Na^+	0.04	6.24	0.01	2.21	0.26
NH_4^+	0.09	0.07	0.03	0.03	0.09
K^+	0.01	4.18	< 0.01	1.48	0.03
Mg^{2+}	0.04	0.20	0.02	0.07	0.01
Ca^{2+}	0.02	1.39	0.01	0.49	0.02
Cl^-	0.08	7.88	0.03	2.80	0.04
NO_2^-	/	11.01	/	3.91	0.37
Br^-	0.07	d.l.	0.02	d.l.	d.l.
NO_3^-	0.07	3.11	0.02	1.10	0.03
SO_4^{2-}	0.08	0.74	0.03	0.26	0.18
$C_2O_4^{2-}$	0.19	d.l.	0.07	d.l.	d.l.
F^-	0.01	0.02	< 0.01	0.01	0.02
Ac	0.11	d.l.	0.04	d.l.	d.l.
Gly	0.04	d.l.	0.01	d.l.	d.l.
Prop	0.09	d.l.	0.03	d.l.	d.l.
Form	0.23	0.36	0.08	0.13	0.02
MSA	0.01	d.l.	< 0.01	d.l.	d.l.
Pyr	0.12	d.l.	0.04	d.l.	d.l.

independent datasets supports the reliability of the used sampling methods allowing the use of them both to infer information on the content and size distribution of the differently determined chemical markers.

The atmospheric concentration of daily PM_{10} showed that most of the particulate matter ionic composition (over 95 %) was represented by Cl^- (30.5 %), ${SO_4}^{2-}$ (26.5 %), Na^+ (23.1 %), ${NH_4}^+$ (5.8 %), Mg^{2+} (2.8 %), ${NO_3}^-$ (2.7 %), MSA (2.4 %), and Ca^{2+} (1.9 %), whereas the others (each one accounting for much less than 2 % of the total PM_{10} budget) composed the remaining 4.3 %.

3.2.3 Sea salt aerosol

Within the Arctic aerosol, Na^+ and Ca^{2+}, originate from both sea spray and crustal sources, cannot be used as univocal sea spray and crustal markers respectively. Sodium, chloride, and magnesium are the main components of the sea spray source, whereas minor contributions are represented by potassium, calcium, and sulfate. Since all these components have other sources than seawater, their sea-salt (ss-) fractions were calculated using ss-Na^+ as specific marker and knowing the X/ss-Na^+ weight/weight (w/w) ratios in seawater of each X component (Kulshrestha et al., 1996; Das, Das, and Misra, 2005): 0.036 for K^+, 0.129 for Mg^{2+}, 0.038 for Ca^{2+}, 1.81 for Cl^-, and 0.253 for ${SO_4}^{2-}$ (Henderson and Henderson, 2009). The non-sea-salt (nss-) fraction of every component was evaluated as the difference from its total concentration in the aerosol and the sea salt contribute

$$totX = ssX + nssX$$

In order to calculate the ss-Na^+ used as reference, the Ca^{2+}/Na^+ w/w ratio in seawater (Riley and Chester, 1971) and the Na^+/Ca^{2+} w/w ratio in the uppermost Earth crust (Bowen, 1979) were used

Table 3.4 – Linear correlation between daily PM_{10} and reconstructed PM_{10} from four-stage samples for the main species; their mean values and mass percentage in the measured soluble fraction in the daily samples and size distribution in the four stages.

Species	*Linear correlation*		*PM_{10} mean*	*% in PM_{10}*	*Size distribution*			
	Slope	R^2	(ng m^{-3})	*(solub. part)*	< 1 µm	1 - 2.5	2.5 - 10	> 10 µm
Na^+	1.16 ± 0.03	0.98	253.7	23.1	17.8	39.9	34.3	8.8
$NH_4{}^+$	0.91 ± 0.04	0.94	63.7	5.8	94.0	3.8	1.7	0.6
Mg^{2+}	1.07 ± 0.04	0.95	30.4	2.8	18.7	41.1	32.5	7.7
Ca^{2+}	1.13 ± 0.06	0.89	20.6	1.9	36.7	29.5	25.2	8.6
Cl^-	1.03 ± 0.04	0.94	335.6	30.5	9.5	38.3	42.0	10.3
$NO_3{}^-$	0.95 ± 0.04	0.93	29.4	2.7	15.6	53.5	27.6	3.4
$SO_4{}^{2-}$	0.92 ± 0.03	0.97	290.8	26.5	82.0	10.2	6.3	1.5
MSA	1.15 ± 0.05	0.94	26.0	2.4	83.5	10.4	4.5	1.6

in a four-variable, four-equation system (Röthlisberger et al., 2002; Udisti et al., 2012):

$$tot\mathrm{Na}^+ = ss\mathrm{Na}^+ + nss\mathrm{Na}^+$$

$$tot\mathrm{Ca}^{2+} = ss\mathrm{Ca}^{2+} + nss\mathrm{Ca}^{2+}$$

$$\left(\frac{\mathrm{Na}^+}{\mathrm{Ca}^{2+}}\right)_{crust} = 0.562$$

$$\left(\frac{\mathrm{Ca}^{2+}}{\mathrm{Na}^+}\right)_{seawater} = 0.038$$

More than 96 % of the total Na^+, Cl^-, and Mg^{2+} mass in PM_{10} was originated by sea spray; conversely, Ca^{2+}, K^+, and ${\mathrm{SO}_4}^{2-}$ have relevant contributions from other sources, especially crustal aerosol (Ca^{2+}) and anthropic emissions (${\mathrm{SO}_4}^{2-}$, K^+) by long-range transport from continental regions (Fisher et al., 2011). Sea salt aerosol was calculated by the sum of the sea salt fraction of Na^+, Mg^{2+}, Ca^{2+}, K^+, ${\mathrm{SO}_4}^{2-}$, and Cl^-. On average, the sea salt fraction of the water-soluble part of PM_{10} accounts for a mean of 60 % of the total PM_{10} mass.

The multi-stage impactor data showed that the sea spray content, marked by ss-Na^+, is mainly distributed in the 1.0 - 2.5 µm fraction (44.2 %), whereas its fractions in the 2.5 - 10 µm range and in the sub-micrometric particles were, respectively, 28.3 and 24.3 %; only 3.2 % of ss-Na^+ was present in the coarse particles (above 10 µm).

The temporal trend of ss-Na^+ does not show any clear seasonality both in PM_{10} and in the micrometric size classes by multi-stage impactor (fig. 3.8 for 2013). On the contrary, the temporal profile of the sub-micrometric fraction shows significantly higher concentrations in spring, with respect to relatively low summer values.

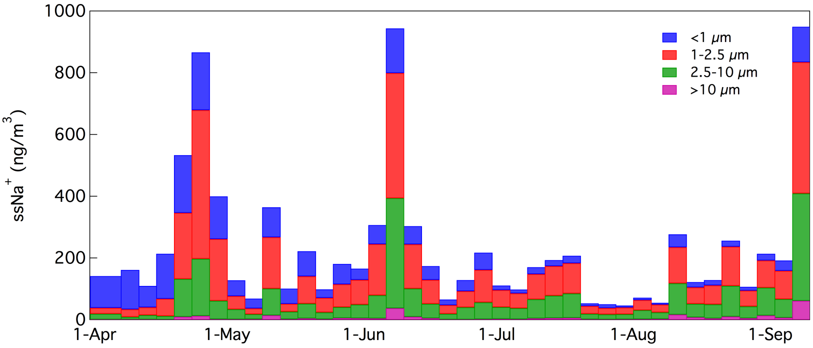

Figure 3.8 – Temporal profile of ss-Na$^+$ in the four size classes, during the campaign of 2013. The temporal resolution is 4 days.

The dominance of the sub-micrometric mode even in the sea-salt particles in spring could be justified by their settling processes during the atmospheric transport. For the same period, we observed large concentrations of nss-sulfate (see later), coming from continental areas as a component of Arctic Haze. It is likely that, during the transport of such air masses, they can be enriched in sea spray along the route over marine sectors.

Differences in sea spray size distribution along the sampling period (fig. 3.8) can be attributed to differences in atmospheric pathways supplying sea salt to Ny Ålesund. To enlighten specific transport processes, a 72-h back-trajectory analysis was carried out on selected time periods (fig. 3.9a–d). For each sample, covering a 4-day sampling period, four 500-m back-trajectories were drawn with arrival at Ny Ålesund day by day. On April 10, 2013, the chemical analysis showed low values of sea salt and a relatively large concentration of ss-Na$^+$ in the sub-micrometric range. Three out of four back-trajectories (fig. 3.9a) traveled over sea-ice areas and, presumably were not supplied by sea-salt, even if their pathways were at low altitude. In contrast, the air masses arriving at Ny Ålesund on April 9, 2013 (blue line) traveled over open sea areas; in particular, air masses were at sea level for the first day and then at about 1000 m in the following 3 days. In this way, the low concentration of sea spray and the shift of the particle size toward the sub-micrometric mode (by settling in abrupt altitude change and along the transport) could be explained. On the other hand, the three major sea spray events occurred on April 26, June 9, and September 9, 2013 (fig. 3.8), show that ss-Na^+ is mainly distributed in the super-micrometric stages (especially in the 1.0 - 2.5 µm range). The corresponding back trajectories (fig. 3.9b–d) revealed that air masses traveled over open-sea areas and at very low altitude at least 2 days before reaching Ny Ålesund. In this way, air masses were enriched in coarse sea spray particles.

3.2.4 Ion balance

Figure 3.10 shows the ionic balances (expressed as $\mathrm{nEq\,m^{-3}}$) of the PM_{10} aerosol samples collected in Ny Ålesund during the spring-summer 2014 campaign (136 samples). The ionic composition is dominated by two main components: sea spray (marked by Na^+, Cl^-, Mg^{2+} and, partially, ${SO_4}^{2-}$) and secondary aerosol (marked by sulfate, ammonium, nitrate, and nitrite). The all-period (total) plot shows that Na^+ and ${NH_4}^+$ were the major cations, accounting for 51 and 25 % of the cation content, respectively. In the same way, chloride and sulfate dominate the anion budget (45 and 38 %, respectively). Such components, however, are not equally distributed in the spring and summer samples, showing a sharp seasonal pattern. Indeed, sulfate and ammonium show the highest contribution (both in absolute quantity and in ion percentage) in spring. In this season, ${NH_4}^+$ accounts for 30 % of the cation budget, while ${SO_4}^{2-}$

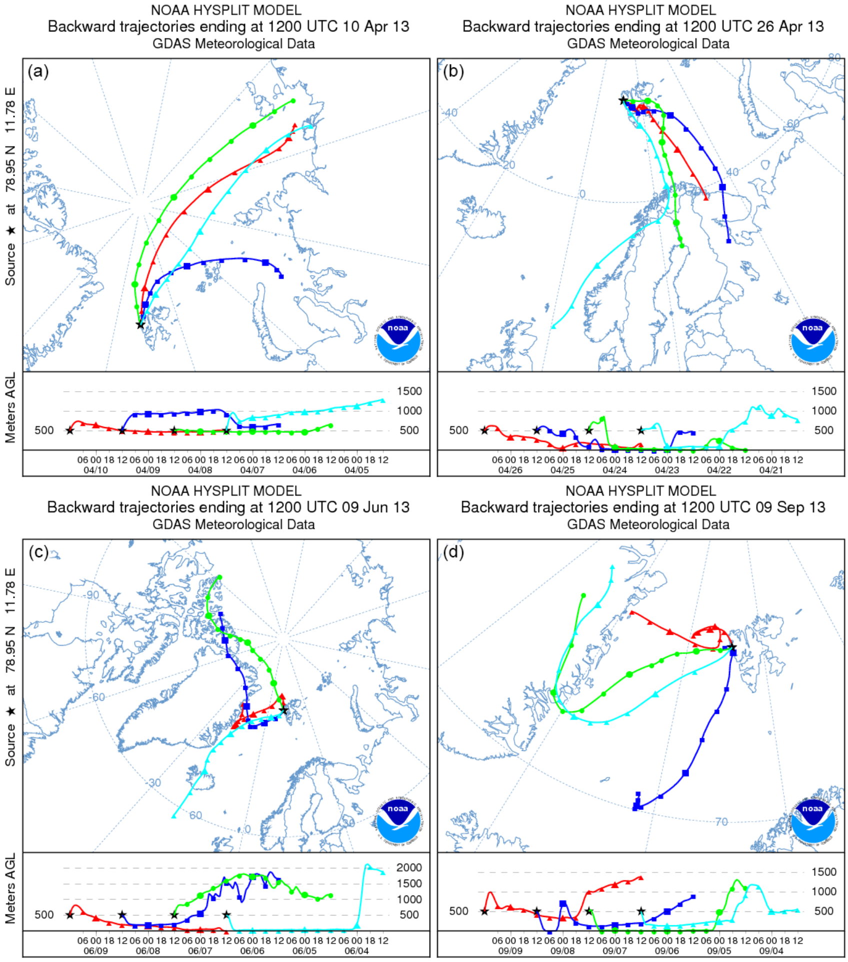

NOAA HYSPLIT MODEL
Backward trajectories ending at 1200 UTC 10 Apr 13
GDAS Meteorological Data

NOAA HYSPLIT MODEL
Backward trajectories ending at 1200 UTC 26 Apr 13
GDAS Meteorological Data

NOAA HYSPLIT MODEL
Backward trajectories ending at 1200 UTC 09 Jun 13
GDAS Meteorological Data

NOAA HYSPLIT MODEL
Backward trajectories ending at 1200 UTC 09 Sep 13
GDAS Meteorological Data

Figure 3.9 – Backtrajectories (72 h) during events of *a* low and *b*–*d* high values of sea salt aerosol.

reaches a contribution as high as 46 % of the anion content. In particular, sulfate accounts for 19 % (5.6 nEq m^{-3}), 23 % (7.3 nEq m^{-3}) and 16 % (4.1 nEq m^{-3}) of the total ion content (anions plus cations) in all-period, spring and summer samples, respectively. All-period and seasonal ionic balances show that anions and cations are almost balanced, indicating a quite completely neutralized aerosol. Figure 3.11 shows the anions and cations sums (as nEq m^{-3}) for all the collected samples. Besides experimental errors (cumulative uncertainties evaluated around 10 %), anions and cations are also balanced day by day, with very few exceptions, when a significant free acidity is evident. This evidence means that acidic species, such as H_2SO_4 and HNO_3, were almost neutralized by ammonia, to give ammonium salts, in the atmosphere during the transport from the source areas to the deposition site.

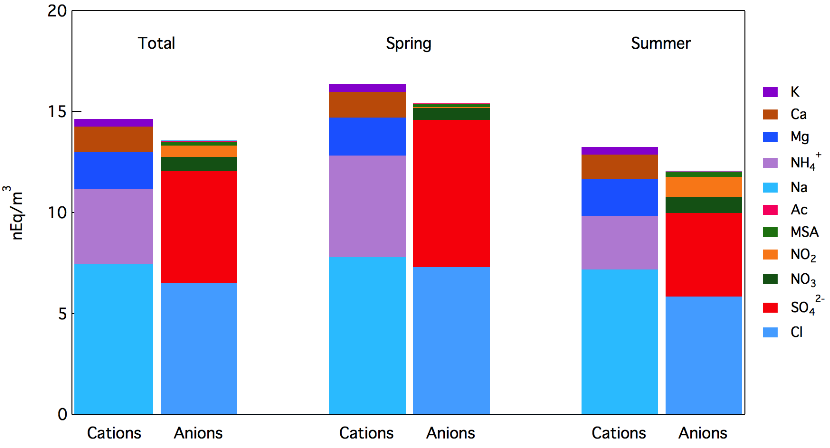

Figure 3.10 – Ionic balances (in nEq m^{-3}) for all-period (total) and seasonal aerosol samples collected at Ny Ålesund during the 2014 campaign.

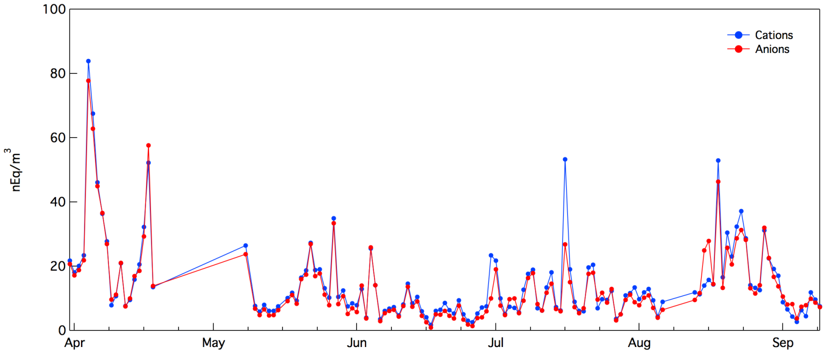

Figure 3.11 – Ny Ålesund PM_{10} anions (red dot) and cations (blue triangle) budget ($nEq\,m^{-3}$) along the sampling period of 2013.

3.2.5 Sulfuric contribution

The second most important contribution to the ionic load of PM_{10} is represented by sulfate (26.5 %). The ss-sulfate and the crustal sulfate (cr-$SO_4{}^{2-}$) are a minor contribution to sulfate budget. Therefore, their contribution has to be subtracted from the total sulfate content. By using ss-Na^+ as sea spray marker and nss-Ca^{2+} as crustal indicator ($SO_4{}^{2-}/Ca^{2+}$ w/w ratio in the uppermost Earth crust is 0.59, Wagenbach et al., 1996), the ss-$SO_4{}^{2-}$ and cr-$SO_4{}^{2-}$ fractions were calculated, following the previous equations, and their values were removed from the tot-$SO_4{}^{2-}$ concentration, then obtaining the nss-ncr-$SO_4{}^{2-}$ fraction. The nss-ncr-sulfate fraction is dominant and can be mainly ascribed to anthropogenic sources via the atmospheric oxidation of SO_2. Indeed, the temporal profile of nss-$SO_4{}^{2-}$ shows a clear seasonal trend, with maximum values in spring, when Arctic Haze events are more frequent and intense, both in the PM_{10} bulk samples and, especially, in the sub-micrometric fraction (fig. 3.12a). In this fraction, sulfate is the most abundant ionic species (65.3 %), followed by ammonium (10.5 %). Indeed, ammonium and oxalate show the same temporal profile of nss-sulfate, with high values in spring and very low summer concentrations. The very similar temporal pattern of ammonium and nss-sulfate highlights the neutralization processes between sulfuric acid and ammonia in the atmosphere.

Ammonia neutralization

By plotting nss-ncr-${SO_4}^{2-}$ vs. ${NH_4}^+$ concentrations, it was possible to evaluate if NH_3 is a relevant neutralizing agent for H_2SO_4 and to estimate the neutralization level. Figure 3.13 shows that nss-ncr-${SO_4}^{2-}$ and ${NH_4}^+$ concentrations are significantly correlated (linear regression; $R = 0.94$, $n = 136$), so demonstrating that sulfate is present in the Ny Ålesund aerosol as an ammonium salt. The slope of the linear regression (3.59) represents an intermediate value between the ${SO_4}^{2-}/{NH_4}^+$ ratios of 2.66 (corresponding to the w/w ratio in $(NH_4)_2SO_4$ salt) and 5.33 (${SO_4}^{2-}/{NH_4}^+$ w/w ratio in NH_4HSO_4). Therefore, the sulfate is present in both these species in spring-summer Ny Ålesund aerosol. Figures 3.12c for 2013 and 3.14 for 2014 show the temporal trend of the nss-ncr-${SO_4}^{2-}/{NH_4}^+$ w/w ratio along all the sampling period. It is evident that nss-ncr-${SO_4}^{2-}$ is simultaneously present both as completely ($(NH_4)_2SO_4$) or partially (NH_4HSO_4) neutralized form in the majority of samples, with a significant exception for a short transport event occurred on 15–16 August 2014. In these days, the nss-ncr-${SO_4}^{2-}/{NH_4}^+$ w/w ratio reaches values as high as 6.31, indicating the presence of sulfate in acidic form (H_2SO_4).

3.2.6 Chloride depletion

In the sub-micrometric fraction, the Cl^-/ss-Na^+ ratio was always lower than the value (1.81 w/w) measured in the seawater

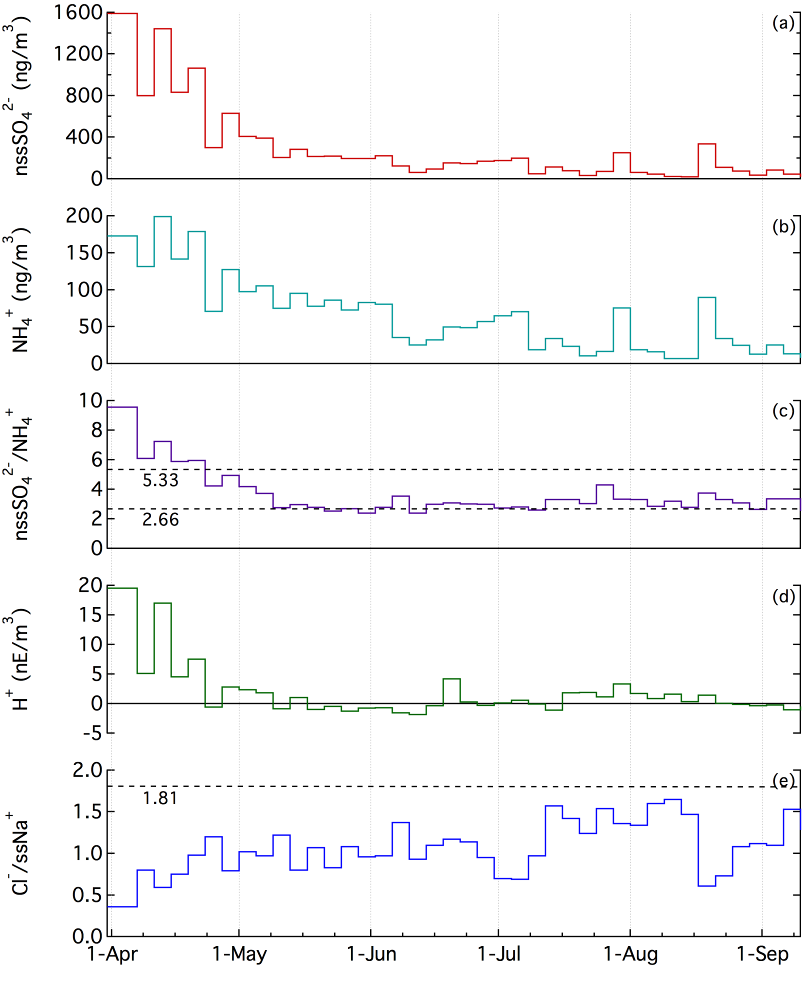

Figure 3.12 – Temporal profiles of: nss-$SO_4{}^{2-}$ (*a*), $NH_4{}^+$ (*b*), nss-$SO_4{}^{2-}/NH_4{}^+$ ratio (*c*), H^+ (*d*), and Cl^-/ss-Na^+ ratio (*e*) in the sub-micrometric aerosol fraction relative to 2013.

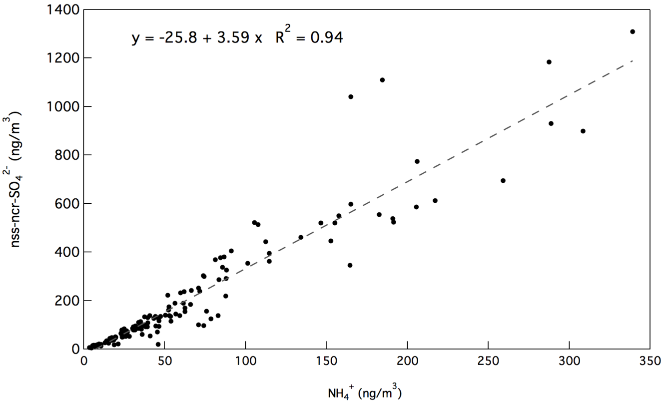

Figure 3.13 – Linear relationship between nss-nc-$SO_4{}^{2-}$ and $NH_4{}^{+}$ concentrations in 2014 Ny Ålesund aerosol samples.

(fig. 3.12e). This chloride depletion can be attrib-uted to acid-base exchanges between NaCl and acidic species, such as nitric and sulfuric acids, to give sulfate and nitrate salts and gaseous HCl. This reaction, occurring on the sea salt particle surface, is more effective for small particles, with a large surface/volume ratio. Indeed, the mean Cl^-/ss-Na^+ ratio in the sub-micrometric fraction was 1.07, values significantly lower than those measured in the three super-micrometric stages (from 1.39 to 1.50). Besides, the chloride depletion is expected to be larger in spring, when the atmospheric concentration of H_2SO_4 in the Arctic haze is higher. Figure 3.12e, relative to 2013, shows that the Cl^-/ ss-Na^+ ratio was lower when nss-$SO_4{}^{2-}$ was higher (spring). In the late spring-summer period, Cl^-/ss-Na^+ increases, because the sulfate concentrations are lower and, especially, the dominant sulfate species is $(NH_4)_2SO_4$ and not H_2SO_4, so enlightening a lack of free acidity. The exchange reaction between NaCl and acidic species occurs in the atmosphere during the aerosol transport from the ocean to the sampling site, and its effect

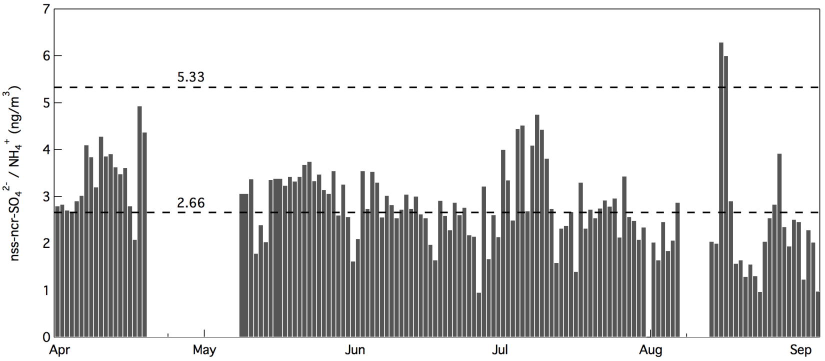

Figure 3.14 – Temporal trend in 2014 of nss-ncr-SO_4^{2-}/NH_4^+ (w/w) ratio. 2.66 and 5.33 are the SO_4^{2-}/NH_4^+ ratios in $(NH_4)_2SO_4$ and NH_4HSO_4 respectively.

increases with the residence time of sea spray. In this way, the extent of the chloride depletion is an indicator of the presence of acidic species in the atmosphere, as well as the presence of aged aerosol, i.e., aerosol formed in regions far from the sampling site and subject to long-range transport processes. To highlight the relevance of the free acidity, 2 days of 2013 were selected as examples of low and high chloride depletion. Figure 3.15a shows the 72-h back-trajectory plot for the August 12th PM_{10} sample, where the chloride depletion was little (Cl^-/ss-Na^+ = 1.65). Back-trajectories at three altitudes show that air masses reaching Ny Ålesund were coming from North Pole areas, very likely free from anthropogenic contaminants in summer. Indeed, the sub-micrometric record of nss-SO_4^{2-} shows very low concentrations in this period (fig. 3.12a). Besides, nss-SO_4^{2-} is mainly present in neutralized ammonium salts (fig. 3.12e). On the contrary, on April 1st, during the spring depletion event, back-trajectories show northward winds delivering air masses from northern Russia (fig. 3.15b), likely to deliver sulfate and other acidic species able to cause depletion processes. On this day, the sulfate concentration was quite high (2420 ng m^{-3}).

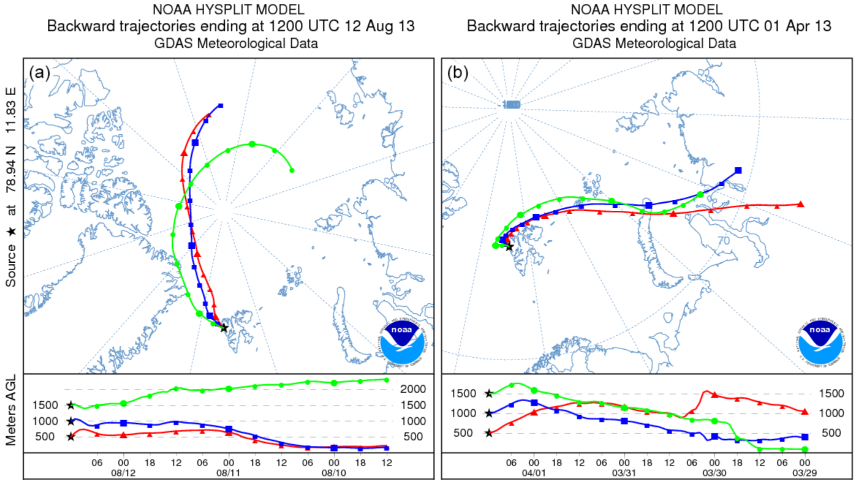

Figure 3.15 – Comparison between backtrajectories (72 h) in days of *a* no chloride depletion and *b* high chloride depletion.

3.2.7 Biogenic emission

The nss-ncr-SO$_4$$^{2-}$ fraction can be attributed to the sum of the species originated in acidic form. The main sources of H_2SO_4 are the anthropogenic emissions and the marine biogenic activity. While source markers of anthropogenic emissions are difficult to interpret because of the large variety of emissions, the contribution of the phytoplanktonic metabolic processes can be evaluated by using MSA as their univocal marker. Therefore, the anthropogenic impact on the sulfate budget was evaluated by subtracting the biogenic sulfate (bio-SO$_4$$^{2-}$) fraction from the nss-ncr-SO$_4$$^{2-}$ concentrations.

Phytoplanktonic metabolic processes produce dimethylsulfoniopropionate (DMSP) as an osmolyte. DMSP is broken down by marine microbial species to form two major volatile sulfur compounds: methanethiol (CH_3SH) and dimethylsulfide (DMS, $CH_3{-}S{-}CH_3$). While methanethiol is rapidly assimilated by bacteria into sulfur-proteins, bacteria uptake of DMS is slower and this compound, scarcely soluble in seawater, is emitted into the atmosphere, where it is oxidized to methanesulfonic acid (MSA) and H_2SO_4 (Bates, Calhoun, and Quinn, 1992; Saltzman, 1995; Kettle and Andreae, 2000). On the global scale, the MSA and H_2SO_4 aerosol originated from marine biogenic emissions affects the Earth's radiative budget by the direct and indirect way (Gondwe et al., 2003). For these effects, the marine biogenic emissions are believed to play a relevant negative feedback on climate change (CLAW hypothesis, Charlson et al., 1987). A strong relationship between aerosol MSA and marine primary productivity was found by Becagli et al., (2013), in the Southern Mediterranean Sea. Besides, nss-${SO_4}^{2-}$ from marine biogenic emissions was used by Wolff et al., (2006), as a specific marker to reconstruct marine biogenic activity for the last 800 kyr by ice core analysis.

While ${SO_4}^{2-}$ at present in the Arctic has many sources and is originated mainly from anthropogenic emission, MSA is a univocal marker of the biogenic emissions. Therefore, the bio-${SO_4}^{2-}$ fraction can be evaluated if the ${SO_4}^{2-}$/MSA ratio from DMS oxidation is known. Unfortunately, this ratio is highly variable and it depends on latitude, air temperature and photochemistry efficiency (e.g., Bates, Calhoun, and Quinn, 1992; Barone, Turnipseed, and Ravishankara, 1995; Hynes, Wine, and Semmes, 1986; Leck and Hetinzenberg, 2002; Turnipseed, Barone, and Ravishankara, 1996).

To understand the relationship between MSA and ${SO_4}^{2-}$ from biogenic emission, we plotted the nss-ncr-${SO_4}^{2-}$/MSA w/w ratio vs. MSA concentration measured in the PM_{10} samples, aiming to find a limit ratio when MSA (i.e. biogenic contribution) is high. Figure

3.16 shows that the nss-ncr-$SO_4{}^{2-}$/MSA ratio tends to be 3.0. This value is similar to other values measured in Polar Regions during summer campaigns. Teinilä et al., (2003) found nss-$SO_4{}^{2-}$/MSA ratios ranging from 77 to 3.8 at ground level in Ny Ålesund. In the same site, by using multistage impactor data, Teinilä et al., (2004) calculated a value around 5 in the sub-micrometric fraction. In the central Arctic Ocean, Chang et al., (2011) found a value of 4, while Leck and Persson, (1996) calculated a ratio = 4.5 in the sub-micrometric aerosol fraction. Values closer to that we have observed as biogenic limiting value were reported at Alert (Canada) by Norman et al., (1999) (nss-$SO_4{}^{2-}$/MSA = 2.6) and by Li and Barrie, (1993) (nss-$SO_4{}^{2-}$/MSA = 1.7). In East Antarctic Plateau (Concordia Station), by using the same approach, Udisti et al., (2012) found the value of 2.6 for a multi-year aerosol database. The ratio = 3.0 evaluated in the 2014 GVB data set is very close to that obtained by the AOE-96 box-model (mean nss-$SO_4{}^{2-}$/MSA = 3.1, by Karl et al., 2007), and slightly higher than those calculated by a chemical transport model (1.5 - 2.6 by Gondwe et al., 2006). By using the $SO_4{}^{2-}$/MSA ratio = 3 in biogenic aerosol originated in the Arctic sea areas, the bio-$SO_4{}^{2-}$ fraction can be evaluated by multiplying the MSA concentrations, measured in the Ny Ålesund aerosol samples, by this value.

Regarding the size distribution, as observed for nss-$SO_4{}^{2-}$, MSA was mainly distributed in the sub-micrometric fraction (tab. 3.4; fig. 3.17), suggesting that the preferred oxidation path is the photochemical oxidation occurring in the gas phase, followed by gas to particle conversion. An oxidation in heterogeneous phase on sea salt particles would have led to higher concentrations in the super-micrometric stages, where the sea spray particle is mainly present, as observed in early summer in Antarctica (Becagli et al., 2012).

The temporal trend of MSA in the sub-micrometric stage (fig.

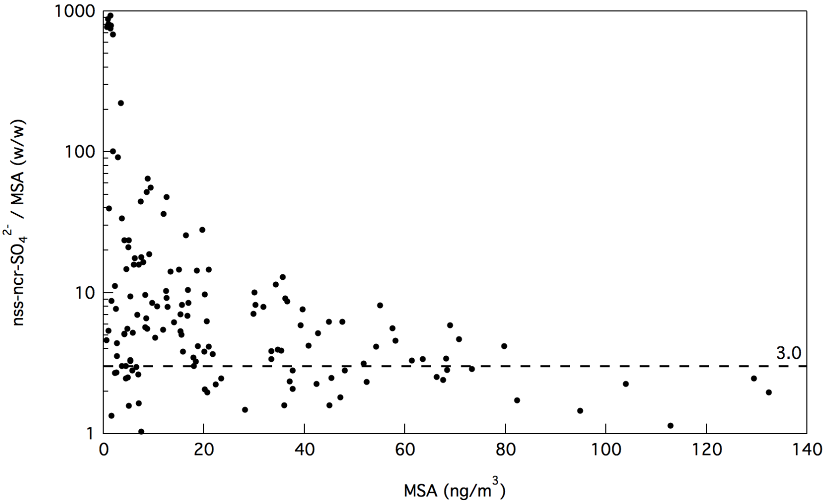

Figure 3.16 – Relationship between the nss-nc-SO_4^{2-}/MSA w/w ratio and MSA concentration in all-period 2013 Ny Ålesund aerosol samples.

3.17) shows the highest concentrations from the end of April to early June, with maxima in mid-May, when values as high as 80 ng m^{-3} were occasionally measured. Such summer maximum simultaneously occurs with the peak of sea ice melting and can be related to the biogenic productivity at the marginal ice zone in the surrounding oceanic areas.

3.2.8 Sulfate anthropogenic fraction

Following the above discussion, the anthropogenic contribution to the sulfate budged (anthr-SO_4^{2-}) in every aerosol sample is evaluated by subtracting the sum of the ss-SO_4^{2-}, cr-SO_4^{2-}, and bio-SO_4^{2-} fractions from the tot-SO_4^{2-} concentration.

Table 3.5 and figure 3.18 show the percentage and mean values of the contribution of the four sulfate fractions to the sulfate budget in all period and in spring and summer samples. In all-period

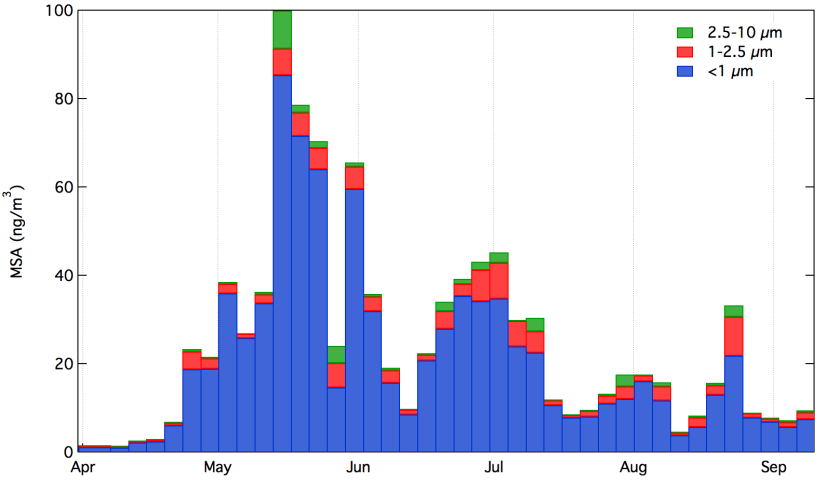

Figure 3.17 – Temporal trend of MSA in the three size stages under 10 µm: 10 - 2.5 µm, 2.5 - 1 µm, < 1 µm, during 2013.

samples, ss-, cr-, bio-, and anthr-$SO_4{}^{2-}$ fractions account for 15.2, 4.2, 21.2, and 61.2 % respectively of the total sulfate budget. It is evident that the anthropogenic emissions play a dominant role in the sulfate atmospheric concentration at Ny Ålesund, with a minor but significant contribution from sea spray and biogenic sources. On the contrary, the crustal contribution is quite low.

Table 3.5 – Sulfate source apportionment (ng m^{-3}) for the Ny Ålesund summer-spring PM_{10} samples of 2014.

Sulfate fraction	*All period*	*Spring*	*Summer*
Anthropogenic	163.7	262.4	83.4
Biogenic	56.4	40.3	69.5
Sea salt	40.6	42.2	39.3
Crustal	11.2	11.6	10.8

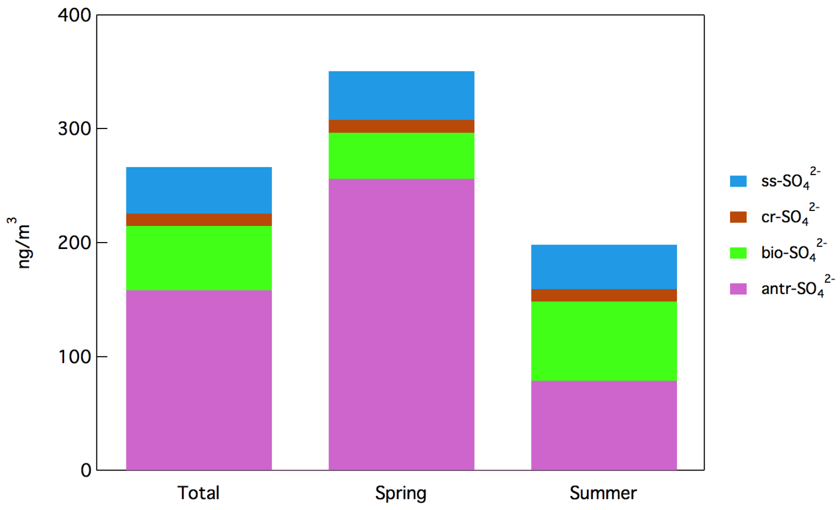

Figure 3.18 – All-period and seasonal contribution of sea salt, crustal, biogenic and anthropogenic fractions to the sulphate budget in 2014 Ny Ålesund aerosol.

More interesting information can be retrieved by the seasonal pattern. In the spring samples, the anthropogenic contribution is very high (covering the 74.8 % of the sulfur budget), so demonstrating the effect of Arctic haze transport events, which are more probable and intense in this season (Quinn et al., 2007). This is due to the inefficient pollutants dispersal, slow removal rates and isentropic transport into the Arctic as low-pressure systems run-up against quasi-stationary Siberian high (Barrie, 1986). In summer, the impact of the anthropogenic source is lower (42 %), with a contribution comparable to that coming from biogenic emissions (35 %), which reaches absolute and percentage values about two times higher than those measured in spring. The sea salt contribution is quite constant (as absolute concentration) in the two seasons, but the percentage contribution is significantly higher in summer (19.8 %) than in spring

(12.0 %). The crustal source plays a minor role. The all-period contribution is 4.2 % of the sulfate budget. Likewise ss-$SO_4{}^{2-}$, the absolute concentrations of cr-$SO_4{}^{2-}$ are similar in spring and summer, but summer percentage is higher (5.5 %, with respect to 3.3 % in spring), due to the larger sulfate atmospheric concentrations in spring. Figure 3.19 shows the temporal distribution of the four sulfate fractions along all the sampling period of 2014.

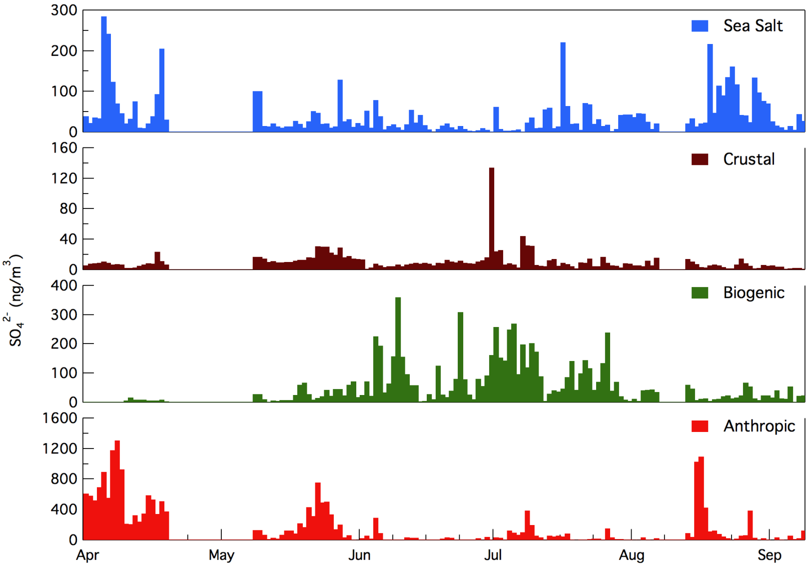

Figure 3.19 – Temporal trend of the contribution of sea salt, crustal, biogenic and anthropogenic fractions to the sulphate budget in 2014 Ny Ålesund aerosol.

A dominant anthropogenic contribution is visible in the aerosol samples from 31 March to end of May, during the period 3-10 June and during a sharp event on 15-16 August. Scheuer et al., (2003) showed that, as the spring season progresses, surface haze diminishes and sulfate starts to decline. In summer, sulfate aerosol is efficiently removed from the atmosphere by low-level clouds and wet deposition processes (Scheuer et al., 2003). Sea spray sulfate is especially large in sporadic spring events and, consistently, in the period 17-31 August. The biogenic sources are relevant from early June to the end of July. The sulfate crustal fraction is visible (but scarcely relevant) in the period 19-25 May and in sporadic samples in late June-early July (especially in the 30 June sample). The higher summer values are possibly due to the contribution of local dust after the snow coverage melting.

3.3 Trace metals

3.3.1 Sample handling

Because of the low concentration of the metals in the Arctic samples, a particular attention was given to every step of sample preparation and during the analysis and a high level of certified purity was required for all the solutions used. All the acid solutions used for dilution and cleaning were prepared from concentrated sub boiled (s.b.) HNO_3, obtained by the DST-1000 acid purification system (Savillex, Minnesota, USA), from 65 % nitric acid for analysis (Carlo Erba, Italy). Suprapur grade 30 % H_2O_2 (Merck, Germany) was used to complete the digestion. The preparation of the diluted HNO_3 (1 %) and all the cleaning procedures, were accomplished using MilliQ ultrapure water (18 MΩ cm), obtained by Millipore purification system. Every plastic or metal tool and the polyethylene bottles were previously washed with MilliQ water in an ultrasonic bath.

Before the digestion, from each filter, the PMP (polymethylpentene) frame ring was removed, to avoid metal contaminations, in particular for Al, Zn, and Cu. Each filter was then mineralized with a microwave digestion system, according to UNI EN 14902:2005 standard method for Pb, Cd, As, and Ni analysis. Thus, the mineralization occurred in a microwave oven (Mars Xpress, CEM, Italy), where each filter was added to 2 mL of concentrated HNO_3 s.b. and 0.5 mL of H_2O_2, in clean Teflon-PFA vessels. The digestion program was arranged in three phases: (i) 70 % of 1600 W for 20 minutes, to increase temperature and pressure up to 220 °C and 30 atm; (ii) stable temperature and pressure for 25 minutes; (iii) cooling down to room temperature. The microwave digestion is a effective method that allows to quickly solubilize the metals present in the particulate matter (except for the silicates), using a very low volume of reagents and with an accurate control of temperature and pressure. The final solution of each sample used for the analysis, included about 10 mL of 1 % HNO_3 in MilliQ water, coming from 2 - 3 consecutive rinses of each vessel. The exact volumes of sample dilution (as well as those of the calibration standards) were determined gravimetrically. After each mineralization cycle, the vessels were cleaned with HNO_3 s.b. with the above-mentioned microwave digestion program.

Finally, exactly 5 mL of each sample were transferred to pre-cleaned polyethylene tubes, where the internal standard was added just before the analysis. Samples and calibration standards signals are normalized to the signal of Indium, used as internal standard, with the final concentration of 10 ppb. For the calibration curves was utilized a 100 mg L^{-1} customized solution of REE standard (O2si, South Carolina, USA) and a 1000 mg L^{-1} single standard solution (Merck) for the other elements. The solution used for every preliminary operation before the analysis (tuning, mass calibration and daily performance), is a Carlo Erba multielement standard solution, containing Ba, B, Co, Fe, Ga, In, K, Li, Lu, Na, Rh, Sc, Tl, U, and Y at the concentration of 1000 mg L^{-1} (1 % HCl, 5 % HNO_3), diluted to 1 µg L^{-1}. These elements cover the whole mass spectrum analyzed, without any mutual interference.

3.3.2 Instrumentation

All the analytical measurements presented in this work were carried out with an ELEMENT2 (Thermo Fisher Scientific, Massachusetts, USA), a double focusing magnetic sector field Inductively Coupled Plasma Mass Spectrometer (ICP-SFMS), equipped with a reverse Nier-Johnson geometry and coupled with a desolvation system provided with a microflow nebulizer. The instrument can work in the 5 - 260 amu mass range, with three resolution levels ($m \ \Delta m^{-1}$), nominally: 300 (LR), 4000 (MR) and 10 000 (HR); however high resolution was not used for this work. Thermo Element's auto lock mass software routine was used during the analysis to compensate for mass drift, caused by thermal effects. All the operative settings of the instrument were daily checked and optimized and are shown in table 3.6.

Table 3.6 – ICP-SFMS Finnigan ELEMENT2 and APEX tune configuration.

Argon flow rates	
Cool	16.0 L min^{-1}
Auxiliary	1.0 L min^{-1}
Sample	0.850 L min^{-1}
RF power	1200 W
Extraction lens voltage	−1270 V
Sample uptake rate	100 µL min^{-1}
Sample cone	1.1 mm, Nickel
Skimmer cone	0.8 mm, Nickel
Take up time	60 s
Washing time	90 s
Resolutions ($m\,\Delta m^{-1}$, 10 % valley)	LR: 300; MR: 4000; HR: 10000
Introduction system	APEX HF, self-aspirated microflow nebulizer
Intr. system temperatures	100 / −5 °C
Additional gas and flow rate	N_2; (10 ± 5) mL min^{-1}
Oxides ($^{238}U^{16}O^+/^{238}U^+$)	<1.5 %
Double charged ion ($^{137}Ba^{++}/^{137}Ba^+$)	0.22 %
Tuning and mass calibration	Daily performed

One of the most important interferences in the ICP-SFMS measurements is the oxides formation in the plasma, due to the presence of water in the sample solutions; furthermore, also the extremely low concentration of metals in the samples made it necessary to avoid the oxides formation. Thus, the APEX HF desolvating system (ESI, Nebraska, USA) was used in order to minimize the presence of water within the sample gas flow, thanks to a thermal treatment, consisting of a heating and a subsequent cooling. The sample solution was self-aspirated via a PFA microflow nebulizer from an ASX-510 (Teledyne CETAC, Nebraska, USA) autosampler, with a sample flow rate of 100 µL min^{-1} into a heated cyclonic spray chamber to vaporize the entire sample (100 °C). The excess solvent within the aerosol is then condensed out by a Peltier cooled condenser (−5 °C) with nitrogen as additional gas, added through this port to increase signal intensity and stability, and reduce the formation of oxide interferences. Thus the dry aerosol reached the ICP torch and was noticed that the use of a desolvation system led to several benefits in the ICP-MS analyzer, if compared with a spray chamber introduction system (tab. 3.7): (a) it produces a more intense and reproducible signal, due to the presence of 90 % of the analyte within the aerosol and to the smaller and more homogeneous dimensions of the aerosol droplets, that means an increase of 5 times of the analytical sensitivity (^{115}In was the reference); (b) it concentrates the analyte and lower the volume of sample solutions needed for analysis, from 6 mL to around 0.5 mL; (c) the amount of oxides and hydrides in the aerosol is lowered 10 times, leading to a considerable reduction of the isobaric interferences. Moreover, the isobaric interferences produced by double ionizations were already sufficiently low (<0.25 %). This allows avoiding the application of mathematical corrections suggested by the instrument software for the interference suppression. The ratio between $^{238}U^{16}O^{+}$ and $^{238}U^{+}$ was used as the reference to quantify the oxides in the aerosol and its mean value was never higher than 1.5 %, adequate for the required accuracy. Instead, the ratio $^{137}Ba^{++}/^{137}Ba^{+}$ was used to check the double ionization. These ratios were daily checked before the analysis. Moreover, during the analysis, all of the samples and calibration standards were kept under a laminar flow hood, to minimize any kind of contamination.

Table 3.7 – Performances comparison between Spray chamber and APEX.

	Spray chamber	*APEX*
Sample volume	6 mL	0.5 mL
Signal intensity (cps ^{115}In, LR)	5×10^5	2.5×10^6
Oxides ($^{238}U^{16}O^+/^{238}U^+$)	14 %	1.5 %
Double charged ion ($^{137}Ba^{++}/^{137}Ba^+$)	0.25 %	0.22 %

Method performances

The ICP-SFMS system was set for the determination of 32 metals (34 isotopes), using low and medium resolution, and Indium as internal standard (tab. 3.8). Thanks to the 100 µL min^{-1} microflow aspiration, the sample consumption during the 7.5 minutes of a single run is low enough to allow the use of just 5 mL of sample, which is sufficient to have a concentrated sample and a volume of solution easy to handle.

Although being the main source of isobaric interferences, oxides are not the only ones, so that a selection of the isotopes of the elements to be determined was necessary. Indeed, interferences can also derive from double ionizations or molecular adducts with other elements, thus their intensities depend on the concentration of those elements. So, every isotope was chosen on the basis of the best compromise between abundance and specific interferences.

The purpose of having a high and stable signal drives to the use of low resolution as much as possible but, thanks to the advantage of having an instrument with three resolution modes, many interferences can be solved with the medium or going even to the high resolution, lowering the signal of 90 % for every resolution increase. The use of a higher resolution is not possible for the quantification of REEs because of their already weak signal, but it is instead possible for

Table 3.8 – Method settings of the ICP-MS.

	Low resolution	*Medium resolution*
Mass window	150 %	125 %
Sample time	0.01 s	0.01 s
Sample per peak	20	30
Segment duration	0.30 s	0.38 s
Search window	150 %	50 %
Integration window	80 %	60 %
Scan type	EScan	EScan
Detection mode	Counting and Analog	Counting and Analog
Integration type	Integral	Integral
Internal standard	^{115}In	^{115}In
Selected isotopes	^{27}Al, ^{45}Sc, ^{89}Y, ^{111}Cd, ^{138}Ba, ^{139}La, ^{140}Ce, ^{141}Pr, ^{146}Nd, ^{147}Sm, ^{153}Eu, ^{157}Gd, ^{159}Tb, ^{163}Dy, ^{165}Ho, ^{166}Er, ^{169}Tm, ^{172}Yb, ^{175}Lu, ^{206}Pb, ^{208}Pb	^{23}Na, ^{27}Al, ^{45}Sc, ^{47}Ti, ^{51}V, ^{52}Cr, ^{55}Mn, ^{56}Fe, ^{60}Ni, ^{63}Cu, ^{66}Zn, ^{68}Zn, ^{75}As, ^{89}Y, ^{98}Mo

many other more abundant metals, as reported in table 3.8. In this method, there was no need to use neither the high resolution nor any mathematical correction, which may introduce additional uncertainties.

Limits of detection and blanks

The limits of detection (LOD) in solution for each measured element shown in table 3.9 are evaluated as 3 times the standard deviation of 10 analyzed blank solutions (HNO_3 1 %); for the limits of detection for atmospheric concentration, a mean air volume of 54.7 m^3 was considered. Very good LOD were found, especially for Rare Earth Elements, from 38 $fg\,m^{-3}$ for Lanthanum, down to 9 $fg\,m^{-3}$ for Ytterbium.

Table 3.9 – Analytical performances for each isotope.

Isotope	*Res.*	*RSD*	*LOD*		*Blank %*	
		%	ppt	pg m^{-3}	ppt	pg m^{-3}
^{23}Na	M	1.6	310	125	7298	2935
^{27}Al	L	1.6	117	47	3129	1259
^{27}Al	M	2.0	158	64	2908	1169
^{45}Sc	M	10.4	0.136	0.054	0.795	0.32
^{47}Ti	M	11.4	21	8.5	150	60
^{51}V	M	6.0	0.597	0.24	19.2	7.73
^{52}Cr	M	2.8	1.67	0.67	157	63.3
^{55}Mn	M	2.9	1.76	0.71	55.1	22.2
^{56}Fe	M	2.2	44	18	3824	1538
^{60}Ni	M	2.3	6.03	2.42	150	60.3
^{63}Cu	M	4.4	4.45	1.79	75.6	30.4
^{66}Zn	M	1.7	121	49	14 015	5637
^{68}Zn	M	2.2	148	59	13 590	5466
^{75}As	M	3.6	10.2	4.09	10.1	4.05
^{89}Y	L	1.9	0.110	0.044	2.74	1.10
^{89}Y	M	2.7	0.141	0.057	2.48	1.00
^{98}Mo	M	11.0	0.488	0.20	7.62	3.07
^{111}Cd	L	7.9	0.886	0.36	8.70	3.50
^{138}Ba	L	2.0	7.05	2.84	75.0	30.2
^{139}La	L	2.4	0.094	0.038	4.66	1.88
^{140}Ce	L	1.4	0.086	0.035	6.39	2.57
^{141}Pr	L	3.0	0.059	0.024	1.11	0.45
^{146}Nd	L	2.2	0.079	0.032	2.45	0.99
^{147}Sm	L	2.1	0.038	0.015	0.855	0.34
^{153}Eu	L	3.0	0.047	0.019	0.683	0.27
^{157}Gd	L	3.3	0.067	0.027	1.080	0.43
^{159}Tb	L	1.7	0.024	0.010	0.473	0.19
^{163}Dy	L	2.7	0.046	0.019	0.712	0.29
^{165}Ho	L	1.7	0.023	0.009	0.508	0.20
^{166}Er	L	3.0	0.046	0.018	0.594	0.24
^{169}Tm	L	2.0	0.026	0.011	0.460	0.18
^{172}Yb	L	1.5	0.022	0.009	0.590	0.24
^{175}Lu	L	2.4	0.032	0.013	0.467	0.19
^{206}Pb	L	1.8	1.55	0.62	43.2	17.4
^{208}Pb	L	1.7	1.51	0.61	44.9	18.0

A study of blanks for each element was accomplished in order to determine the effects of the acidic digestion procedure and blank filters on the final concentrations. Procedural blanks (including digestion tubes, laboratory handling operations, and reagents) are comparable with the ones measured on the digested unexposed filters for most of the elements. Since the blanks of the reagents (ultrapure water, HNO_3 s.b., and suprapur hydrogen peroxide) are below or comparable with the detection limit for most the elements, the most relevant reason of contamination can be ascribed to the whole set up of operations carried out in the extraction protocol.

Filter impurities are significant only for Al, Cr, and Zn, but always under the sample concentration levels. Despite the very low blank values, they are not negligible because of the very low concentration of the analytes. The blank levels range from the minimum of the 1st percentile of the samples concentrations for Iron to the maximum of the 50th percentile for Cadmium. So, the mean blank value of each element was subtracted from the concentrations found in the samples.

Recovery and precision

Digestion efficiencies for the analyzed Rare Earth Elements were calculated as recoveries of a certified reference material, using AMiS 0356, REE(L) Carbonatite Wigu TZ (AMiS, Republic of South Africa). Two different aliquots of CRM (5 and 50 µg) were used for the extraction through the earlier described microwave acid digestion procedure. The apparent recoveries are always higher than 80 % (tab. 3.10) for all the reported elements, with the exception of Scandium (the only one determined with medium resolution), even though no hydrofluoric acid was used for the mineralization but only nitric acid. The very good agreement of the measured value with the certified one, shows the accuracy of the whole procedure, from the extraction to the analysis.

Table 3.10 – Recoveries of the acid digestion; (c) certified conc., (p) provisional conc., (i) indicated mean Element.

Element	*CRM* ppm			*This study* ppm	*Recovery* %
Sc	28.0	± 6.1	p	17.5	62.4
Y	35.0	± 5.1	p	28.3	80.8
La	8226	± 1111	p	7175	87.2
Ce	11 160	± 766	c	9426	84.5
Pr	894	± 172	p	810	90.6
Nd	2419	± 253	c	2007	83.0
Sm	159	± 10	c	135	84.8
Eu	29.0	± 2.2	c	27.1	93.5
Gd	58		i	63.8	110.1
Tb	4		i	4.04	101.1
Dy	12.8	± 2.9	p	11.5	89.6
Ho	1.60	± 0.31	p	1.62	101.3
Er	3.2		i	3.19	99.7
Tm	0.32		i	0.342	106.9
Yb	1.9		i	1.67	87.7
Lu	0.28		i	0.251	89.8

The repeatability of the signal for each isotope was checked as the relative standard deviation of ten repeated analyses of the same sample. The precision of the instrument is acceptable for all the target isotopes (RSD <20 %, table 3.9) and very good for most of the elements, except Scandium (10.4 %), Titanium (11.4 %) and Molybdenum (11.0 %), likely because of the low signal due to the use of medium resolution.

3.3.3 Rare Earth Elements

All the PM_{10} samples collected during the spring-summer campaigns between 2010 and 2015 in Ny Ålesund were analyzed through ICP-MS and each metal concentration in aerosol was calculated. For the following calculations and figures, only concentrations above the detection limit will be taken into account. The mean total concentration of REEs (La to Lu) in our samples was $49.4\,\mathrm{pg\,m^{-3}}$, with a large variability ($\sigma = 85.6\,\mathrm{pg\,m^{-3}}$) mainly due to few high-value spikes, with concentrations reaching $1500\,\mathrm{pg\,m^{-3}}$ during heavy aerosol events. This high variability in the total load of REEs is likely to be ascribed to the contribution of different crustal sources containing REEs, which was highlighted already in previous works (Moroni et al., 2016) and is noticeable by the different REEs profiles. The same variability was present for each lanthanoid, as shown by their mean, median and maximum value in table 3.11. Regarding the weight, lanthanides represent on average $23 \pm 47\,\mathrm{ppm}$ of the total PM_{10} load and, as shown in figure 3.20b, they have a good correlation with Sc (0.82) and Y (0.85), that are often included within REEs because of their similar properties, and with Al (0.80), Fe (0.62), and Mn (0.75), indicating a strong relationship with crustal representative elements. All the correlation coefficients shown in figure 3.20 have a significance level (p) always lower than 0.001.

Despite REEs is one of the largest group in the periodic table displaying such a great similarity between its elements, they can be divided into two subgroups with little but systematic behavior differences: light rare earth elements (LREEs): La, Ce, Pr, Nd, Sm, and Eu; and heavy rare earth elements (HREEs): Gd, Tb, Dy, Ho, Er, Tm, Yb, and Lu. Weathering processes cause soil elements fractionation, with LREEs having usually a higher concentration in Earth's upper crust because of their preferential retention on solid

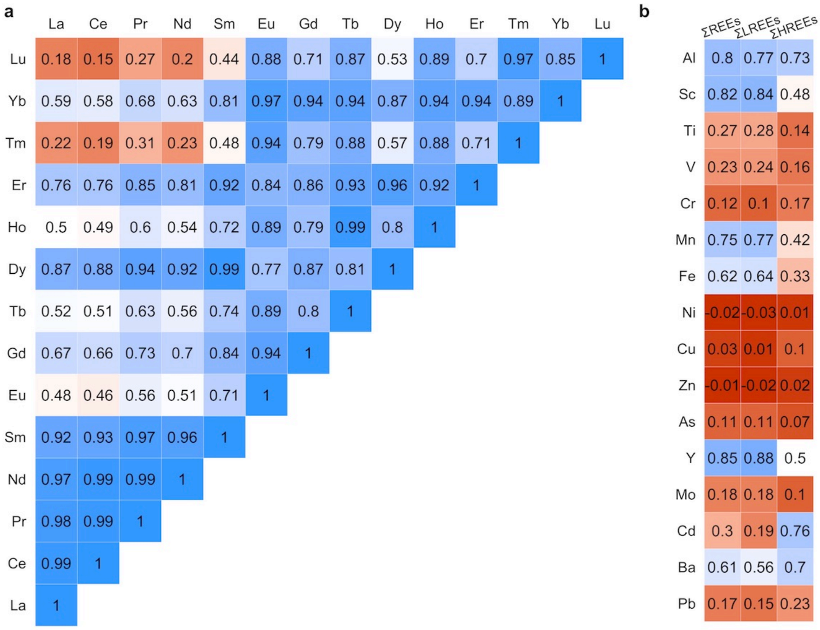

	La	Ce	Pr	Nd	Sm	Eu	Gd	Tb	Dy	Ho	Er	Tm	Yb	Lu
Lu	0.18	0.15	0.27	0.2	0.44	0.88	0.71	0.87	0.53	0.89	0.7	0.97	0.85	1
Yb	0.59	0.58	0.68	0.63	0.81	0.97	0.94	0.94	0.87	0.94	0.94	0.89	1	
Tm	0.22	0.19	0.31	0.23	0.48	0.94	0.79	0.88	0.57	0.88	0.71	1		
Er	0.76	0.76	0.85	0.81	0.92	0.84	0.86	0.93	0.96	0.92	1			
Ho	0.5	0.49	0.6	0.54	0.72	0.89	0.79	0.99	0.8	1				
Dy	0.87	0.88	0.94	0.92	0.99	0.77	0.87	0.81	1					
Tb	0.52	0.51	0.63	0.56	0.74	0.89	0.8	1						
Gd	0.67	0.66	0.73	0.7	0.84	0.94	1							
Eu	0.48	0.46	0.56	0.51	0.71	1								
Sm	0.92	0.93	0.97	0.96	1									
Nd	0.97	0.99	0.99	1										
Pr	0.98	0.99	1											
Ce	0.99	1												
La	1													

	ΣREEs	ΣLREEs	ΣHREEs
Al	0.8	0.77	0.73
Sc	0.82	0.84	0.48
Ti	0.27	0.28	0.14
V	0.23	0.24	0.16
Cr	0.12	0.1	0.17
Mn	0.75	0.77	0.42
Fe	0.62	0.64	0.33
Ni	-0.02	-0.03	0.01
Cu	0.03	0.01	0.1
Zn	-0.01	-0.02	0.02
As	0.11	0.11	0.07
Y	0.85	0.88	0.5
Mo	0.18	0.18	0.1
Cd	0.3	0.19	0.76
Ba	0.61	0.56	0.7
Pb	0.17	0.15	0.23

Figure 3.20 – Correlation matrix: (a) between Rare Earth Elements and (b) between REEs sums and the other analyzed metals (LREEs: La, Ce, Pr, Nd, Sm, and Eu; HREEs: Gd, Tb, Dy, Ho, Er, Tm, Yb, and Lu).

phases, whereas HREEs are preferentially enriched in solution thanks to their tendency to complexation (Sholkovitz, 1992; Cantrell and Byrne, 1987; Byrne and Kim, 1992). In the correlation matrix in figure 3.20b, looking at Yttrium and Scandium, the two elements included in the REEs group beside lanthanides, they show a good correlation only with light REEs. Manganese and Iron show the same behavior of Yttrium and Scandium, because of their higher interaction affinity with LREE (Koeppenkastrop, De Carlo, and Roth, 1991). Regarding the inter-REEs correlations (fig. 3.20a), the difference between light and heavy REEs is significant: a good correlation is present within each of the two groups but not between elements

Table 3.11 – Mean, median, and maximum air concentration of the Rare Earth Elements analyzed in the Arctic aerosol samples in the period 2010-2015.

Element	*Mean* pg m^{-3}	*Median* pg m^{-3}	*Max* pg m^{-3}	*N. values*
La	10.8 ± 18.6	6.1	308.3	883
Ce	19.4 ± 36.3	10.2	647.5	921
Pr	2.5 ± 4.4	1.4	74.3	914
Nd	8.5 ± 16.3	4.5	288.3	941
Sm	1.9 ± 3.4	1.1	53.8	901
Eu	0.8 ± 1.7	0.4	27.0	709
Gd	2.1 ± 4.9	1.1	85.1	814
Tb	0.6 ± 0.9	0.3	10.8	822
Dy	1.5 ± 2.5	0.8	30.7	885
Ho	0.6 ± 1.0	0.3	11.1	741
Er	1.2 ± 1.7	0.5	14.1	858
Tm	0.6 ± 1.1	0.2	15.7	718
Yb	0.8 ± 1.5	0.4	19.5	799
Lu	0.4 ± 1.5	0.2	21.0	568
ΣREEs	45.7 ± 85.3	25.1	1500.6	-
ΣLREEs	39.7 ± 76.3	20.8	1381.6	-
ΣHREEs	6.1 ± 12.1	2.8	177.0	-

belonging to different groups. Every light REE is well correlated with each other in the group ($R^2 > 0.92$), with the exception of Europium because of its anomaly (due to its additional charge +2), whereas they do not correlate well with the heavy REEs. In the HREEs group, a further partition is noticeable between odd and even-numbered elements, among which only the even ones maintain a weak similarity with LREEs. Lu does not correlate very well with other REEs, except for Tm, Ho, and Tb. This suggests that Tb, Ho, Tm and Lu within the particles are considerably variable in the atmospheric environment, also because of their very low concentration. The variability of the LREEs vs. HREEs ratio and the good correlation among the elements within the two groups is likely due to several source material profiles, coming from different geochemical weathering processes. Moreover, the internal odd-even fractionation of HREEs suggests an additional coherent behavior in atmospheric fractionation processes.

Temporal trends

The high number of daily samples allows reconstructing the temporal trend along the six-consecutive spring-summer campaigns with a daily resolution, suitable for both temporal pattern analysis and for short aerosol events investigations. In figure 3.21 the temporal evolution of the sum of the 14 lanthanoids (ΣREEs) is shown for each year and little but noticeable seasonal differences between spring and summer can be discussed. During spring the median value of ΣREEs concentration is significantly higher than in summer (respectively 28.6 $\mathrm{pg\,m^{-3}}$ and 18.2 $\mathrm{pg\,m^{-3}}$). In addition, despite the mean value of the two periods are very close, spring shows a low variability ($48.3 \pm 66.0\,\mathrm{pg\,m^{-3}}$) and rarely over 100 $\mathrm{pg\,m^{-3}}$, while in summer the combination of very low values and several heavy aerosol events increase considerably its variability ($47.6 \pm 101.2\,\mathrm{pg\,m^{-3}}$). The different medians can be explained by the higher aerosol load reaching the Arctic region and the Svalbard Islands during spring (as seen in section 3.2, mainly because of the persistence of particles in the Arctic atmosphere ascribed to the presence of the Arctic Haze (Quinn et al., 2007; Heintzenberg, Hansson, and Lannefors, 1981). On the other hand, the appearance of casual high peaks in summer (over 100 $\mathrm{pg\,m^{-3}}$) is likely attributable to the exposure of local soil, after the melting of snow, usually occurring in May.

The fractionation between light and heavy REEs, represented in

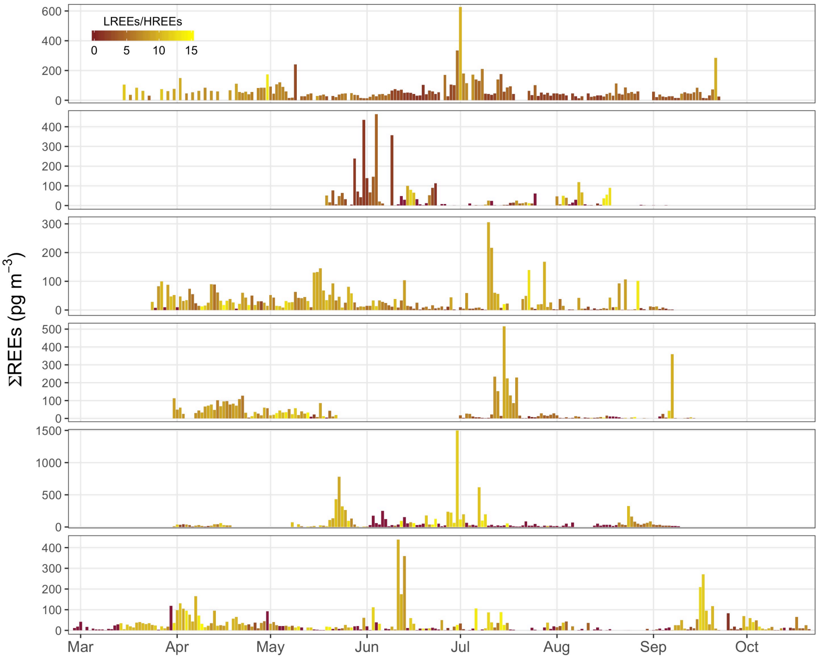

Figure 3.21 – Temporal trend of REEs air concentration sum in the six years of sampling campaign, aligned on the day of year. The color scale indicates the light-heavy REEs ratio.

figure 3.21 by their ratio, shows a seasonal pattern, characterized by high values in spring (8.37 ± 2.88) and lower values in summer (5.47 ± 3.93). This suggests a difference in the aerosol origin, ascribing to long range sources the atmospheric aerosols reaching the Arctic during spring which is depleted of heavier lanthanoids; on the contrary, the local soil, left uncovered by snow during summer, has some influence in lowering the REEs fractionation.

Cerium and Europium anomalies

The different geochemical properties in the lanthanides group have led the lighter elements to be more abundant in the Earth's crust than the heavier. In addition, every REE with an even atomic number is always more abundant than its two odd-numbered neighbor elements (Oddo-Harkins rule). These effects are present in most of the samples, as evident in the box-whisker plot in figure 3.22a, which includes all the analyzed samples and display the main concentration ranges. The removal of these systematic differences between adjacent elements allows a more efficient data interpretation and an easier comparison with sources profiles. Chondrite was chosen as the reference material because it represents the composition of the Earth's initial condition, so every difference from this reference can be ascribed to geochemical differentiation processes, such as fusion and subsequent crystallization. Thus, every REE atmospheric concentration (as ppm mass fraction) was normalized to chondrite (Boynton, 1984), bringing to the data visualization in figure 3.22b, which maintains the decreasing trend and LREEs enrichment, typical of the Earth's crust geochemical fractionation.

While all lanthanoid ions have a trivalent valence, Cerium and Europium present an additional redox state (+4 for Ce and +2 for Eu), which modifies their distribution in the environment, compared to the other REEs. These two anomalies are systematic geochemical characteristics of rock composition or redox condition of the environment and represent a further tool for their identification (Wilde, Quinby-Hunt, and Erdtmann, 1996; De Carlo, Wen, and Irving, 1998; Tostevin et al., 2016). Thus, chondrite normalization allows the evaluation of the anomalies of Cerium and Europium:

$$\frac{Ce}{Ce^*} = \frac{Ce_N}{\sqrt{La_N \cdot Pr_N}}$$

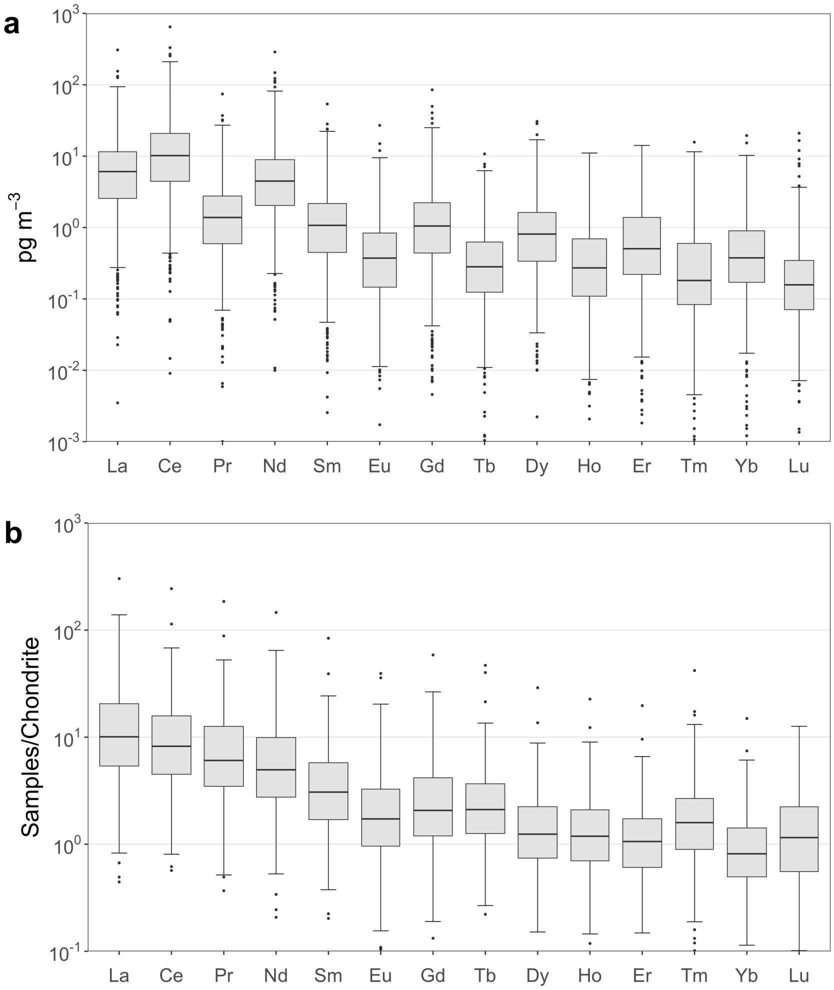

Figure 3.22 – Temporal trend of REEs air concentration sum in the six years of sampling campaign, aligned on the day of year. The color scale indicates the light-heavy REEs ratio.

$$\frac{Eu}{Eu^*} = \frac{Eu_N}{\sqrt{Sm_N \cdot Gd_N}}$$

Both the anomalies have no evident temporal pattern along the year and show a high variability. This maybe due to many influences: the median value of Cerium anomaly is 1.00 (mean $= 1.00 \pm 0.45$); whereas for Europium it is 0.86 (mean $= 1.24 \pm 0.94$). However, in both cases, looking to the monthly trend in figure 3.23, their variability increases between June and September, leading to a decrease of the median value for Cerium towards a negative anomaly from 1.02 until April to 0.94 of August-September, and to a simultaneous increase for Europium switching to a positive anomaly, from 0.68 to 1.40.

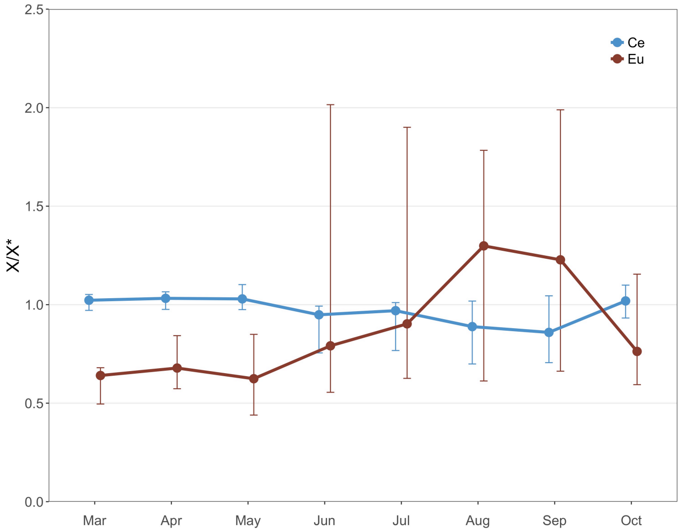

Figure 3.23 – Median, 25th and 75th percentiles of monthly Cerium and Europium anomalies.

Among the LREEs, La-Ce and Ce-Pr show very high values of correlation (fig 3.20a), as confirm of a weak Cerium anomaly presence in the REEs profiles. In contrast, Europium, with its low correlation values with the others LREEs and its variable anomaly, suggest the presence of many sources influence.

The two anomalies represent an effective tool for a first apportionment of different sources. The relationship between them is represented in figure 3.24 connected with the light-heavy ratio of normalized REEs. A large part of the samples has no Cerium anomaly, negative Europium anomaly and a high ratio of light-heavy elements; these characteristics are typical of felsic rocks and suggest their influence in many samples of atmospheric aerosols. Despite the presence of a noticeable variability in anomalies values, when a variation happens, it brings to a simultaneous decrease of Cerium anomaly and an increase for Europium. A confirmation for this differentiation comes from the light-heavy REEs ratio which follows the same change. Its trend moves towards lower values, suggesting the ascription of these samples to a local influence.

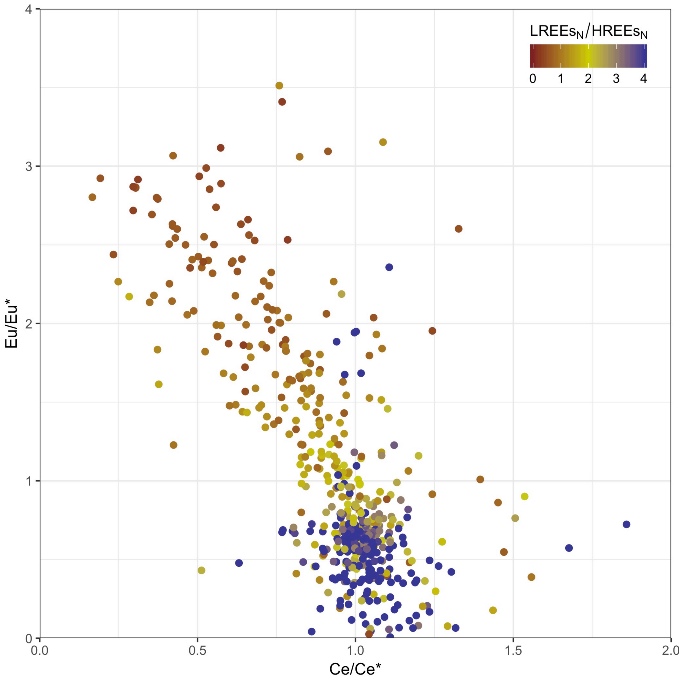

Figure 3.24 – Cerium vs. Europium anomaly distribution and their relation with light-heavy REEs ratio.

3.4 Source apportionment

Thanks to the PMF model and the back-trajectory analysis, it was possible to identify the main sources of the Arctic atmospheric aerosols. During the model optimization, many solutions with a different number of factors and using several combinations of chemical species were examined and, in the end, it yielded a solution with seven independent factors with 28 chemical species (including the total PM_{10}). The model was run 20 times and all the runs converged.

The validity of this result is supported by an in-depth analysis of the residuals for each species, aimed at minimizing their value. Residuals are the difference between the real value (observed) in each sample and the sum of the source contributions calculated by the model (predicted). The residues are low as the model is able to divide the mass of the chemical species into the factors found, without any unexplained mass rest. To explain the validity of our results, figures 3.25a and 3.26 show the correlation and the time series of observed and predicted PM_{10} concentrations respectively.

Besides, the distribution of scaled residuals ($r_{ij} = e_{ij}/\sigma_{ij}$) of PM_{10}, represented in figure 3.25b, is largely within the range of -3 and $+3$, which also confirmed a good agreement between the observed and predicted values. PM_{10} is shown here as the representative of the goodness of the result, since it was used in the model as the total variable for the mass closure. In addition to PM_{10}, the residuals analysis was performed for all the species and, as shown in figure 3.27, most of the scaled residuals fall within the ± 3 range, with a few exceptions, however not far from that range.

The PMF model apportioned 85.9 % of the total measured PM_{10} mass to the seven sources, namely: ammonia-sulfate, anthropic, biogenic, biomass burning, marine, nitrate, and soil, as shown in figure 3.28, together with their mean relative percentage in the 2015

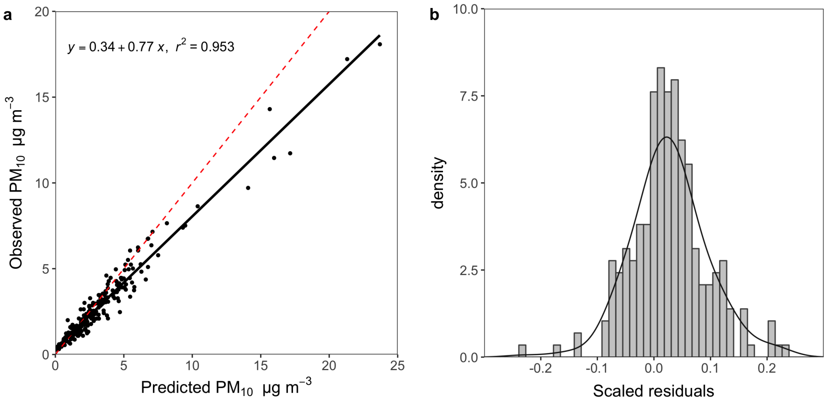

Figure 3.25 – *a*: correlation with linear regression between observed PM_{10} concentration of the samples and their predicted values by PMF model. *b*: distribution of the scaled residuals for PM_{10}.

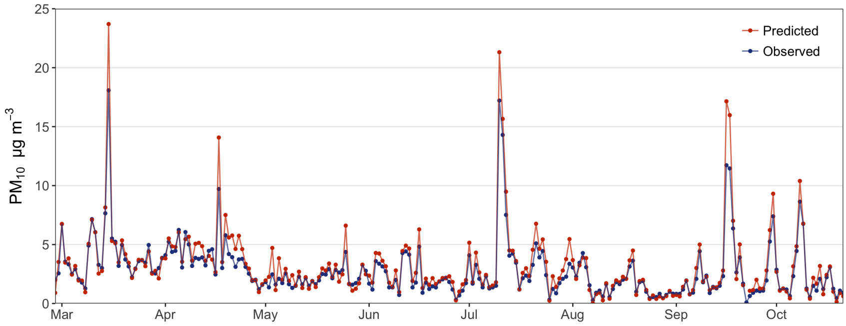

Figure 3.26 – Time series of observed and predicted concentrations of PM_{10}. The residuals are the difference between the two values in each sample.

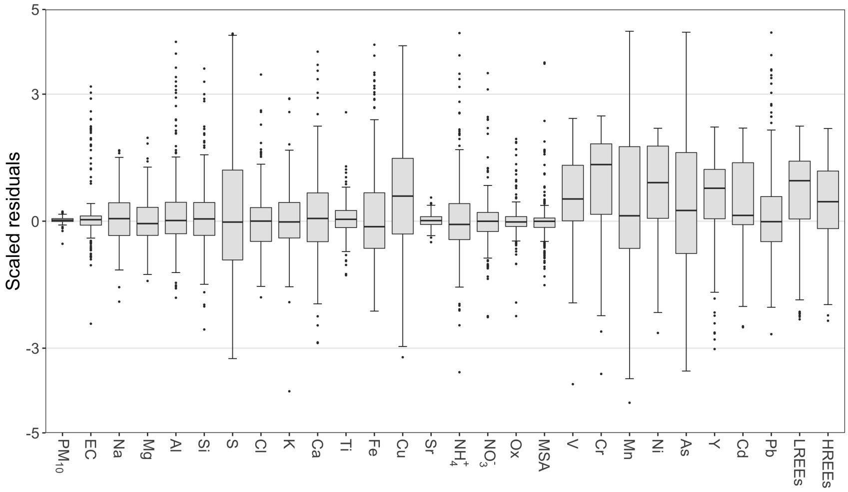

Figure 3.27 – Box-whisker plot of the scaled residual distributions of every chemical species used in the PMF model.

campaign samples. The identified factors represent both natural and anthropic sources, which account for the 57.7 % and 27.6 % of the total apportioned PM_{10} mass respectively, whereas the biomass burning source (14.7 %) can have both origins.

The final result provided the weight amount corresponding to every factor in the whole dataset of samples. Figure 3.29 shows the time series amount of the factor contributions as a percentage of the total particles in the samples. The figure gives a general picture of the temporal trend of the sources and their relative weight on the aerosol load (which are discussed separately in detail in the next section).

As just seen for each sample, in figure 3.30 are shown the relative contributions of the factors in each of the 28 chemical variables used in the model. The plot confirms how many sources influenced the presence of a single chemical species. Their different relative

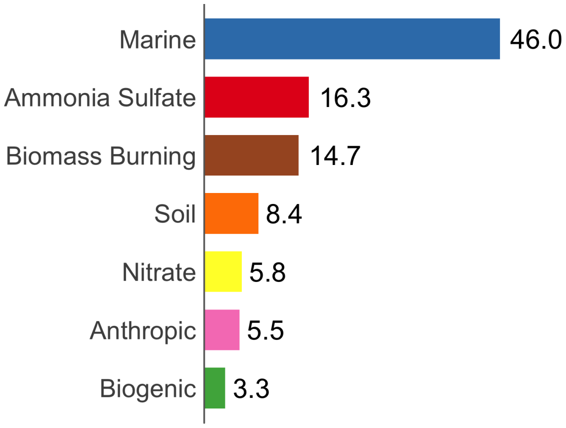

Figure 3.28 – Mass fraction (as percentage) of the seven factors identified by PMF analysis in the apportioned PM_{10}.

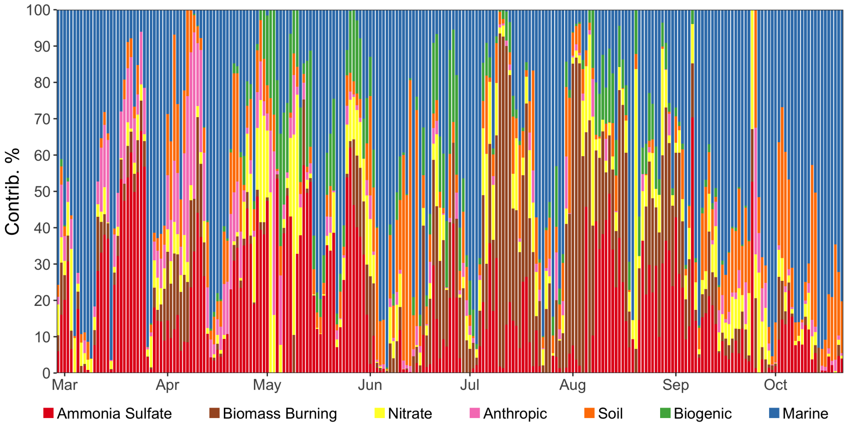

Figure 3.29 – Time series of the percentages of the factor contributions in each sample.

distribution, together with the corresponding air concentration, is a very useful information about the chemical composition of the factors. Thus, thanks to the chemical composition, to the distinctive species (the source's chemical markers) and to the mass fraction of the main chemical components (tab. 3.12), it was possible to link each factor to the corresponding source. Moreover, the ratios between species concentrations within the same factor represent a fingerprint of the source, which can be then recognized both in future model analyses and within single samples.

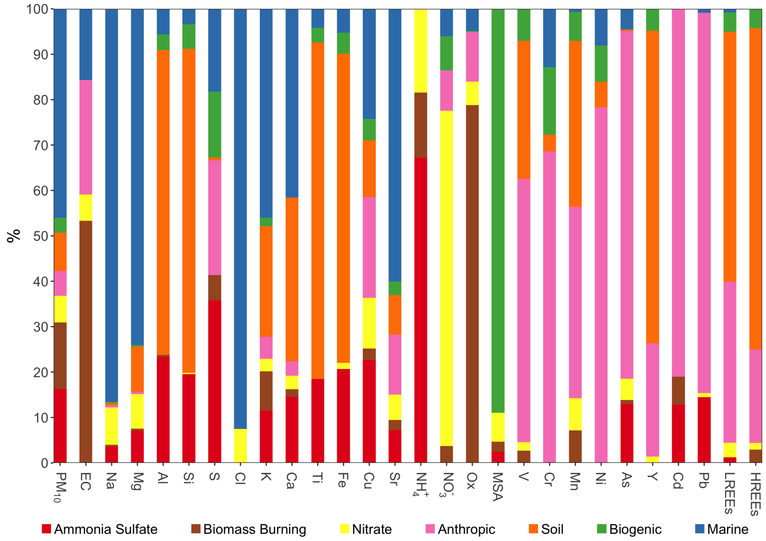

Figure 3.30 – Percentage distribution of the seven factors within the 28 chemical species used in the PMF analysis.

The daily atmospheric concentration of each one of the seven factors obtained by PMF (fig. 3.29), together with the 900 trajectories of 2015 (4 per day), calculated with the NOAA HYSPLIT model, were the input used to run the PSCF model. The combination of the PSCF model together with PMF results has proved to be a powerful

Table 3.12 – Chemical composition, as mass percentage, of the seven factors obtained by PMF analysis. Only chemical species above 1 % are shown.

Factor	*Species (%)*
Ammonia Sulfate	S (44.7 %), NH_4^+ (23.5 %), Na (9.0 %), Si (7.7 %), Al (4.6 %), Mg (2.8 %), Fe (2.5 %), Ca (2.5 %), K (2.3 %)
Anthropic	S (82.2 %), NO_3^- (5.5 %), Na (3.2 %), EC (2.7 %), K (2.6 %), Ca (1.4 %), Ox (1.3 %)
Biogenic	S (55.2 %), MSA (25.3 %), Si (6.5 %), NO_3^- (5.4 %), Al (2.0 %), Na (2.0 %), Fe (1.7 %), K (1.1 %)
Biomass Burning	S (31.6 %), NH_4^+ (22.6 %), Ox (15.9 %), EC (9.8 %), K (7.9 %), Na (4.7 %), NO_3^- (4.0 %), Ca (1.3 %)
Marine	Cl (53.4 %), Na (34.9 %), Mg (4.6 %), S (3.6 %), K (1.5 %), Ca (1.1 %)
Nitrate	Cl (35.1 %), Na (27.0 %), NO_3^- (22.6 %), NH_4^+ (8.3 %), Mg (3.8 %)
Soil	Si (41.8 %), Al (19.4 %), Fe (12.3 %), Ca (9.3 %), K (7.2 %), Mg (5.7 %), Na (1.8 %), S (1.3 %), Ti (1.1 %)

tool for the identification of regions of potential aerosol influence (Pekney et al., 2006; Polissar, Hopke, and Poirot, 2001). The PSCF results are displayed in the form of maps of the geophysical region covered by the trajectories and divided into cells of 1°×1° latitude and longitude, on which the PSCF probability values are displayed in terms of a color scale ranging from 0 to the maximum probability value of each plot. Finally, the PSCF values are smoothed on the map area to make more readable the result and the source region assignment.

3.4.1 Marine

The sea salt contribution is the most important contribution in the Arctic PM_{10} (46 %), as already seen in section 3.2.4. The 99.1 % of the composition of the marine factor is represented by the sum of the six main markers of the sea salt: Cl^-, Na^+, Mg^{2+}, S, K^+, and Ca^{2+} (fig. 3.31d). Regarding the Sulfur, it is present in this source as sulfate (${SO_4}^{2-}$) and for this reason, and from now on, the sulfate contribution is calculated as three times the sulfur (proportionally to their masses). The importance of these species as chemical markers of the marine source is explained by their percentage contribution (red diamonds in fig. 3.31a) over 40 % for all the six species and the Strontium, for which the sea salt represents one of the main sources in the atmosphere, since it is present in the seawater as trace element. The ratios between the PMF fraction of Potassium, Magnesium, Calcium, and Chloride with Sodium are close to the same ratios present in the sea water (Henderson and Henderson, 2009), as shown in table 3.13, whereas sulfate shows the highest discrepancy.

Table 3.13 – Comparison between the ratios of the main ions of sea water with Sodium and the same ratios obtained in the PMF results.

	K^+	Mg^{2+}	Ca^{2+}	Cl^-	${SO_4}^{2-}$
$\left(\frac{X}{Na^+}\right)_{sea}$	0.036	0.129	0.038	1.81	0.253
$\left(\frac{X}{Na^+}\right)_{PMF}$	0.042	0.131	0.033	1.53	0.312
Δ	+16 %	+1.5 %	−13 %	−15 %	+23 %

The contribution of this natural source to the atmospheric PM_{10} does not have a glaring seasonal trend (fig. 3.31b). Its presence is mainly linked to the action of the wind on the sea surface and high concentration spikes are due to strong wind events, which are more frequent during spring and autumn.

The PSCF result confirms the assignment of this factor to a marine origin. The most influent area is the Norwegian Sea, whereas minor contributions come from the Barents Sea and the Greenland Sea (fig. 3.31c). Since the influential areas are seas around the Svalbard Islands, the result suggests a nearly exclusive local source, which is explained by the short residence time in the atmosphere of these particles. This is supported by the size of the particles (more than 75 % are over 1 µm, as seen in section 3.2.3) making them more subject to scavenging processes. Moreover, we can not exclude a strictly local influence due to the aerosol formed in the sea sections around Ny Ålesund and which is excluded from the back-trajectory analysis because of its likely path below the planetary boundary layer.

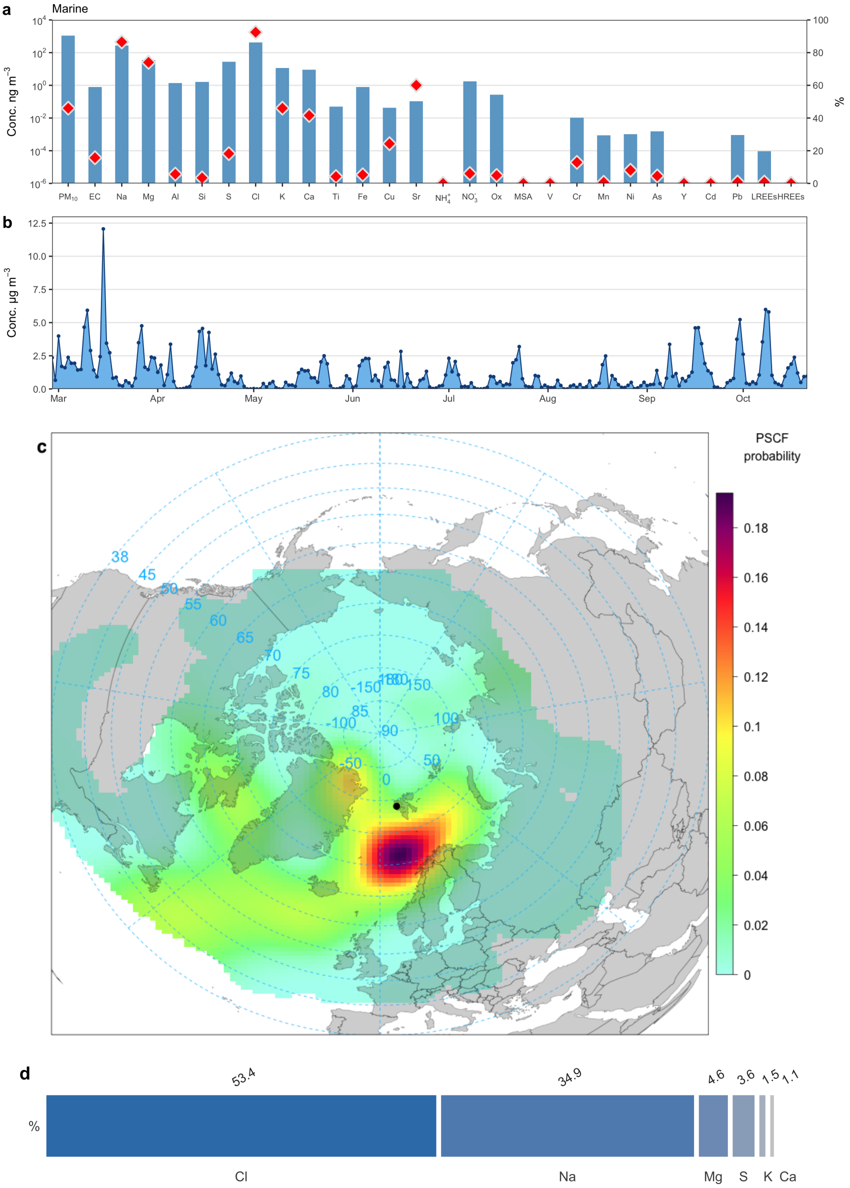

Figure 3.31 – Factor 1: Marine. *a*: factor profile as species mass contribution (blue bars) and percent distribution of elements within the factor (red diamonds); *b*: time series of the factor contribution; *c*: PSCF probability distribution of the factor over the Arctic; *d*: mass percentage of the species (>1 %) within the factor.

3.4.2 Soil

The second natural source found by the PMF model represents the soil contribution to the Arctic aerosol, which is estimated as 8.4 % of the total PM_{10}. Despite this little mass fraction within the whole PM_{10} load, it contains a high apportioned mass of Al, Si, Ti, Fe, Y, and HREEs (> 60 %) and a minor contribution of K, Ca, V, Mn, and LREEs (> 20 %) (fig. 3.34a). Since these elements are the main components of the upper continental crust, their nearly exclusive presence allows identifying this factor as the crustal influence. Moreover, the distribution of these elements within the soil factor (their percentage in the apportioned PM_{10}), is similar to their distribution in the continental crust (Henderson and Henderson, 2009), as shown in figure 3.32, confirming the consistency of the source attribution.

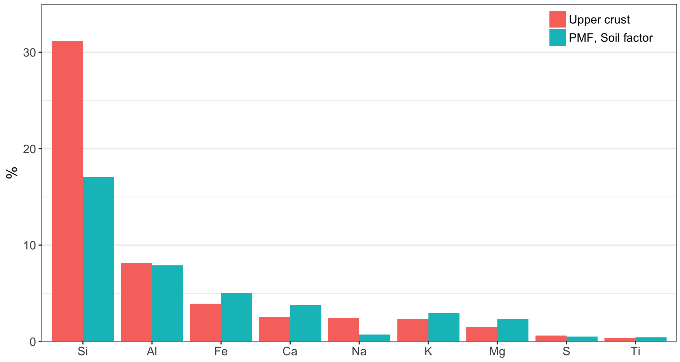

Figure 3.32 – Comparison between the main elements fraction of the upper continental crust (Henderson and Henderson, 2009) and their percentage in the the Soil factor, in order of crustal abundance.

As with the marine source, for the soil is not present any seasonal pattern (fig. 3.34b). Just a few strong aerosol events are recognizable and can be useful for the identification of precise source areas. In this case, the high crustal event occurred between 11 and 13 June was analyzed separately. While the PSCF model points both at the Russian archipelago of Novaya Zemlya and at the southern Scandinavian Peninsula, looking to the superimposed back-trajectories in figure 3.33 the greater influence of the Russian archipelago is clear, because of the larger number of trajectories coming from that region.

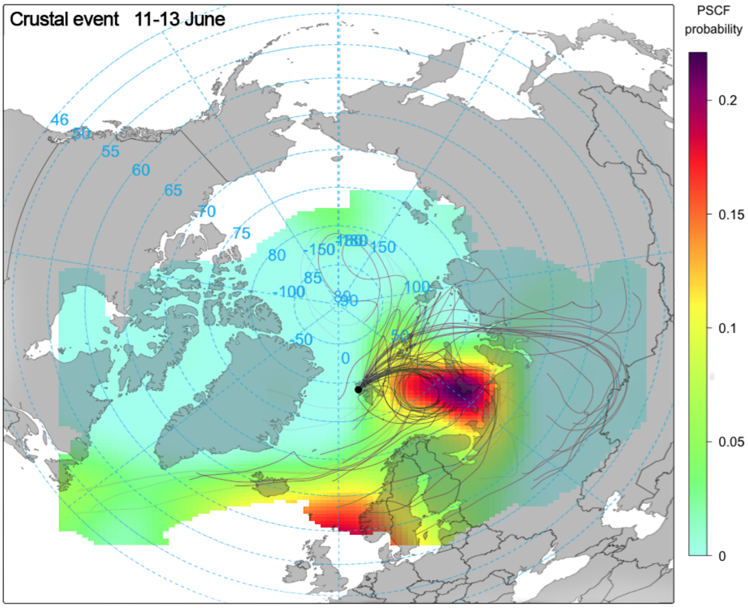

Figure 3.33 – PSCF model and backward trajectory superimposition during the crustal event between 11 and 13 June 2015.

Looking to the total PSCF analysis of the factor (fig. 3.34c), we can recognize two main crustal sources: a nearby influence, from all the dry land facing towards the Svalbard Islands (i.e. Northern Scandinavia, Greenland and the Russian archipelagos); and a long range source, from central Russia. However, as for the marine source, the hypothesis of a local source cannot be ruled out.

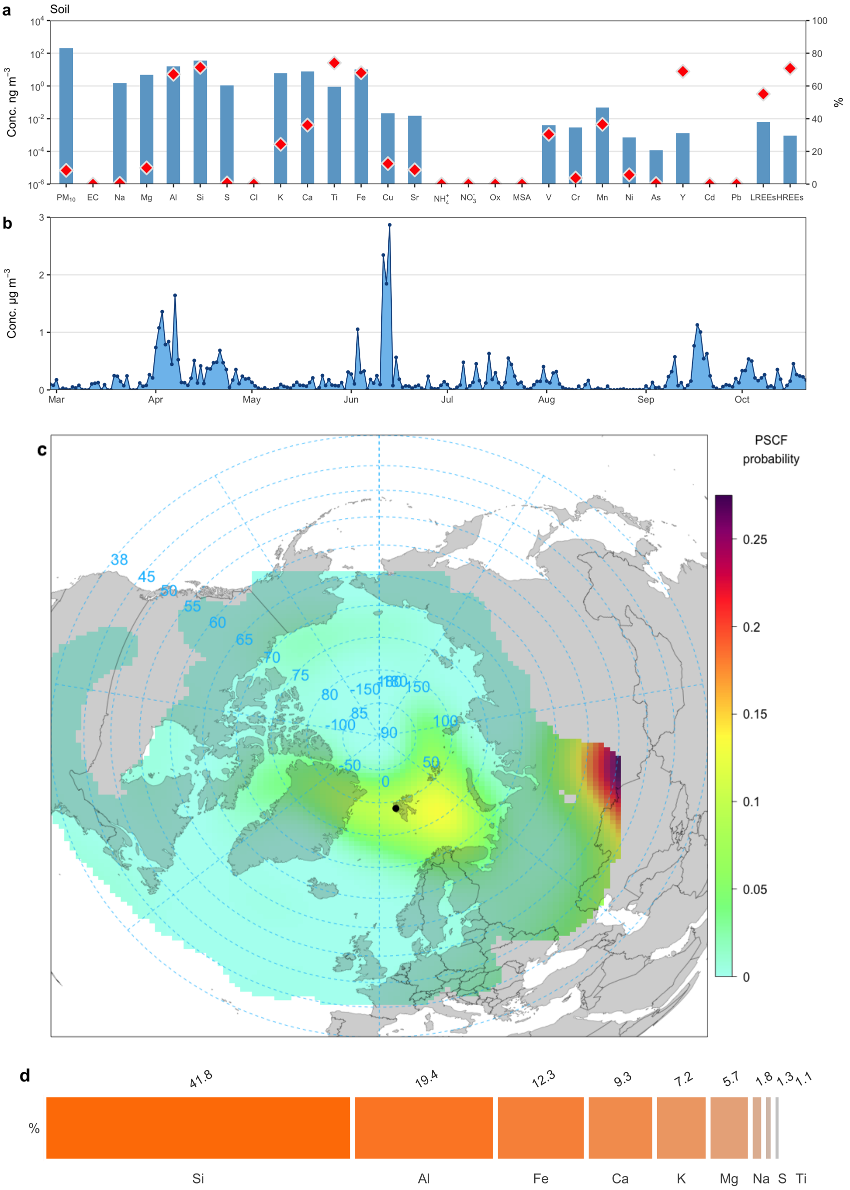

Figure 3.34 – Factor 2: Soil. *a*: factor profile as species mass contribution (blue bars) and percent distribution of elements within the factor (red diamonds); *b*: time series of the factor contribution; *c*: PSCF probability distribution of the factor over the Arctic; *d*: mass percentage of the species (>1 %) within the factor.

3.4.3 Anthropic

Despite V, Cr, Ni, As, Cd, and Pb represent only the 0.4 % of the mass of this factor and are not among its main components (fig. 3.37d), they are the chemical species on which is based the naming of this source. Indeed, these heavy metals are chemical markers of industrial activities, such as petroleum refining, chemical industry, minerals and coal mining and, as shown in figure 3.37a, most of their mass is gathered in this factor, which accounts for 5.5 % of the PM_{10}. Since 84 % of Lead is apportioned to this source, it is representative of this factor as clear from the comparison between its time series (fig. 3.35) and the equivalent of the Anthropic factor in figure 3.37b.

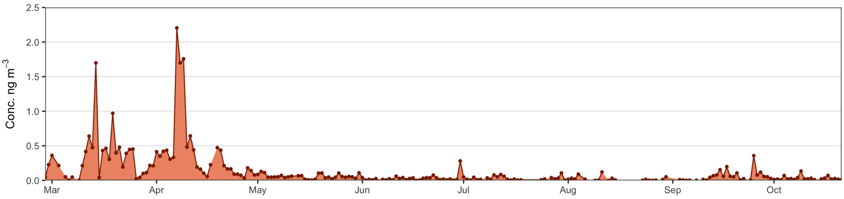

Figure 3.35 – Time series of the total air concentration of ^{206}Pb during 2015.

From the time series of the factor, it is evident a seasonal pattern, which is mainly ascribable to the influence of the Arctic haze (see section 3.2.8), with most of the mass contribution concentrated between March and April (83 %) and very low values for the rest of the period.

The main source regions for the PM_{10} apportioned to this factor are the east coast of North America and the geographical region between the North Greenland and western Russia (fig. 3.37c). This last wide extension on the sea and beyond the Arctic polar circle of a primary anthropic factor is explained by the long permanence of the anthropic pollutant which is typical of the Arctic haze. This, together with the 5-day limit of the back-trajectories, leads the PSCF model to point at the regions of a longer lasting permanence of the particles as the source regions.

The strong spring contribution deserved an in-depth analysis about the origin of the air masses. Looking to the PSCF model limited to the March-April period for Pb and Cd, two of the main markers (fig. 3.36a-b), is clear the influence of two different regions of the western Russia: the geographical areas near St. Petersburg and Surgut, which are both the locations of headquarters of extensive industrial activity (fig. 3.36c; Urbanica, 2012).

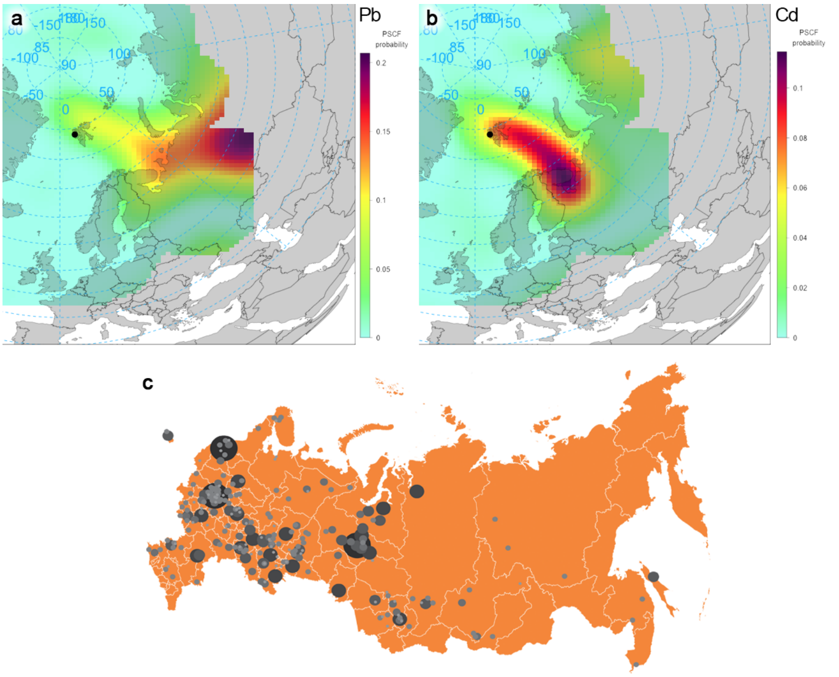

Figure 3.36 – PSCF results limited to the March-April period for Lead (*a*) and Cadmium (*b*); *c*: main industrial activities in Russia, classified by size (source: urbanica.spb.ru).

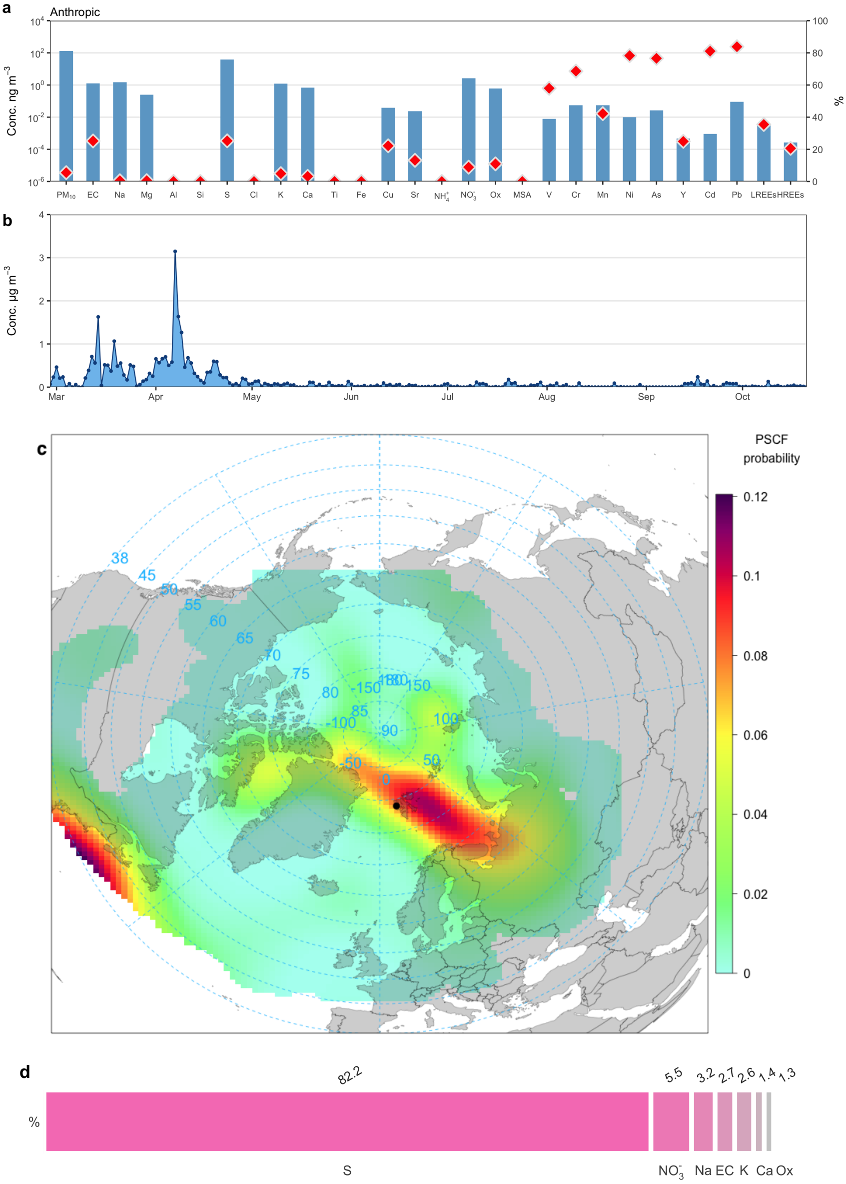

Figure 3.37 – Factor 3: Anthropic. *a*: factor profile as species mass contribution (blue bars) and percent distribution of elements within the factor (red diamonds); *b*: time series of the factor contribution; *c*: PSCF probability distribution of the factor over the Arctic; *d*: mass percentage of the species (>1 %) within the factor.

3.4.4 Ammonia-sulfate

This is the second PMF factor in order of abundance (16.3 %) and it was so named because Sulfur (i.e. sulfate) and ammonium are both the most abundant species in mass, and those with the highest apportioned percentage in this factor (respectively 44.7 % and 23.5 %).

This factor is quite similar to the previous one in both seasonal trend and source region but deeply different in its chemical composition. Indeed, after the two main species, the rest of the mass is mostly formed by crustal metals (fig. 3.38d). Even though in its profile heavy metals are either absent or present in negligible concentrations (fig. 3.38a), its origin can be partially ascribed to anthropic activities thanks also to the similarities with the anthropic factor. The temporal trend with high concentrations in spring and lower during summertime (fig. 3.38b) suggests an influence of the Arctic haze for this factor as well, as seen for 2013 in section 3.12. In this case, however, it is a secondary aerosol factor and, even assuming a common source with the anthropic factor, it is impossible to trace back to the source region. Gaseous SO_2 emitted at lower latitudes and transported to the Arctic persists in the atmosphere longer than solid particles and its conversion to H_2SO_4 and the subsequent ammonium neutralization could occur anywhere along its path towards the north. This makes the 5-day back-trajectories useless and, as result, the factor seems to have a local source (fig. 3.38c), without any influence from Europe and Russia.

Unlike the anthropic factor, here the presence of non-negligible concentrations during summer is partially due to the formation of biogenic sulfates in the atmosphere (as seen in section 3.2.7) from the photochemical oxidation of DMS and MSA in gas phase followed by gas-to-particle conversion.

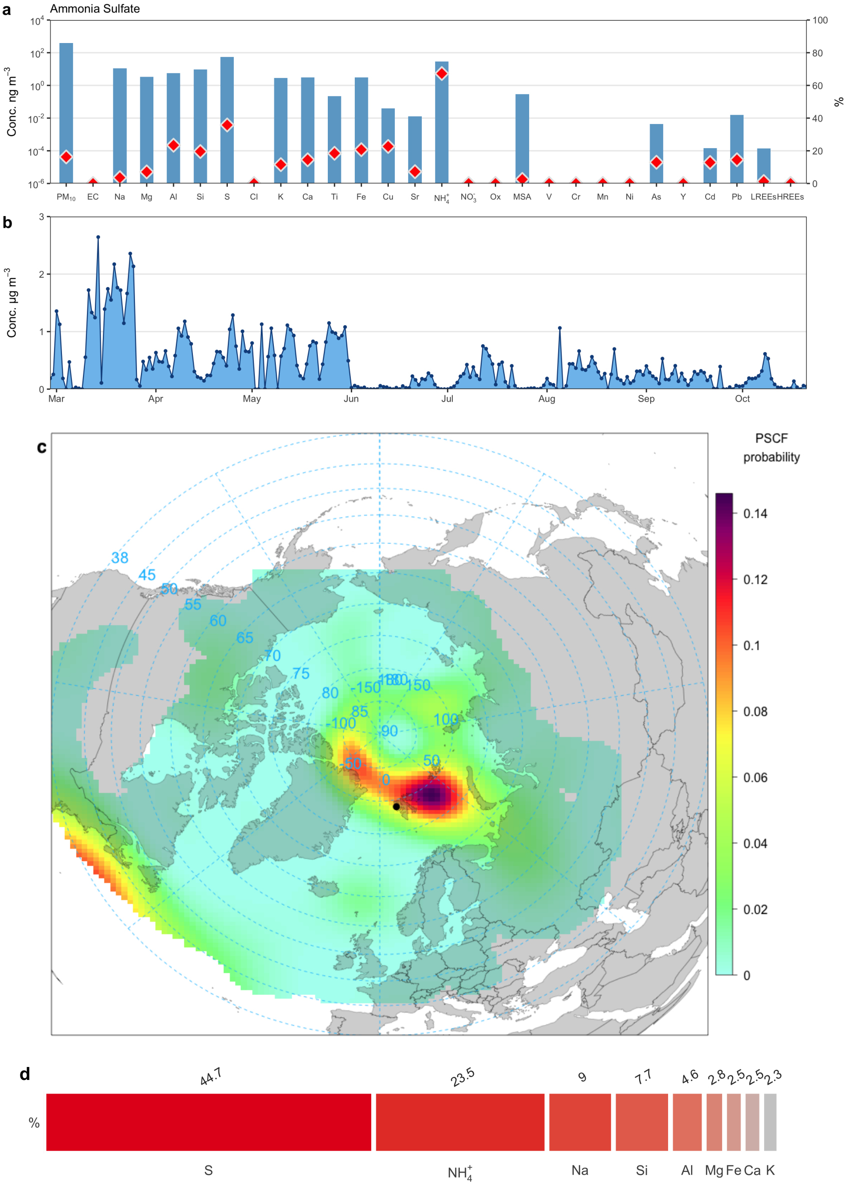

Figure 3.38 – Factor 4: Ammonia Sulfate. *a*: factor profile as species mass contribution (blue bars) and percent distribution of elements within the factor (red diamonds); *b*: time series of the factor contribution; *c*: PSCF probability distribution of the factor over the Arctic; *d*: mass percentage of the species (>1 %) within the factor.

3.4.5 Nitrate

The PMF analysis found the nitrate's pattern not comparable to any other chemical species analyzed. The result was a separate factor which represents 5.8 % of the total mass and has in his profile a high percentage of apportioned nitrate (74 %), while all the other species remain below 20 % (fig. 3.40a). Thus, this factor was read as the secondary anthropic aerosol due to the pollution caused by nitrogen oxides. This source is difficult to interpret in order to assign a geographic origin to this type of aerosol, both because its secondary formation depends on many different factors (temperature, irradiation, humidity, presence of other pollutants such as ozone), and because it has no seasonal pattern (fig. 3.40b) that can suggest a preferential air transport. The high PSCF values over the central states of the USA shown in figure 3.40c overestimates what is actually the real situation. Indeed, it was just one single strong event (2 - 4 of March) which produced high values because of the low number of total back-trajectories coming from that region. For this reason, we integrated the results with the concentration weighted trajectory (CWT) model. This approach considers the concentration of a species together with its residence time in a grid cell as follows:

$$C_{ij} = \frac{1}{\sum_{l=1}^{M} \tau_{ijl}} \sum_{l=1}^{M} C_l \tau_{ijl}$$

where C_{ij} is the average weighted concentration in the ijth cell, l is the index of the trajectory, C_l is the pollutant concentration on the arrival of l, M is the total number of trajectories, and τ_{ijl} is the time spent in the ijth cell by trajectory l. The CWT approach showed similar results to the PSCF for every factor found with PMF but, in this case, the difference allowed to exclude a high influence from the USA and to ascribe the source to the area around the

Svalbard Islands (fig. 3.39). From this result, and as seen for the ammonia-sulfate, it was impossible to link this factor to a real source region. Just a prevalent local influence was recognized, confirming the secondary origin in the atmosphere of nitrate, caused by long-range transport.

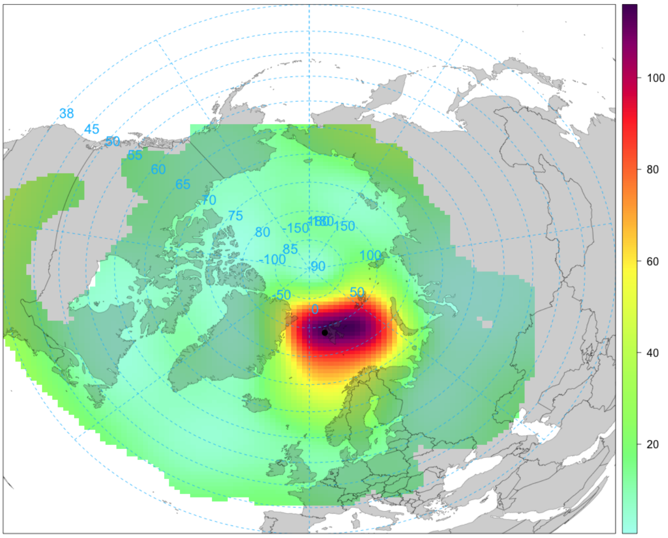

Figure 3.39 – CWT result of the nitrate factor.

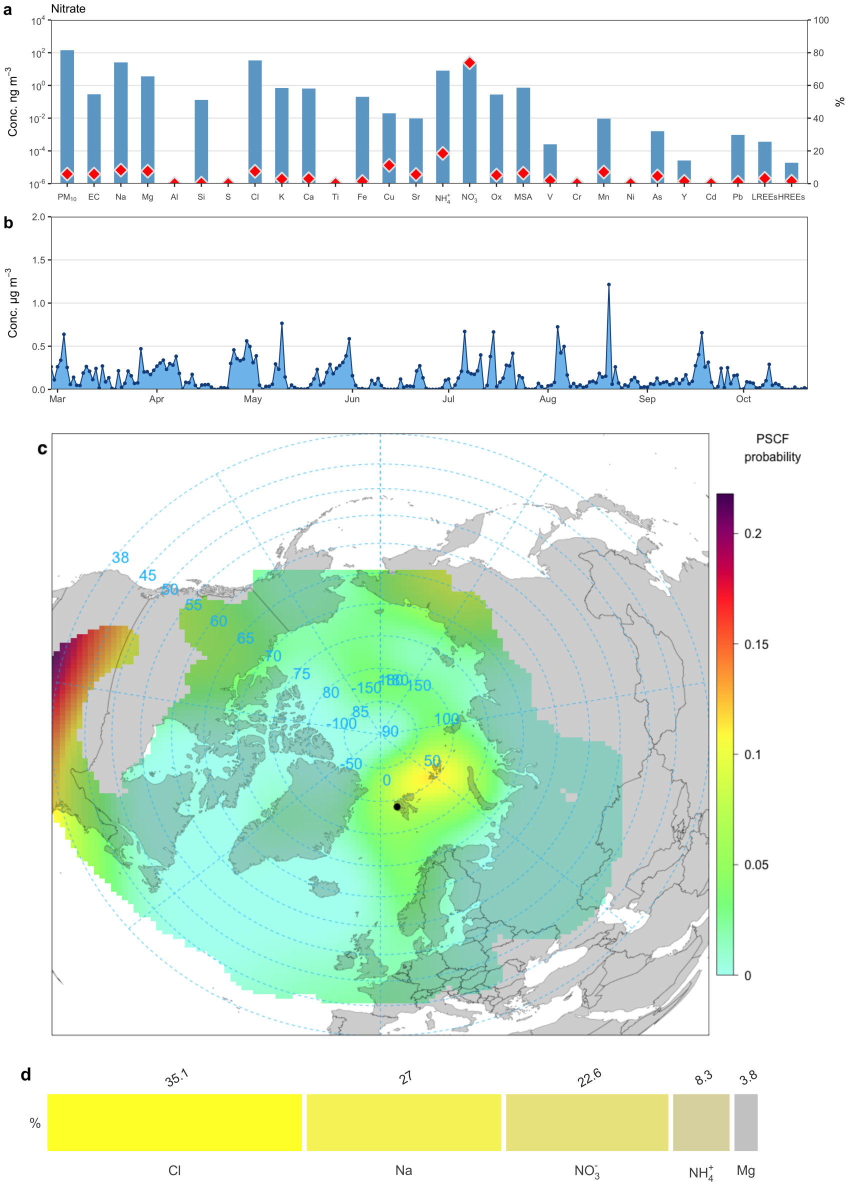

Figure 3.40 – Factor 5: Nitrate. *a*: factor profile as species mass contribution (blue bars) and percent distribution of elements within the factor (red diamonds); *b*: time series of the factor contribution; *c*: PSCF probability distribution of the factor over the Arctic; *d*: mass percentage of the species (>1 %) within the factor.

3.4.6 Biomass burning

Despite Sulfur and ammonium together constitute more than half of the factor mass (54.2 %, figure 3.44d), oxalate and elemental Carbon lead this factor, since they are present with 79 % and 53 % of their mass respectively (fig. 3.44a). The strong presence of these two species and 7.9 % of potassium (despite being only 8.6 % of its total) represent the chemical markers sufficient to associate this factor with the biomass burning source.

In the Arctic, the presence of particulate matter coming from the biomass burning source is mainly due to forest fires occurring in Russia and Northern America, especially during the summer season. A strong direct transport event, occurred between 10 and 15 July 2015, confirmed the source attribution of this factor (Moroni et al., 2017). The event is clearly visible in the time series of the factor (fig. 3.44b) and it has high values for two days and then gradually decreases in the following days. Its influence lasted for few days but was strong and continuous, thus sufficient for a back-trajectory analysis and for the chemical and physical characterization of the source. In figure 3.41 it is clear a good correspondence between the wildfire locations identified from satellite images (NASA, EOSDIS, 2015) and the starting points of the back-trajectories reaching Ny Ålesund in the days of the event (which are however limited to 5 days).

The size distribution of the particles during the event (fig. 3.42) shows that peaks of atmospheric aerosols concentrations mainly correspond with the arrival of particles in the accumulation mode (with the diameter under 0.1 µm), whereas smaller particles last longer in the atmosphere. Furthermore, a good correlation exists between oxalate and Potassium in the same days (fig. 3.43) and their linear regression coefficient ($m = 2.051$) resulted very close to the

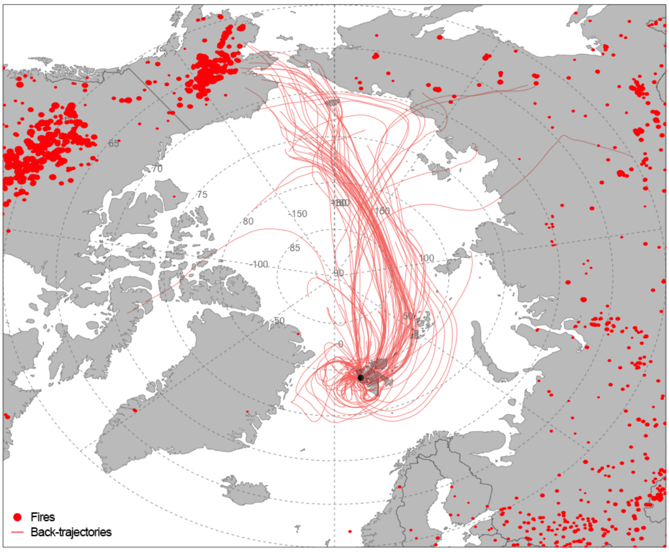

Figure 3.41 – Back-trajectories reaching Ny Ålesund between 10 and 15 of July 2015 (red lines) and map of the active fires between 28 June and 8 July 2015 (red circles, with size proportional to their brightness, source: NASA, EOSDIS, 2015).

ratio of the two ions within the factor (2.018 from fig. 3.44d).

The comprehension of this source turns out to be very important because of its high relative weight in the total aerosol load, since it represents here the second source in order of abundance, with 14.7 % of the total PM_{10}. This source has, however, a high variability because of its discontinuity and it is produced only by the occurrence of sporadic events but, at the same time, they can carry a large load of particles to the entire Arctic region. This is the case of the analyzed example, which shows the air masses passing over the Arctic ice cap. During the path of at least 5 days, the particles produced by wildfires and rich in carbonaceous substances are likely to have been subjected to multiple sedimentation processes and, consequently, a large amount of particulate matter could have been deposited on the Arctic ice cap. So, a source like this can have a very important influence on the Arctic environment and therefore great repercussions on the climate.

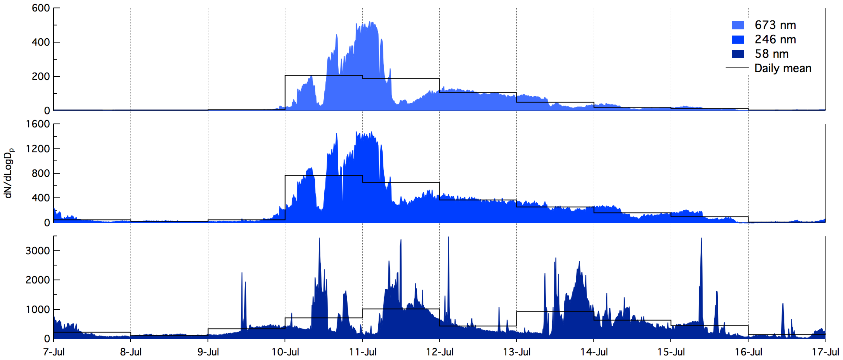

Figure 3.42 – Temporal trend of the particle counts for three size channels of SMPS particle counter (58, 246, and 673 nm), with their daily mean (black line).

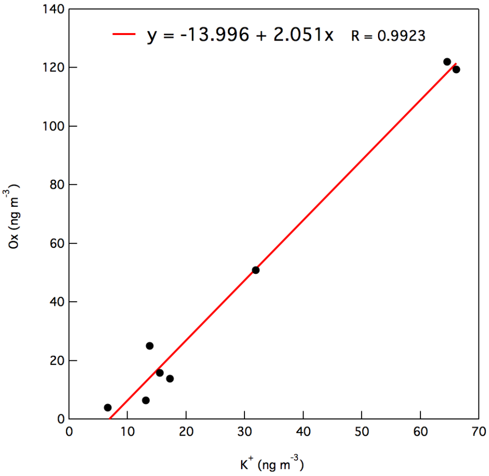

Figure 3.43 – Correlation between Oxalate and Potassium concentrations during the week of the biomass burning event.

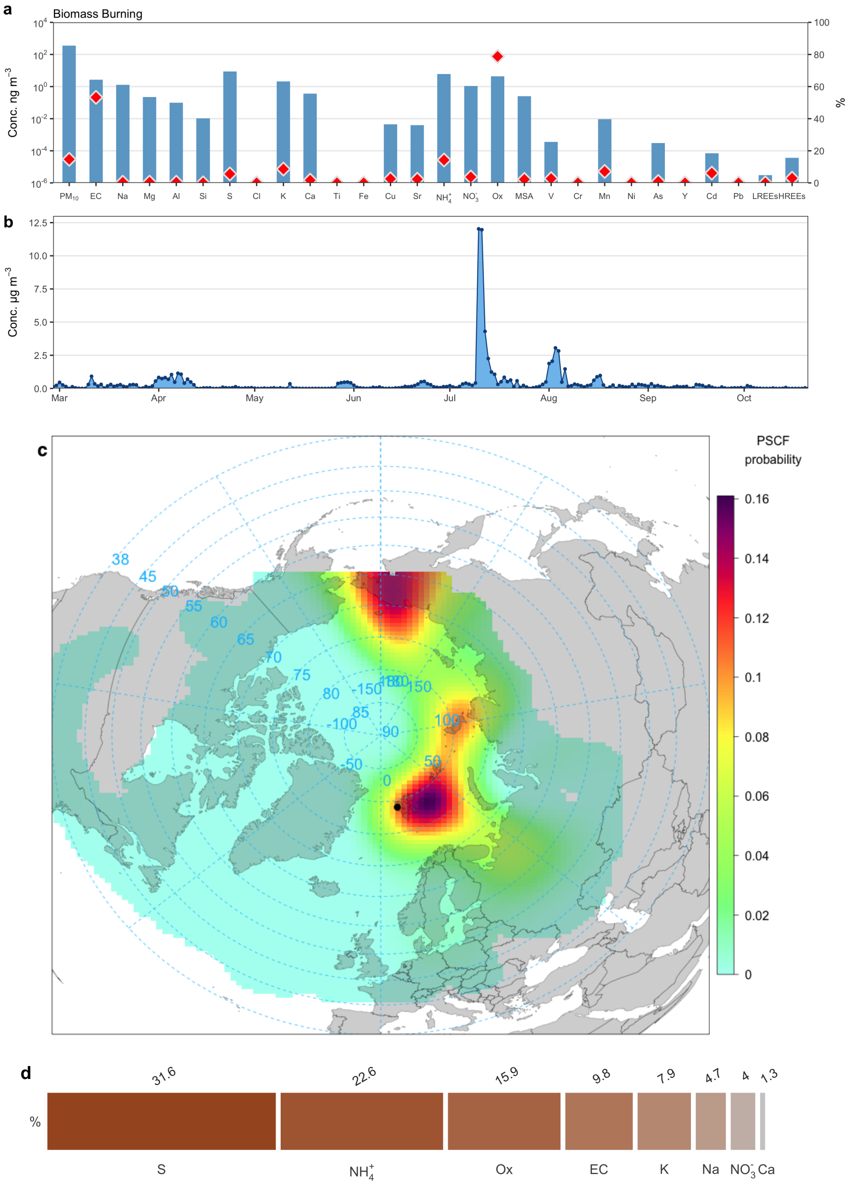

Figure 3.44 – Factor 6: Biomass Burning. *a*: factor profile as species mass contribution (blue bars) and percent distribution of elements within the factor (red diamonds); *b*: time series of the factor contribution; *c*: PSCF probability distribution of the factor over the Arctic; *d*: mass percentage of the species (>1 %) within the factor.

3.4.7 Biogenic

This factor is the last one in order of abundance since it represents just 3.3 % of the apportioned mass of the PM_{10}. Within the factor, Sulfur and MSA are together the 80.5 % and, although the first is the most abundant species, MSA lead the factor since it is the univocal chemical marker of the phytoplankton activity and it is almost completely apportioned to this factor (fig. 3.46a).

From figure 3.46b it is clear the presence of a seasonal pattern. As seen in section 3.2.7 for the only MSA, the biogenic source is characterized by the absence of contributions from October to April (i.e. the Arctic night), whereas during the rest of the year, the solar radiation triggers the biogenic activity, which is also favored by the melting of the Arctic sea ice. During the light season, three different periods are recognizable by the evolution of the factor contribution: (i) 27 February - 4 June, (ii) 4 June - 26 July, and (iii) 26 July - 21 October.

The PSCF model ascribes to the biogenic source a local origin, from the sea region around the Svalbard Islands (fig. 3.46c). However, the PSCF analysis of the three periods splits the result into as many different regions (fig. 3.45). The first source region of this factor is the northern Barents Sea (east of the sampling site). Then from June, the main influence moves southward, between the Greenland Sea and the Norwegian Sea. Finally, the third period shows a larger extension, including both the previous and the North Atlantic Ocean. Thus, this suggests a seasonal differentiation in the marine biological activity periods for these three sea regions.

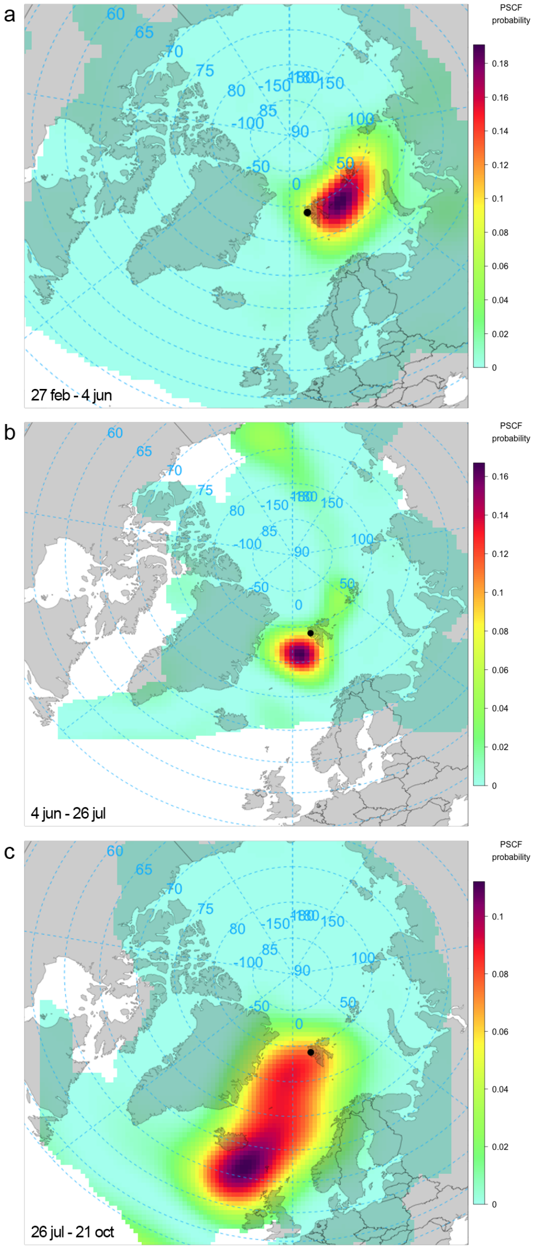

Figure 3.45 – PSCF of the biogenic contribution, applied to three different periods: 27 Feb - 4 Jun (*a*), 4 Jun - 26 Jul (*b*) and 26 Jul - 21 Oct (*c*).

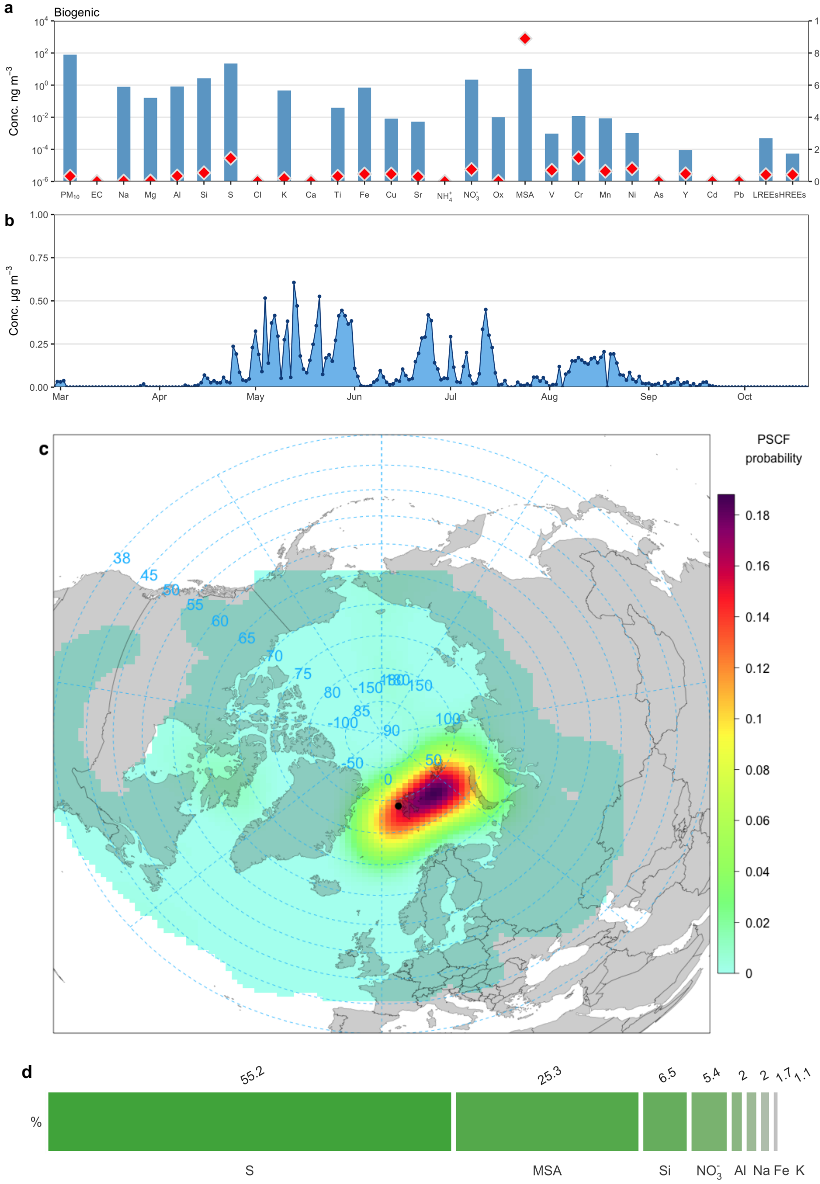

Figure 3.46 – Factor 7: Biogenic. *a*: factor profile as species mass contribution (blue bars) and percent distribution of elements within the factor (red diamonds); *b*: time series of the factor contribution; *c*: PSCF probability distribution of the factor over the Arctic; *d*: mass percentage of the species (>1 %) within the factor.

Chapter 4

Conclusions

This thesis work was carried out in the framework of the study of the Arctic environment as particularly sensitive region to the current and future climatic changes. The work was mainly focused on identifying and assessing the relative contribution of the sources and transport processes delivering aerosol to the Arctic as well on the study of aerosol production (processes of New Particle Formation). Such aims were pursued thanks to the availability a large dataset from sampling and direct measurements (size distribution) spanning a relatively large temporal frame (six years), an accurate optimization of the analytical methods applied to the chemical characterization (with special attention to Rare Earth Elements) and devoted and advanced statistical tools (Positive matrix factorization and Potential Source Contribution Function) to apportion the various sources of atmospheric particulate. During six consecutive spring-summer Arctic sampling campaigns, between 2010 and 2015, particle size-distribution measurements and aerosol sampling for chemical analysis (PM_{10} and size-segregated aerosol) were carried out at Ny Ålesund (Svalbard Islands). PM_{10} was collected at daily resolution, while a multistage impactor with a 4-day resolution was used to obtain the aerosol size distribution of the chemical characterization in the ranges: <1.0 µm, 1.0 - 2.5, 2.5 - 10 µm, and >10 µm. Samples were then analyzed by Ion Chromatography (18 ions) and Inductively Coupled Plasma - sector field Mass Spectrometry (32 metals). The results were discussed to identify and quantify the contribution of the main aerosol sources, in addition to their seasonal trend and source region.

Measurements of aerosol number concentration clearly show the seasonal cycle linked to the Arctic Haze, with accumulation mode dominating during April and May, and the Aitken mode dominating during the summer months. The Accumulation mode median particle concentration drops during this period, halving from April to August, while the Aitken number modal concentration increases with the main size mode around 35 nm. Median Nuclei concentration is quite stable, with a slight increase towards the summer months. Looking at the various interquartile ranges, a more evident increase in the different percentiles is visible, proving the presence of multiple New Particle Formation (NPF) events. The high occurrence of NPF events can be considered the result of both photochemical production of nucleating/condensing species and low so-called condensation sink (indicating how fast condensable vapor molecules can condense on the existing aerosol).

From the direct observation of the temporal evolution of the main chemical markers concentrations, it was possible to analyze the main sources of the Arctic aerosol, both natural and anthropic. The calculated sea salt Sodium (ss-Na^+), as a univocal marker of sea spray, was used to find the sea salt contribution of the other main components of sea salt source (Cl^-, ${SO_4}^{2-}$, Mg^{2+}, Ca^{2+}, and K^+). The size distribution of ss-Na^+ shows that sea spray particles are mostly distributed in the 1.0 - 10 µm range. Methanesulfonate

(MSA), mainly present in the sub-micrometric fraction, was used as the univocal biogenic marker. Its temporal trend suggested the occurrence of two periods in which the phytoplankton activity was particularly intense, with maximum values between April-July. Sulfate was found to be one of the dominant species in the Ny Ålesund aerosol and it is present mostly in the sub-micrometric range, confirming that secondary sources (via atmospheric oxidation of SO_2 and DMS atmospheric oxidation) are dominant with respect to primary emissions from sea spray and crustal scraping. The sea spray contribution was calculated from ss-Na^+, used as sea spray marker; crustal fraction was evaluated by using nss-Ca^{2+} as crustal marker; the biogenic contribution was derived by MSA, as univocal phytoplankton emission indicator. Anthropogenic sulfate was obtained as a difference between the sum of the previous contributions and the total sulfate atmospheric concentration in every sample. Sea salt aerosol contributes in the sulfate amount for about 20 % in summer, while spring values were lower (12.0 %). The crustal fraction is always low, with a relatively high contribution in summer (5.5 %). Biogenic emissions are the main sulfate source from early June to early August, accounting for 35.0 % in the summer samples. The anthropogenic fraction showed a clear seasonal pattern, being dominant in spring up to the end of May (75 % of the total sulfate budget), probably due to Arctic haze transport phenomenon, and in two short transport events (early July and mid-August). Nss-$SO_4{}^{2-}$ is long-range transported from lower-latitude industrialized areas, and its acidic form (anthropogenic and biogenic) is the most probable agent for chloride removal (as HCl) in aged sea-spray particles. The chloride depletion, with respect to seawater composition, was particularly evident in the sub-micrometric fraction and in spring, when H_2SO_4 is not completely neutralized by ammonia and free acidity is available. The linear regression between the acidic form of sulfate and ammonium was highly significant ($R = 0.94$; $n = 136$) and indicated that the mean sulfate/ammonium ratio was intermediate between semi- (NH_4HSO_4) and complete ($(NH_4)_2SO_4$) neutralization. Also in this case, a seasonal trend is clearly observed: the nss-$SO_4{}^{2-}$/$NH_4{}^+$ w/w ratio shows early-spring values higher than 5.33, corresponding to NH_4HSO_4 formation; on the other hand, summer values were consistently around 2.66, which is the ratio value corresponding to the complete neutralization of H_2SO_4 with ammonia to give $(NH_4)_2SO_4$. This is in agreement with the spring and summer ionic balances, where anion equivalents are counterbalanced by cations, avoiding the necessity to invoke the presence of extra H^+ or $HCO_3{}^-$ equivalents to compensate possible unbalances.

In this work, we also demonstrated the applicability of a method based on an ICP-MS system coupled with a microflow nebulizer and a desolvation system for the quantification of metals in samples of Arctic particulate matter. The desolvation system, compared to the spray chamber introduction, allows reducing the presence of isobaric interferences, which are mainly due to oxide formation in the plasma. This avoids any mathematical corrections and enables the use of the low resolution configuration for many elements, with a significant gain in terms of signal. Despite the very low detection limits of the methods, the determination of trace and ultra-trace elements in samples characterized by such a little load of atmospheric aerosols may be significantly affected by the blank levels, hence an accurate study of blank values was carried out. The performances of this method were studied in particular for the determination of Rare Earth Elements, which show for most of the cases recoveries larger than 80 %, with the exception of Sc. The high performances of the instrument led to the development of a powerful method for the quantification of a large number of metals in the first multi-year daily series of Arctic PM_{10} samples, collected with a low-volume device in Ny Ålesund (Svalbard Islands), between 2010 and 2015. The study of REEs correlations in the samples reveals the partition of the group between light REEs (from La to Sm) and heavy REEs (from Gd to Lu) and an additional weaker partition based on the even or odd atomic number of the elements. The analysis of their temporal pattern shows an increase of the variability during the summer months for both the air concentration and the light/heavy REEs ratio. The Cerium and Europium anomalies appeared to be suitable tools for a preliminary sources identification. Most samples show no Cerium anomaly, negative Europium anomaly and high light/heavy REEs ratio. From spring to summer a decrease in Cerium anomaly and in LREE/HREE ratio was observed; on the contrary, Europium anomaly exhibited a clear increase. Such a temporal pattern suggests a different contribution of the local and long-range transported dust, which affect with a different extent the two seasons, i.e. larger contribution of local dust occurring in the summer period, when larger areas become active in dust production after snow melting.

Thanks to the large database of the chemical composition of the samples collected during 2015 (expanded with PIXE and elemental carbon data), two receptor models were applied: the Positive Matrix Factorization (PMF), for the source type identification, and the Potential Source Contribution Function (PSCF), which uses the air mass back-trajectories to recognize the source geographic regions of the particles reaching Ny Ålesund and bringing high concentrations of a chemical species (i.e. the factor contribution in this work). Seven factors were found through PMF, which apportioned 86 % of the total PM_{10}, whereas the chemical markers allowed to recognize the types of sources affecting the Arctic aerosols. So, the chemical profile obtained for each source allowed a better estimate of their chemical composition, both in terms of contribution of the chemical species to the total weight of the source and their subdivision in the factors. On the other hand, the distribution of the factors within the 237 daily samples allowed analyzing the seasonal trend of each source.

Sea salt and soil are the natural sources of the primary Arctic aerosol and together represent the 54.4 % of PM_{10} load (46.0 % and 8.4 % respectively). Both sources do not exhibit a clear seasonal pattern in the analyzed period. Despite it is not possible to exclude a local influence for both, the main sources of marine aerosols are the seas south of the Svalbard Islands, which are free from sea ice: the largest contribution comes from the Norwegian Sea, then from the Barents Sea and the Greenland Sea; as concerning the origin of the crustal input to the atmospheric aerosols in Ny Ålesund, it is mainly attributed to central Russia and the dry land facing towards the Svalbard Islands.

The biological activity of the phytoplankton is the main natural source of secondary aerosols. It affects only 3.3 % of the Arctic aerosol in terms of load but still gives a remarkable contribution to the atmospheric sulfate concentration (together with MSA, its main marker), especially during spring and summer. Indeed, since the solar radiation and the melting of sea ice trigger the marine biological activity, this aerosol source is present almost exclusively from April to September. During these months, this type of aerosol reaches the sampling site from three different regions (starting from the Barents Sea to the North Atlantic Ocean), suggesting a different seasonality for the marine biological activity of the Arctic seas.

Regarding the anthropic sources, heavy metals drive the primary aerosol fraction, which is 5.5 % of the total PM_{10} budget. The strong seasonality of this type of aerosol is clear from the recurring presence of high values until April, which concentrate most of its mass in this period (83 %), whereas its presence is almost negligible since May. A considerable influence is due to the major industrial areas of Central and Western Russia, while the total mass of anthropogenic aerosol shows a source from both eastern North America and the extended Arctic regions between western Russia and northern Greenland. The occurrence of air masses from this latter region and the temporal trend, confirm how closely this type of aerosol is related to the Arctic haze, since particles remain trapped in the Arctic atmosphere for long periods during this phenomenon (relatively to their atmospheric residence time) and thus appear to have a local source.

The same geographic apportionment result was obtained for the other two anthropic aerosol sources: ammonia-sulfates and nitrate, that account for 16.3 % and 5.8 % respectively. Indeed, both represent secondary aerosol and therefore it was impossible to ascribe a source region. The back-trajectory study can only confirm the permanence or formation of these species in the Arctic atmosphere, coming from long-range transport. Although the presence of nitrates does not have a clear seasonal trend during the sampling period, the ammonia-sulfate source shows a seasonality which is similar to that seen for heavy metals, with high values in spring and early summer, confirming the transport of a large amount of sulfates due to this atmospheric phenomenon. During the summer there is still a small presence of ammonium and sulfates which, as seen above, are mainly present in the two forms of neutralization.

Finally, the biomass burning source was also studied. Its contribution reaches 14.7 % of the total and has a high variability, linked to forest fire occurrences. A large aerosol event, which happened in July 2015 and lasted for a few days, made possible the characterization of this source, thanks to the connection of extensive forest fires in Alaska with fast air transport processes towards the Svalbard Islands. Oxalate, Potassium and elemental Carbon have proved to be reliable markers of this source, whose existence can be attributed both to natural and anthropic causes and which can have a decisive weight on the Arctic environment, especially due to the large aerosol loads that it can emit into the atmosphere and the direct effect of black carbon (released in huge amounts during fires) on the atmospheric radiative balance.

The achieved results represent a contribution to the complex study of identification and quantification of Arctic aerosol sources, although a significant work is yet to be carried out at this purpose. There are still, for example, uncertainty about sulfates due to their many sources. To obtain more significant results, many points that can be worked on and improved; among them: (i) enlargement of the sampling period to all year round, during periods of very low or totally lacking incoming solar radiation, in order to better capture the role of sunlight in triggering atmospheric reactions and oceanic productivity; (ii) improvement of PMF analysis by extending it to the other sampling years and better constraining the errors associated with the results; (iii) improvement of PSCF model by inserting a weight function to underestimate small transport events. However, the results here reported provide useful information in evaluating the relevance of the impact of anthropogenic aerosol on the critical Arctic ecosystem and in improving climate models based on aerosol-solar irradiation interaction processes.

References

Albrecht, B.A. (1989). Aerosols, cloud microphysics and fractional cloudiness. *Science* 245, pp. 1227–1230. DOI: 10.1126/science.245.4923.1227.

Ara, B., E. Kim, C.H. Jeong, D.W. Lee, and P.K. Hopke (2005). Evaluation of the potential source contribution function using the 2002 Quebec forest fire episode. *Atmospheric Environment* 39, pp. 3719–3724. DOI: 10.1016/j.atmosenv.2005.03.008.

Asmi, E., V. Kondratyev, D. Brus, T. Laurila, H. Lihavainen, J. Backman, V. Vakkari, M. Aurela, J. Hatakka, Y. Viisanen, T. Uttal, V. Ivakhov, and A. Makshtas (2015). Aerosol size distribution seasonal characteristics measured in Tiksi, Russian Arctic. *Atmospheric Chemistry and Physics Discussions* 15, pp. 18109–18149. DOI: 10.5194/acpd-15-18109-2015.

Barone, S.B., A.A. Turnipseed, and A.R. Ravishankara (1995). Role of adducts in the atmospheric oxidation of dimethyl sulfide. *Faraday Discuss* 100, pp. 39–54. DOI: 10.1039/FD9950000039.

Barrie, L.A. (1986). Arctic air pollution: an overview of current knowledge. *Atmospheric Environment* 20, pp. 643–663. DOI: 10.1016/0004-6981(86)90180-0.

Bates, T.S., J.A. Calhoun, and P.K. Quinn (1992). Variations in the methane-sulfonate to sulfate molar ratio in submicrometer marine aerosol particles over the south Pacific Ocean. *Journal of Geophysics Research* 97.D9, pp. 9859–9865. DOI: 10.1029/92JD00411.

Bazzano, A., F. Ardini, S. Becagli, R. Traversi, R. Udisti, D. Cappelletti, and M. Grotti (2015). Source assessment of atmospheric lead measured at Ny-Ålesund, Svalbard. *Atmospheric Environment* 113, pp. 20–26. DOI: 10.1016/j.atmosenv.2015.04.053.

Bazzano, A., F. Ardini, M. Grotti, M. Malandrino, A. Giacomino, O. Abollino, D. Cappelletti, S. Becagli, R. Traversi, and R. Udisti (2016). Elemental and lead isotopic composition of atmospheric particulate measured in the Arctic region (Ny-Ålesund, Svalbard Islands). *Rendiconti Lincei* 27.1, pp. 73–84. DOI: 10.1007/s1221.

Becagli, S., C. Scarchilli, R. Traversi, U. Dayan, M. Severi, D. Frosini, V. Vitale, M. Mazzola, A. Lupi, S. Nava, and R. Udisti (2012). Study of present-day sources and transport processes affecting oxidised sulphur compounds in atmospheric aerosols at Dome C (Antarctica) from year-round sampling campaigns. *Atmospheric Environment* 52, pp. 98–108. DOI: 10.1016/j.atmosenv.2011.07.053.

Becagli, S., L. Lazzara, F. Fani, C. Marchese, R. Traversi, M. Severi, A. di Sarra, D. Sferlazzo, S. Piacentino, C. Bommarito, U. Dayan, and R. Udisti (2013). Relationship between methanesulfonate in atmospheric particulate and remotely sensed phytoplankton activity in oligo-mesotrophic central Mediterranean Sea. *Atmospheric Environment* 79, pp. 681–688. DOI: 10.1016/j.atmosenv.2013.07.032.

Bodhaine, B.A. (1989). Barrow surface aerosol: 1976-1986. *Atmospheric Environment* 23, pp. 2357–2369. DOI: 10.1016/0004-6981(89)90249-7.

Bowen, H.J.M. (1979). *Environmental Chemistry of the Elements.* Academic Press.

Boynton, W.V. (1984). *Cosmochemistry of the rare earth elements; meteorite studies.* Ed. by Elsevier. Henderson, P., pp. 63–114.

Byrne, R. H. and K. Kim (1992). Rare earth precipitation and coprecipitation behavior: The limiting role of ${PO_4}^{3-}$ on dissolved rare earth concentrations in seawater. *Geochimica et Cosmochimica Acta* 57, pp. 519–526. DOI: 10.1016/0016-7037(93)90364-3.

Calzolai, G., M. Chiari, F. Lucarelli, S. Nava, F. Taccetti, S. Becagli, D. Frosini, R. Traversi, and R. Udisti (2014). PIXE-PIGE analysis of size-segregated aerosol samples from remote areas. *Nuclear Instruments and Methods in Physics Research Section B* 318, pp. 125–129. DOI: 10.1016/j.nimb.2013.05.097.

Cantrell, K. J. and R. H. Byrne (1987). Rare Earth Element complexation by carbonate and oxalate ions. *Geochimica et Cosmochimica Acta* 51, pp. 597–605. DOI: 10.1016/0016-7037(87)90072-X.

Carslaw, D.C. and K. Ropkins (2012). openair - An R package for air quality data analysis. *Environmental Modelling and Software* 27-28, pp. 52–61. DOI: 10.1016/j.envsoft.2011.09.008.

Carslaw, K. S., L.A. Lee, C.L. Reddington, K.J. Pringle, A. Rap, P.M. Forster, G.W. Mann, D.V. Spracklen, M.D. Woodhouse, L.A. Regayre, and J.R. Pierce (2013). Large contribution of natural aerosols to uncertainty in indirect forcing. *Nature* 503, pp. 67–79. DOI: 10.1038/nature12674.

Chang, R.Y.W., C. Leck, M. Graus, M. Müller, J. Paatero, J.F. Burkhart, A. Stohl, L.H. Orr, K. Hayden, S.M. Li, A. Hansel, M. Tjernström, W.R. Leaitch, and J.P.D. Abbatt (2011). Aerosol composition and sources in the central Arctic Ocean during ASCOS. *Atmospheric Chemistry and Physics* 11, pp. 10619–10636. DOI: 10.5194/acp-11-10619-2011.

Charlson, R.J., J.E. Lovelock, M.O. Andreae, and S.G. Warren (1987). Oceanic phytoplankton, atmospheric sulphur, cloud albedo and climate. *Nature* 326.6114, pp. 655–661. DOI: 10.1038/326655a0.

Covert, D.S., A. Wiedensohler, P. Aalto, J. Heintzenberg, P.H. McMurry, and C. Leck (1996). Aerosol number size distribution from 3 to 500 nm diameter in the arctic marine boundary layer during summer and autumn. *Tellus* 48B, pp. 197–212. DOI: 10.1029/2002JD002533.

Dal Maso, M., M. Kulmala, I. Riipinen, R. Wagner, T. Hussein, P.P. Aalto, and K.E.J. Lehtinen (2005). Formation and growth of fresh atmospheric aerosols: eight years of aerosol size distribution data from SMEAR II, Hyytiala, Finland. *Boreal Environmental Research* 10, pp. 323–336. DOI: 10.1.1.562.3319.

Das, R., S.N. Das, and V.N. Misra (2005). Chemical composition of rainwater and dustfall at Bhubaneswar in the east coast of India. *Atmospheric Environment* 39, pp. 5908–5916. DOI: 10.1016/j.atmosenv.2005.06.030.

De Carlo, E.H., X.Y. Wen, and M. Irving (1998). The influence of redox reactions on the uptake of dissolved Ce by suspended Fe and Mn oxide particles. *Aquatic Geochemistry* 3.4, pp. 357–389. DOI: 10.1023/A:1009664626181.

Draxler, R.R. and G.D. Rolph (1997). *HYSPLIT4 (Hybrid Single-Particle Lagrangian Integrated Trajectory) Model.* NOAA Air Resources Laboratory, Silver Spring, MD. URL: `http://www.arl.noaa.gov/ready/hysplit4.html`.

Du, L. and J. Turner (2015). Using PM2.5 lanthanoid elements and nonparametric wind regression to track petroleum refinery FCC emissions. *Science of the Total Environment* 529, pp. 65–71. DOI: `10.1016/j.scitotenv.2015.05.034`.

EOSDIS (2015). *NASA - Earth Observing System Data and Information System.* URL: `https://firms.modaps.eosdis.nasa.gov`.

Engvall, A.C., R. Krejci, J. Ström, R. Treffeisen, R. Scheele, O. Hermansen, and J. Paatero (2008). Changes in aerosol properties during spring–summer period in the Arctic troposphere. *Atmospheric Chemistry and Physics* 8, pp. 445–462. DOI: `10.5194/acp-8-445-2008`.

Fan, A.X., P.K. Hopke, T.M. Raunemaa, M. Oblad, and J.M. Pacyna (1995). A study on the potential sources of air pollutants-observed at Tjörn, Sweden. *Environmental Science and Pollution Research* 2.2, pp. 107–115. DOI: `10.1007/BF02986733`.

Ferrat, M., D.J. Weiss, S. Strekopytov, S. Donga, H. Chen, J. Najorka, Y. Sunc, S. Guptaa, R. Tada, and R. Sinha (2011). Improved provenance tracing of Asian dust sources using rare earth elements and selected trace elements for palaeomonsoon studies on the eastern Tibetan Plateau. *Geochimica et Cosmochimica Acta* 75, pp. 6374–6399. DOI: `10.1016/j.gca.2011.08.025`.

Fisher, J.A., D.J. Jacob, Q. Wang, R. Bahreini, C.C. Carouge, M.J. Cubison, J.E. Dibb, T. Diehl, J.L. Jimenez, E.M. Leibensperger, Z. Lu, M.B.J. Meinders, O.T. Havala Pye, P.K. Quinn, S. Sharma, D.G. Streets, A. van Donkelaar, and R.M. Yantosca (2011). Sources, distribution, and acidity of sulfate-ammonium aerosol in the Arctic in winter-spring. *Atmospheric Environment* 45, pp. 7301–7318. DOI: `10.1016/j.atmosenv.2011.08.030`.

Gao, N., M.D. Cheng, and P.K. Hopke (1993). Potential source contribution function analysis and source apportionment of sulfur species measured at Rubidoux, CA during the southern California air quality study, 1987. *Analytica Chimica Acta* 277, pp. 369–380. DOI: `10.1016/`

0003-2670(93)80449-U.

Gondwe, M., M. Krol, W. Gieskes, W. Klaassen, and H. de Baar (2003). The contribution of ocean-leaving DMS to the global atmospheric burdens of DMS, MSA, SO_2, and $nssSO_4^{2-}$. *Global Biogeochem Cycles* 17.2, p. 1056. DOI: 10.1029/2002GB001937.

Gondwe, M., M. Krol, W. Klaassen, W. Gieskes, and H. de Baar (2006). Comparison of modeled versus measured MSA:nss SO4 ratios: A global analysis. *Global Biogeochemical Cycles* 18. DOI: 10.1029/2003GB002144.

Hafner, W.D. and R.A. Hites (2003). Potential sources pesticides, PCBs, and PAHs to the atmosphere of the Great Lakes. *Environmental Science and Technology* 37, pp. 3764–3773. DOI: 10.1021/es034021f.

Heintzenberg, J., H.C. Hansson, and H. Lannefors (1981). The chemical composition of Arctic haze at Ny-Alesund, Spitsbergen. *Tellus* 33, pp. 162–171. DOI: 10.1111/j.2153-3490.1981.tb01741.x.

Henderson, P. and G.M. Henderson (2009). *The Cambridge handbook of earth science data*. Cambridge University Press.

Hsu, Y.-K., T.M. Holsen, and P.K. Hopke (2003). Locating and quantifying PCB sources in Chicago: receptor modeling and field sampling. *Environmental Science and Technology* 37, pp. 681–690. DOI: 10.1021/es025531x.

Hynes, A.J., P.H. Wine, and D.H. Semmes (1986). Kinetics and mechanism of hydroxyl reactions with organic sulfides. *Journal of Physical Chemistry* 90, pp. 4148–4156. DOI: 10.1021/j100408a062.

IPCC (2013). IPCC 2014. Ed. by B. Kirtman, S.B. Power, J.A. Adedoyin, G.J. Boer, R. Bojariu, I. Camilloni, F.J. Doblas-Reyes, A.M. Fiore, M. Kimoto, G.A. Meehl, M. Prather, A. Sarr, C. Schär, R. Sutton, G.J. van Oldenborgh, G. Vecchi, and H.J. Wang. Vol. Climate Change 2013: The Physical Science Basis. Contribution of Working Group I to the Fifth Assessment Report of the Intergovernmental Panel on Climate Change. Cambridge University Press. Chap. Near-term Climate Change: Projec- tions and Predictability.

Iversen, T. and E. Joranger (1985). Arctic air-pollution and large scale atmospheric flows. *Atmospheric Environment* 19, pp. 2099–2108. DOI: 10.1016/0004-6981(85)90117-9.

Järvinen, E., A. Virkkula, T. Nieminen, P.P. Aalto, E. Asmi, C. Lanconelli, M. Busetto, A. Lupi, R. Schioppo, V. Vitale, M. Mazzola, T. Petäjä, V.M. Kerminen, and M. Kulmala (2013). Seasonal cycle and modal structure of particle number size distribution at Dome C, Antarctica. *Atmospheric Chemistry and Physics* 13, pp. 7473–7487. DOI: `10.5194/acp-13-7473-2013`.

Karl, M., A. Gross, C. Leck, and L. Pirjola (2007). Intercomparison of dimethylsulfide oxidation mechanisms for the marine boundary layer: gaseous and particulate sulfur constituents. *Journal of Geophysics Research* 112.D15304. DOI: `10.1029/2006JD007914`.

Kettle, A.J. and M.O. Andreae (2000). Flux of dimethylsulfide from the oceans: a comparison of updated data sets and flux models. *Journal of Geophysics Research* 105.D22, pp. 26793–26808. DOI: `10.1029/2000JD900252`.

Kltto, M.E., D.L. Anderson, G.E. Gordon, and I. Olmez (1992). Rare Earth Distributions in Catalysts and Airborne Particles. *Environmental Science and Technology* 1375.30, pp. 1368–1375. DOI: `10.1021/es00031a014`.

Koeppenkastrop, D., E.H. De Carlo, and M. Roth (1991). A method to investigate the interaction of Rare Earth Elements in aqueous solution with metal oxides. *Journal of Chemical Information and Modeling* 152.2, pp. 337–346. DOI: `10.1017/CBO9781107415324.004`.

Kulkarni, P., S. Chellam, J.B. Flanagan, and R.K.M. Jayanty (2007). Microwave digestion - ICP-MS for elemental analysis in ambient airborne fine particulate matter: Rare earth elements and validation using a filter borne fine particle certified reference material. *Analytica Chimica Acta* 599, pp. 170–176. DOI: `10.1016/j.aca.2007.08.014`.

Kulshrestha, U.C., A.K. Sarkar, S.S. Srivastava, and D.C. Parashar (1996). Investigation into atmospheric deposition through precipitation studies at New Delhi (India). *Atmospheric Environment* 30, pp. 4149–4154. DOI: `10.1016/1352-2310(96)00034-9`.

Leck, C. and M. Hetinzenberg J. Engard (2002). A meridional profile of the chemical composition of submicrometer particles over the Atlantic Ocean: aerosol sources and hemispheric variabilities. *Tellus* 54, pp. 377–384. DOI: `10.1034/j.1600-0889.2002.01318.x`.

Leck, C. and C. Persson (1996). Seasonal and short-term variability in dimethyl sulfide, sulfur dioxide and biogenic sulfur and sea salt aerosol particles in the arctic marine boundary layer during summer and autumn. *Tellus B* 48, pp. 272–299. DOI: 10.1034/j.1600-0889.48.issue2.1.x.

Li, S.M. and L.A. Barrie (1993). Biogenic sulfur aerosol in the Arctic troposphere: 1. contributions to total sulfate. *Journal of Geophysics Research* 98.D11, pp. 20613–20622. DOI: 10.1029/93JD02234.

Maenhaut, W., W.H. Zoller, R.A. Duce, and G.L. Hoffman (1979). Concentration and size distribution of particulate trace elements in the south polar atmosphere. *Journal of Geophysics Research* 84.C5, pp. 2421–2431. DOI: 10.1029/JC084iC05p02421.

Maenhaut, W., P. Cornille, J.M. Pacyna, and V. Vitols (1989). Trace element composition and origin of the atmospheric aerosol in the norwegian Arctic. *Atmospheric Environment* 23.11, pp. 2551–2569. DOI: 10.1016/0004-6981(89)90266-7.

Mazzera, D.M., D.H. Lowenthal, J.C. Chow, J.G. Watson, and V. Grubisíc (2001). PM10 measurements at McMurdo Station, AntArctica. *Atmospheric Environment* 35.10, pp. 1891–1902. DOI: 10.1016/S1352-2310(00)00409-X.

Mazzola, M., A.P. Viola, C. Lanconelli, and V. Vitale (2016). Atmospheric observations at the Amundsen-Nobile Climate Change Tower in Ny-Ålesund, Svalbard. *Rendiconti Lincei* 27.1, pp. 7–18. DOI: 10.1007/s12210-016-0540-8.

Moorthy, K.K., V. Sreekanth, J.P. Chaubey, M.M. Gogoi, S.S. Babu, S.K. Kompalli, S.P. Bagare, B.C. Bhatt, V.K. Gaur, T.P. Prabhu, and N.S. Singh (2011). Fine and ultrafine particles at a near–free tropospheric environment over the high-altitude station Hanle in the Trans- Himalaya: new particle formation and size distribution. *Journal of Geophysics Research* 116, p. D20212. DOI: 10.1029/2011JD016343.

Moreno, T., X. Querol, S. Castillo, A. Alastuey, E. Cuevas, L. Herrmann, M. Mounkaila, J. Elvira, and W. Gibbons (2006). Geochemical variations in aeolian mineral particles from the Sahara - Sahel Dust Corridor. *Chemosphere* 65, pp. 261–270. DOI: 10.1016/j.chemosphere.2006.02.052.

Moreno, T., X. Querol, A. Alastuey, and W. Gibbons (2008). Identification of FCC refinery atmospheric pollution events using lanthanoid- and vanadium-bearing aerosols. *Atmospheric Environment* 42, pp. 7851–7861. DOI: `10.1016/j.atmosenv.2008.07.013`.

Moreno, T., X. Querol, A. Alastuey, J. de la Rosa, A.M. Sánchez de la Campa, M. Minguillón, M. Pandolfi, Y. Gonzalez-Castanedo, E. Monfort, and W. Gibbons (2010). Variations in vanadium, nickel and lanthanoid element concentrations in urban air. *Science of the Total Environment* 408.20, pp. 4569–4579. DOI: `10.1016/j.scitotenv.2010.06.016`.

Moroni, B., S. Becagli, E. Bolzacchini, M. Busetto, D. Cappelletti, S. Crocchianti, L. Ferrero, D. Frosini, C. Lanconelli, A. Lupi, M. Maturilli, M. Mazzola, M.G. Perrone, G. Sangiorgi, R. Traversi, R. Udisti, A. Viola, and V. Vitale (2015). Vertical profiles and chemical properties of aerosol particles upon Ny-Ålesund (Svalbard Island). *Advances in Meteorology* 2015, Article ID 292081. DOI: `10.1155/2015/292081`.

Moroni, B., D. Cappelletti, L. Ferrero, S. Crocchianti, M. Busetto, M. Mazzola, S. Becagli, R. Traversi, and R. Udisti (2016). Local vs. long-range sources of aerosol particles upon Ny-Ålesund (Svalbard Islands): mineral chemistry and geochemical records. *Rendiconti Lincei* 27.1, pp. 115–127. DOI: `10.1007/s12210-016-0533-7`.

Moroni, B., D. Cappelletti, S. Crocchianti, S. Becagli, L. Caiazzo, R. Traversi, R. Udisti, M. Mazzola, K. Markowicz, and T. Ritter C. Zielinski (2017). Morphochemical characteristics and mixing state of long range transported wildfire particles at Ny-Ålesund (Svalbard Islands). *Atmospheric Environment* 156, pp. 135–145. DOI: `10.1016/j.atmosenv.2017.02.037`.

NOAA. *Air Resources Laboratory.* URL: `http://ready.arl.noaa.gov/gdas1.php`.

Norman, A.L., L.A. Barrie, D. Toom-Sauntry, A. Sirois, H.R. Krouse, S.M. Li, and S. Sharma (1999). Sources of aerosol sulphate at Alert: apportionment using stable isotopes. *Journal of Geophysics Research* 104.D9, pp. 11619–11631. DOI: `10.1029/1999JD900078`.

Pacyna, J.M. and B. Ottar (1985). Transport and chemical composition of the summer aerosol in the Norwegian Arctic. *Atmospheric Environment*

19.12, pp. 2109–2120. DOI: 10.1016/0004-6981(85)90118-0.

Pacyna, J.M., B. Ottar, U. Tomza, and W. Maenhaut (1985). Transport of trace elements to Ny Alesund, Spitsbergen. *Atmospheric Environment* 19.6, pp. 857–865. DOI: 10.1016/0004-6981(85)90231-8.

Pekney, N.J., C.I. Davidson, L. Zhou, and P.K. Hopke (2006). Application of PSCF and CPF to PMF-Modeled Sources of PM 2.5 in Pittsburgh. *Aerosol Science and Technology* 40, pp. 952–961. DOI: 10.1080/02786820500543324.

Pincus, R. and M. Baker (1994). Effect of precipitation on the albedo susceptibility of clouds in the marine boundary layer. *Nature* 372, pp. 250–252. DOI: 10.1038/372250a0.

Pithan, F. and T. Mauritsen (2014). Arctic amplification dominated by temperature feedbacks in contemporary climate models. *Nature Geoscience* 7, pp. 181–184. DOI: 10.1038/ngeo2071.

Polissar, A.V., P.K. Hopke, and R.L. Poirot (2001). Atmospheric aerosol over Vermont: Chemical composition and sources. *Environmental Science and Technology* 35.23, pp. 4604–4621. DOI: 10.1021/es0105865.

Pourmand, A., J.M. Prospero, and A. Sharifi (2014). Geochemical fingerprinting of trans-Atlantic African dust based on radiogenic Sr-Nd-Hf isotopes and rare earth element anomalies. *Geology* 42.8, pp. 675–678. DOI: 10.1130/G35624.1.

Quinn, P.K., T.L. Miller, T.S. Bates, J.A. Ogren, E. Andrews, and G. Shaw (2002). A three-year record of simultaneously measured aerosol chemical and optical properties at Barrow, Alaska. *Journal of Geophysics Research* 107.D11, pp. 1–15. DOI: 10.1029/2001JD001248.

Quinn, P.K., G. Shaw, E. Andrews, E.G. Dutton, T. Ruoho-Airola, and S.L. Gong (2007). Arctic haze: current trends and knowledge gaps. *Tellus* 59B, pp. 99–114. DOI: 10.1111/j.1600-0889.2006.00238.x.

R-Core-Team (2016). *R: A language and environment for statistical computing*. R Foundation for Statistical Computing, Vienna, Austria. DOI: https://www.R-project.org/.

Riley, J.P. and R. Chester (1971). *Introduction to Marine Chemistry*. Academic Press.

Robock, A. (1983). Ice and snow feedbacks and the latitudinal and seasonal distribution of climate sensitivity. *Journal of the Atmospheric Sciences*

40, pp. 986–997. DOI: `10.1175/1520-0469(1983)040<0986:IASFAT>2.0.CO;2`.

Röthlisberger, R., R. Mulvaney, E.W. Wolff, M.A. Hutterli, M. Bigler, S. Sommer, and J. Jouzel (2002). Dust and sea salt variability in central East Antarctica (Dome C) over the last 45 kyrs and its implications for southern high-latitude climate. *Geophysical Research Letters* 29, p. 1963. DOI: `10.1029/2002GL015186`.

Saltzman, E.S. (1995). *Ice core studies of global biogeochemical cycles.* Ed. by R.J. Delmas. Berlin: Springer-Verlag. Chap. Ocean/atmosphere cycling of dimethylsulfide, pp. 65–90.

Scheuer, E., R.W. Talbot, J.E. Dibb, G.K. Seid, L. DeBell, and B. Lefer (2003). Seasonal distributions of fine aerosol sulfate in the North American Arctic basin during TOPSE. *Journal of Geophysics Research* 108.D4, p. 8370. DOI: `10.1029/2001JD001364`.

Screen, J.A. and I. Simmonds (2010). The central role of diminishing sea ice in recent Arctic temperature amplification. *Nature* 464, pp. 1334–1337. DOI: `10.1038/nature09051`.

Serreze, M.C. and J.A. Francis (2006). The Arctic amplification debate. *Clinatic Change* 76, pp. 241–264. DOI: `10.1007/s10584-005-9017-y`.

Shaw, G. (1984). Microparticle size spectrum of Arctic haze. *Geophysical Research Letters* 11, pp. 409–412. DOI: `10.1029/GL011i005p00409`.

Shindell, D. and G. Faluvegi (2009). Climate response to regional radiative forcing during the twentieth century. *Nature Geoscience* 2.4, pp. 294–300. DOI: `10.1038/ngeo473`.

Sholkovitz, E. R. (1992). Chemical evolution of rare earth elements: fractionation between colloidal and solution phases of filtered river water. *Earth and Planetary Science Letters* 144, pp. 77–84. DOI: `10.1016/0012-821X(92)90152-L`.

Stohl, A. (1996). Trajectory statistics-a new method to establish source–receptor relationships of air pollutants and its application to the transport of particulate sulfate in Europe. *Atmospheric Environment* 30, pp. 579–587. DOI: `10.1016/1352-2310(95)00314-2`.

Stohl, A., A. Klimont, S. Eckhardt, K. Kupiainen, V.P. Shevchenko, V.M. Kopeikin, and A.N. Novigatsky (2013). Black carbon in the Arctic: the underestimated role of gas flaring and residential combustion emissions.

Atmospheric Chemistry and Physics 13, pp. 8833–8855. DOI: 10.5194/acp-13-8833-2013.

Stroeve, J., M.M. Holland, W. Meier, T. Scambos, and M. Serreze (2007). Arctic sea ice decline: Faster than forecast. *Geophysical Research Letters* 34. DOI: 10.1029/2007GL029703.

Ström, J., J. Umegård, K. Tørseth, P. Tunved, H.C. Hansson, K. Holmén, V. Wismann, A. Herber, and G. König-Langlo (2003). One year of particle size distribution and aerosol chemical composition measurements at the Zeppelin Station, Svalbard. *Physics and Chemistry of the Earth* 28, pp. 1181–1190. DOI: 10.1016/j.pc.2003.08.058.

Suzuki, Y., T. Suzuki, and N. Furuta (2010). Determination of Rare Earth Elements (REEs) in Airborne Particulate Matter (APM) Collected in Tokyo, Japan, and a Positive Anomaly of Europium and Terbium. *Analytical Sciences* 26, pp. 929–935. DOI: 10.2116/analsci.26.929.

Swami, K., C.D. Judd, J. Orsini, K.X. Yang, and L. Husain (2001). Microwave assisted digestion of atmospheric aerosol samples followed by inductively coupled plasma mass spectrometry determination of trace elements. *Fresenius Journal of Analytical Chemistry* 369.1, pp. 63–70. DOI: 10.1007/s002160000575.

Teinilä, K., R. Hillamo, V.M. Kerminen, and H.J. Beine (2003). Aerosol chemistry during the NICE dark and light campaigns. *Atmospheric Environment* 37, pp. 563–575. DOI: 10.1016/S1352-2310(02)00826-9.

— (2004). Chemistry and modal parameters of major ionic aerosol components during the NICE campaigns at two altitudes. *Atmospheric Environment* 38, pp. 1481–1490. DOI: 10.1016/j.atmosenv.2003.11.028.

Toscano, G., A. Gambaro, I. Moret, G. Capodaglio, C. Turetta, and P. Cescon (2005). Trace metals in aerosol at Terra Nova Bay, AntArctica. *Journal of Environmental Monitoring* 7.12, pp. 1275–1280. DOI: 10.1039/B507337P.

Tostevin, R., G.A. Shields, G.M. Tarbuck, T. He, M.O. Clarkson, and R.A. Wood (2016). Effective use of cerium anomalies as a redox proxy in carbonate-dominated marine settings. *Chemical Geology* 438, pp. 146–162. DOI: 10.1016/j.chemgeo.2016.06.027.

Tunved, P., J. Ström, and R. Krejci (2013). Arctic aerosol life cycle: linking aerosol size distributions observed between 2000 and 2010 with air mass transport and precipitation at Zeppelin station, Ny-Ålesund, Svalbard. *Atmospheric Chemistry and Physics* 13, pp. 3643–3660. DOI: `10.5194/acp-13-3643-2013`.

Turetta, C., R. Zangrando, E. Barbaro, J. Gabrieli, E. Scalabrin, P. Zennaro, A. Gambaro, G. Toscano, and C. Barbante (2016). Water-soluble trace, rare earth elements and organic compounds in Arctic aerosol. *Rendiconti Lincei* 27.1, pp. 95–103. DOI: `10.1007/s12210-016-0518-6`.

Turnipseed, A.A., S.B. Barone, and A.R. Ravishankara (1996). Reaction of OH with dimethyl sulfide. 2. Products and mechanisms. *Journal of Physical Chemistry* 100, pp. 14703–14713. DOI: `10.1021/jp960867c`.

Udisti, R., U. Dayan, S. Becagli, M. Busetto, D. Frosini, M. Legrand, F. Lucarelli, S. Preunkert, M. Severi, R. Traversi, and V. Vitale (2012). Sea spray aerosol in central Antarctica. Present atmospheric behaviour and implications for paleoclimatic reconstructions. *Atmospheric Environment* 52, pp. 109–120. DOI: `10.1016/j.atmosenv.2011.10.018`.

Udisti, R., S. Becagli, D. Frosini, C. Ghedini, F. Rugi, M. Severi, R. Traversi, R. Zanini, G. Calzolai, M. Chiari, F. Lucarelli, S. Nava, F. Ardini, M. Grotti, D. Vione, M. Malandrino, E. Bolzacchini, L. Ferrero, M.G. Perrone, G. Sangiorgi, S. Francesconi, S. Giannarelli, D. Cappelletti, B. Moroni, D. Ceccato, P. Mittner, and P. Sartori (2013). *Activity and preliminary results from the 2011 and 2012 field seasons at Ny Alesund.*

Urbanica (2012). *The 250 Largest Industrial Centers of Russia (Top-250) - 2010.* URL: `http://urbanica.spb.ru/en/research/ratings/250-krupnejshih-promyshlennyh-tsentrov-rossii-top-250-2010/`.

Viola, A.P., V. Vitale, I. Petroni, F. Tampieri, M. Mazzola, C. Lanconelli, M. Busetto, A. Lupi, L. Di Liberto, A. Conidi, A. Ianniello, R. Salvatori, G. Esposito, F. Spataro, R. Udisti, S. Becagli, D. Frosini, C. Ghedini, R. Traversi, D. Cappelletti, M. Valt, and C. Turetta (2013). *Atmospheric studies at "Dirigibile Italia".*

Wagenbach, D., S. Preunkert, J. Schäfer, W. Jung, and L. Tomadin (1996). *Northward transport of Saharan dust recorded in a deep alpine ice core. In: The impact of desert dust across the mediterranean.* Ed. by S. Guerzoni and R. Chester. Vol. 11. Springer.

Wilde, P., M.S. Quinby-Hunt, and B.D. Erdtmann (1996). The whole-rock cerium anomaly: a potential indicator of eustatic sea-level changes in shales of the anoxic facies. *Sedimentary Geology* 101, pp. 43–53. DOI: 10.1016/0037-0738(95)00020-8.

Winton, M. (2006). Amplified Arctic climate change: What does surface albedo feedback have to do with it? *Geophysical Research Letters* 33.3, pp. 1–4. DOI: 10.1029/2005GL025244.

Wolff, E.W., H. Fischer, F. Fundel, U. Ruth, B. Twarloh, G.C. Littot, R. Mulvaney R.and Röthlisberger, M. de Angelis, C.F. Boutron, M. Hansson, U. Jonsell, M.A. Hutterli, F. Lambert, P. Kaufmann, B. Stauffer, T.F. Stocker, J.P. Steffensen, M. Bigler, M.L. Siggaard-Andersen, R. Udisti, S. Becagli, E. Castellano, M. Severi, D. Wagenbach, C. Barbante, P. Gabrielli, and V. Gaspari (2006). Southern Ocean sea-ice extent, productivity and iron flux over the past eight glacial cycles. *Nature* 440, pp. 491–496. DOI: 10.1038/nature04614.

Wu, G., B. Xu, C. Zhang, S. Gao, and T. Yao (2009). Geochemistry of dust aerosol over the Eastern Pamirs. *Geochimica et Cosmochimica Acta* 73.4, pp. 977–989. DOI: 10.1016/j.gca.2008.11.022.

Xie, Y. and C.M. Berkowitz (2007). The use of conditional probability functions and potential source contribution functions to identify source regions and advection pathways of hydrocarbon emissions in Houston, Texas. *Atmospheric Environment* 41.28, pp. 5831–5847. DOI: 10.1016/j.atmosenv.2007.03.049.

Zeng, Y. and P.K. Hopke (1989). A study of the sources of acid precipitation in Ontario, Canada. *Atmospheric Environment* 23.7, pp. 1499–1509. DOI: 10.1016/0004-6981(89)90409-5.

Zhang, Y., Z. Jiang, and B. Hu (2006). Determination of refractory elements in atmospheric particulates using slurry sampling electrothermal vaporization inductively coupled plasma optical emission spectrometry and inductively coupled plasma mass spectrometry with polyvinylidene fluoride as chemical modifier. *Rapid Communications In Mass Spectrometry* 20, pp. 2091–2098. DOI: 10.1002/rcm.2565.

Zhang, Y., Z. Jiang, M. He, and B. Hu (2007). Determination of trace rare earth elements in coal fly ash and atmospheric particulates by electrothermal vaporization inductively coupled plasma mass spectrometry with slurry sampling. *Environmental Pollution* 148, pp. 459–467. DOI:

10.1016/j.envpol.2006.12.004.